INAUGURAL - DISSERTATION

submitted to the
Combined Faculties for the Natural Sciences and for Mathematics
of the Ruperto - Carola University of Heidelberg, Germany
for the degree of
Doctor of Natural Sciences

presented by
Diplom-Chemiker Lars Meyer
born in Vechta

Oral examination: December 22, 2009

Expanding the STED Principle to Multicolor Imaging and Far-Field Optical Writing

Referees: Prof. Dr. Joachim Spatz
Prof. Dr. Stefan W. Hell

Abstract

Stimulated emission depletion (STED) nanoscopy has emerged as a powerful far-field technique for subdiffraction optical imaging and is extensively used in the life sciences to investigate different protein species. In many cases, however, the relative assembly of two (or more) proteins is of interest and needs to be determined with nanometric resolution. Meanwhile, STED has also found its way into material science. Yet, the method's potential for subdiffraction optical writing has so far remained unexplored. This work evidences the development of a dual-color STED setup with lateral resolving power of 30 nm in both color channels. The method is shown to be applicable to the study of double-stained neuronal proteins and aids in establishing a novel sample sectioning technique. As a result the first high-resolution three-dimensional reconstruction of dual-color STED images is rendered possible. Flexible operation of the individual color channels furthermore answers open questions in chemistry and biology. Another key point of this thesis is the realization of STED nanolithography. Subdiffraction-sized structures are written by bleaching a layer of fluorophores. The underlying concept of bleaching suppression through STED is experimentally introduced and theoretically described by a photophysical model. Numerical simulations corroborate the experimental findings. The presented studies take multicolor-STED nanoscopy close to macromolecular resolution and thus open up new methodical perspectives in the life sciences. STED nanolithography, on the other hand, has the potential of becoming an alternative to classical photolithography, thus simplifying high-resolution optical data storage.

Zusammenfassung

Die *stimulated emission depletion* (STED) Nanoskopie hat sich zu einer leistungsstarken, optisch nicht beugungsbegrenzten Fernfeld-Technik entwickelt und wird in den Lebenswissenschaften umfassend genutzt, um unterschiedliche Proteine zu untersuchen. Vielfach ist jedoch die relative Anordnung zweier (oder mehr) Proteine von Interesse und muss mit Auflösung im Nanometerbereich bestimmt werden. Mittlerweile hat STED auch in die Materialwissenschaften Einzug gehalten. Das Potential der Methode für optisches Schreiben unterhalb des Beugungslimits ist bislang jedoch unerschlossen geblieben. Die vorliegende Arbeit beschreibt die Entwicklung eines zweifarbigen STED Aufbaus mit lateraler Auflösung von 30 nm in beiden Farbkanälen. Die Methode wird zur Untersuchung doppelt gefärbter neuronaler Proteine genutzt und begünstigt die Einführung einer neuartigen Probenschneidetechnik. Daraus resultiert die erste dreidimensionale Rekonstruktion von zweifarbigen STED Bildern. Durch flexiblen Einsatz der einzelnen Farbkanäle werden darüberhinaus offene Fragestellungen in Chemie und Biologie beantwortet. Ein weiteres zentrales Thema dieser Arbeit ist die Realisierung von STED Nanolithographie. Strukturen unterhalb des Beugungslimits werden dabei durch Bleichen einer Farbstoffschicht erzeugt. Das zu Grunde liegende Konzept der STED Bleichunterdrückung wird experimentell vorgestellt und an Hand eines photophysikalischen Modells theoretisch beschrieben. Numerische Simulationen unterstützen die experimentellen Befunde. Die vorgestellten Studien bringen die mehrfarbige STED Nanoskopie nah an makromolekulare Auflösung heran und eröffnen damit neue methodische Perspektiven in den Lebenswissenschaften. Die STED Nanolithographie könnte eine interessante Alternative zu klassischer Photolithographie werden, was hochauflösende optische Datenspeicherung deutlich vereinfachen würde.

List of Publications

Parts of this work have been/will be published as the following journal contributions/patents:

- Lars Meyer, Jan Keller, Christian Eggeling, and Stefan W. Hell. Nanolithography using Stimulated Emission Depletion (STED) Nanoscopy. *In preparation*.

- Lars Meyer, Dominik Wildanger, Rebecca Medda, Annedore Punge, Silvio O. Rizzoli, Gerald Donnert, and Stefan W. Hell. Dual-Color STED Microscopy at 30-nm Focal-Plane Resolution. *Small*, 4: 1095-1100, 2008.

- Gyuzel Mitronova, Vladimir Belov, Mariano Bossi, Christian Wurm, Lars Meyer, Rebecca Medda, Gael Moneron, Stefan Jakobs, Christian Eggeling, and Stefan W. Hell. New Fluorinated Rhodamines as Photostable Fluorescent Dyes for Optical Microscopy and Nanoscopy. *accepted* (by *Chem. Eur. J.*).

- Hanna Regus-Leidig, Susanne tom Dieck, Dana Specht, Lars Meyer, and Johann Helmut Brandstätter. Early Steps in the Assembly of Photoreceptor Ribbon Synapses in the Mouse Retina: The Involvement of Precursor Spheres. *J. Comp. Neurol.*, 512: 814-824, 2009.

- Annedore Punge, Silvio O. Rizzoli, Andreas Schönle, Lars Kastrup, Lars Meyer, Jan D. Wildanger, Reinhard Jahn, and Stefan W. Hell. 3D Reconstruction of High-Resolution STED Microscope Images. *Microsc. Res. Tech.*, 71: 644-650, 2008.

- Stefan W. Hell, Vladimir Belov, Gyuzel Mitronova, Mariano Bossi, Gael Moneron, Christian Wurm, Stefan Jakobs, Christian Eggeling, Jakob Bierwagen, and Lars Meyer. New Fluorinated Rhodamines as Photostable Fluorescent Dyes for Labelling and Imaging Techniques. Patent, 2009. PCT/EP2009/004650.

Abbreviations

AM	Absorbance modulation
APD	Avalanche photodiode
BSF	Bleach suppression factor
cw	Continuous wave
D-Rex/T-Rex	Dark state/triplet relaxation
FCS	Fluorescence correlation spectroscopy
FPALM	Fluorescence photoactivation localization microscopy
FRET	Fluorescence/Förster resonance energy transfer
FWHM	Full width half maximum
GSD	Ground state depletion
IR	Infrared
NA	Numerical aperture
$\mathrm{Nd{:}YVO_4}$	Neodymium-doped yttrium orthovanadate
NF-L/-M/-H	Neurofilament light/medium/heavy
NHS	*N*-Hydroxysuccinimide
OPA	Optical parametric amplifier
PALM	Photoactivation localization microscopy
PBS	Phosphate buffered saline
PMMA	Polymethylmethacrylate
PMT	Photomultiplier tube
PSF	Point spread function
PVA	Polyvinyl alcohol
RAPID	Resolution augmentation through photo-induced deactivation
RegA	Regenerative amplifier
RESOLFT	Reversible saturable optical fluorescence transition
SLM	Spatial light modulator
SNARE	Soluble N-ethylmaleimide-sensitive-factor attachment receptor
SSIM	Saturated structured illumination microscopy
STED	Stimulated emission depletion
STORM	Stochastic optical reconstruction
TCSPC	Time-correlated single photon counting
Ti:sa	Titanium-sapphire

Contents

1 Introduction

The visualization of (macro)molecular structures and processes has always been an important challenge for researchers of various fields of expertise including chemistry, physics and biology. Nowadays there is a full variety of complementary microscopic techniques at hand to gain new insight into a system's nature. Likewise, the inverse approach of manipulating matter with nanometric resolution in lithography has become increasingly important throughout the years since adequate technologies enable compact and cost-effective data-storage devices.

Still, there is unwaning interest in further enhancing resolution in optical imaging and writing. Molecular biologists, for instance, seek to clarify open questions with superresolving microscopes while material scientists strive for highly resolving but less complex optical nanopatterning techniques.

1.1 Light microscopy and lithography in the course of time

The phenomenon that objects appear magnified in water is known since ancient times. 2800 year old Egyptian hieroglyphs depicting simple glass meniscal lenses are supposed to be the earliest historical reference to magnification. [1] 900 years later the roman savant Seneca provided the first reliable record of magnification: "Letters, however small and indistinct, are seen enlarged and more clearly through a globe of glass filled with water". [1] Without any knowledge of the underlying physics, however, these first observations of magnification were falsely ascribed to intrinsic properties of water. It therefore took another 900 years until the Arabian scholar Ibn al-Haytham (Alhazen) built the first historically evidenced magnifying device - a convex lens. [1] Having written the seven-volume treatise *Book of Optics* from 1011 to 1021 he has had substantial influence on the development of optics as a science. [2] Some time after this book became available in Europe the development of spectacles began in 13th-century Italy. [3] To date it is not fully clarified who invented the first actual microscope but general consensus is that the Dutch spectacle-makers Zacharias Janssen and Hans Janssen may be credited with this invention. [3] Around 1590 they constructed a two-lens system with a sliding tube essentially having built a compound microscope. [4] The same instrument was independently developed by the Tuscan physicist Galileo Galilei in 1624. He inverted an initially built telescope by using two convex lenses instead of concave and convex lenses and termed the device *Occhialino* - the “little eye”. [5] Significant improvement was later on achieved by Robert Hooke (1635-1703) who introduced a third lens in a compound microscope thereby increasing the magnification of earlier two-lens designs. His microscopic observations including those that led to the term *cell* are written up in his 1665 treatise *Micrographia*. [5]

Probably one of the most famous workshops for microscopes was run by Carl Friedrich Zeiss in Jena, Germany from 1848 on. In order to bring together manufacturing skills and scientific insight he later on hired a colleague from the University of Jena whose name was Ernst Carl Abbe. This collaboration proved to be very fruitful as Abbe not only derived quality criteria for lenses but also found a fundamental limit for the resolution of an optical microscope. The equations read

$$\Delta r \approx \frac{\lambda}{2n \sin(\alpha)} \tag{1.1a}$$

$$\Delta z \approx \frac{\lambda}{2n \sin^2(\alpha/2)} \tag{1.1b}$$

where $\Delta \mathrm{r}$ and $\Delta \mathrm{z}$ denote the full width half maximum (FWHM) of a focused light spot along the lateral and axial direction, respectively. The wavelength is symbolized by λ, n is the refractive index and α the semi-aperture angle. [6] This limitation has detained further resolution enhancement for more than a century. It was not until 1994 that this barrier could be broken by stimulated emission depletion (STED) microscopy - a technique whose further development is a central aspect of this thesis. [7]

The history of printing starts in the Chinese Han Dynasty (25-220). [8] Paper - the recording material for printing - was invented in the year 105 by Cai Lun [1] who used different media, for example sheets from macerated tree bark or fishing-nets. [9] Since ink was already known by that time (in use since about 2500 B. C. [10]) the combination of recording medium (paper), writing material (ink) and templates (reliefs on seals and marble pillars) allowed for the production of printed matter. However, this procedure - especially the tem-

---

[1] It is controversial whether Cai Lun truly invented the production of paper or essentially built up on knowledge of ancestors.

plate fabrication - was cumbersome and therefore replaced by using engraved wood blocks as templates. A few hundreds of years later ($\sim$ 1040) Bi Sheng invented a movable type the fabrication know-how of which being transferred to Europe soon thereafter. Inspired by this idea Johannes Gutenberg optimized the procedure by using lead molds as movable types. [11] Together with his invention of a mechanical press around 1450 he provided a complete and economic package for typography.

The yet still rather high costs of printing urged Alois Senefelder (1771 - 1834) to look for alternative ways to publish his works. [12] He experimentally found out that ink poured over moistened limestone which was treated with a greasy pencil in some areas deposited only in the drawn regions. [2] Based on these experiments the technique became known as *lithography* from the Greek words *lithos* (stone) and *graphein* (to write). Lithography has laid the foundation for modern offset printing and keeps getting further developed up to present days. A remarkable paradigm shift was the introduction of light as a writing material in photolithography which nowadays allows for patterning of micro- and nanoscale objects. [8]

1.2 Stimulated emission depletion (STED) nanoscopy and its photophysical principles

Abbe's diffraction limit of light (equation (1.1)) is a fundamental principle of optics and clearly specifies the ways to improve resolution in microscopy: Both shortened wavelengths and increased numerical apertures result in narrower sizes of the diffraction spot. Yet, this procedure has come to a developmental status from where minor improvements can only be realized at high expenses (both technically and economically). The question therefore arises how to fundamentally break the diffraction limit to boost resolution in microscopy at reasonable expenses. Stimulated emission depletion (STED) microscopy [7] was the first far-field concept to succeed in achieving subdiffraction resolution and is the keystone for all new developments presented in this thesis. Therefore its principles will thoroughly be introduced in the following. As full comprehension of the STED concept necessitates some knowledge about the underlying photophysics a section devoted to this topic is prefixed.

---

[2] The reason for this finding is, of course, the hydrophoby of ink which preferentially mixes with lipophilic grease.

1.2.1 Molecular photophysics of electronic transitions

With the advent of fluorescence microscopy at the beginning of the 20th century a technique was born that should from then on be continuously developed for efficiency and specificity. It allows for fast three-dimensional imaging of living cells and plays a well-established role in the life sciences. Also this thesis deals with the development of a special form of super-resolving fluorescence microscopy for which reason it is worth taking a closer look at the underlying photophysics.

For a transition between states m (lower energy) and n (higher energy) to occur two conditions have to be fulfilled. First, the frequency ν needs to be tuned such that the product of it and the Planck constant h matches the energy difference between the two states: $E_n - E_m \approx h\nu$. In addition, the transition moment $\vec{R}_{nm} = \int \psi_n^* (x) \hat{\vec{\mu}} \psi_m (x) \, \mathrm{d}x$ needs to be different from zero. In this equation ψ_s is the wave function of unperturbed state s along the spatial coordinate x and $\hat{\vec{\mu}}$ is the operator of the electric dipole moment. [13] Einstein identified three contributions to the transition between states:

(i) Stimulated absorption This process describes the transition from state m to state n and is driven by the electromagnetic field oscillating at the transition frequency. The total number of absorption events in time interval t is $N_m B_{mn} \rho (\nu) t$ where N_m is the number of molecules in state m and B_{mn} is the *Einstein coefficient of (stimulated) absorption*. If B_{mn} is large strong transitions will occur which means that the sample will be strongly absorbing.

(ii) Stimulated emission The radiation of frequency ν that induces absorption is also capable of inducing emission events thus producing photons with the same frequency ν. We therefore may write $N_n B_{nm} \rho (\nu) t$ - a relation analogous to stimulated absorption with the permuted indices being the only difference. Einstein found out that the coefficients of stimulated absorption and emission are equal and thus $B_{mn} = B_{nm} = B$. Furthermore, a detailed analysis gives

$$B = \frac{|\mu|^2}{6\epsilon_0 \hbar^2} \tag{1.2}$$

with μ the transition moment, ϵ_0 the vacuum permittivity and $\hbar = h/2\pi$. [14] Again, we see that absorption may only take place if the transition moment takes on a nonzero value.

(iii) Spontaneous emission In addition to stimulated emission there is another radiative relaxation pathway for the molecule which is independent of any field influence. The *Einstein coefficient of spontaneous emission* is denoted as A_{mn} and is related to B via

$$A = \left(\frac{8\pi h \nu^3}{c^3} \right) B \tag{1.3}$$

when the spectral energy density is taken into account. Here, h is the Planck constant and c the velocity of light, respectively. While spontaneous emission may largely be ignored at relatively low frequencies of rotational and vibrational transitions it follows from equation (1.3) that it is strongly enhanced at higher frequencies used for electronic transitions. As will be explained in detail later on the phenomenon of fluorescence is one form of spontaneous emission.

So far general aspects of any kind of molecular transition have been worked out. We shall now take a closer look at electronic transitions which occur at excitation energies between 1 eV (electron volts) and 10 eV - values that correspond to wavelengths between $\sim$ 1250 nm and $\sim$ 125 nm and therefore cover the whole visible range of the electromagnetic spectrum. In order to understand the selection rules for electronic transitions we consider a two-atomic linear molecule whose total angular momentum takes on values $\Lambda\hbar$ where $\Lambda = 0, \pm 1, \pm 2$ etc.. To characterize these states they are symbolized as terms

$$\begin{aligned} \Lambda =& 0, 1, 2, 3, \cdots \\ & \Sigma, \Pi, \Delta, \Phi, \cdots \end{aligned}$$

The total spin component S is split to multiplets with multiplicity $2S + 1$. The multiplicity is denoted as a number on the upper left of the term symbol. Hence, a triplet state with $\Lambda = 1$ would be symbolized as ${}^3\Pi$, e. g.. A subscript g or u specifies the parity of two atoms which is their behaviour under inversion (Σ_g or Π_u, for example). Finally, superscripted index $+$ or $-$ gives notice of symmetric or antisymmetric behaviour of the electronic wave function to a mirror plane through neighboured atoms.

The selection rules concerned with changes in angular momentum are

$$\Delta\Lambda = 0, \pm 1 \quad \Delta S = 0 \quad \Delta\Sigma = 0 \quad \Delta\Omega = 0, \pm 1$$

where $\Omega = \Lambda + \Sigma$ is the quantum number for the total angular momentum along the internuclear axis.

Allowed and forbidden changes in symmetry are summarized by two other selection rules. The *Laporte rule* for centrosymmetric molecules states that the only allowed transitions are transitions that are accompanied by a change of parity, i. e., $u \rightarrow g$ and $g \rightarrow u$. Secondly, only Σ^+ and Σ^+ (and Σ^- and Σ^-) terms can combine. Transitions between states of equal parity become (weakly) allowed when the center of symmetry is lost due to asymmetrical vibration. Such transitions are called vibronically allowed. An important consequence of these rules is that - in first approximation - singlet terms only combine with singlet terms and analogously transitions from triplet states only occur to other triplet states. In a conventional organic fluorophore electrons are usually paired in the ground state which means that for such a molecule the ground state is a singlet state. Consequently, irradiation with a resonant frequency ν will excite the molecule to another, higher excited singlet state.

Considering a defined electronic state of a diatomic molecule its vibrational energy depends also on the atomic core separation. The course of the potential energy as a function of core separation is well described by the *Morse-potential*

$$V(r) = D_e \left[1 - e^{-\beta\left(r - r_{\mathrm{gl}}\right)}\right]^2 \tag{1.4}$$

which accounts for dissociation through D_e as the dissociation energy (without consideration of the zero point energy). r_{gl} is the equilibrium distance and β is a constant. Another particular feature of the Morse potential is anharmonicity at larger core separations. In larger N-atomic molecules the potential energy surface cannot be plotted that easily as the molecule has $3N - 6$ degrees of freedom. Yet, a qualitative discussion of the vibronical transitions in such a molecule is possible by selecting a single normal mode of vibration and plotting its potential energy along the core coordinate for the first two electronic states as has been done in figure 1.1 (A). [3] The transition in this scheme occurs from the vibrational ground state $v'' = 0$ of the electronic ground state into a higher excited vibrational level $v' = 2$ of the first excited electronic state. This is a consequence of the *Franck-Condon principle* which states that nuclei are so much more massive than the electrons that an electronic transition takes place much faster than the nuclei can respond. [14] The transitions therefore occur at fixed core positions which corresponds to a *vertical* excitation in the pictorial of figure 1.1 (A). In figure 1.1 (B) this corresponds to the excitation pathway from S_0 to $\mathrm{S}_{1,\mathrm{vib}}$. From a quantum mechanical point of view the vibronic transition excites the molecule into a vibrational state that most closely resembles the vibrational wave function of the vibrational ground state of the lower electronic state having the equilibrium distance r_{gl}. If the upper curve is shifted horizontally the transition will terminate in the higher excited vibrational state $v' = 2$. Other vibrational states will, however, also be populated (with lower probability) because they lie relatively close to each other. Vibrational substructure will be present in the electronic spectra. After fast ($\sim$ 200 fs) energy loss through nonradiative internal conversion the molecule energetically descends to the vibrational ground state of S_1. Here, the molecule has a rela-

---

[3] Figure 1.1 (A) has been taken from:
`http://commons.wikimedia.org/wiki/File:Franck-Condon-Prinzip.svg`.

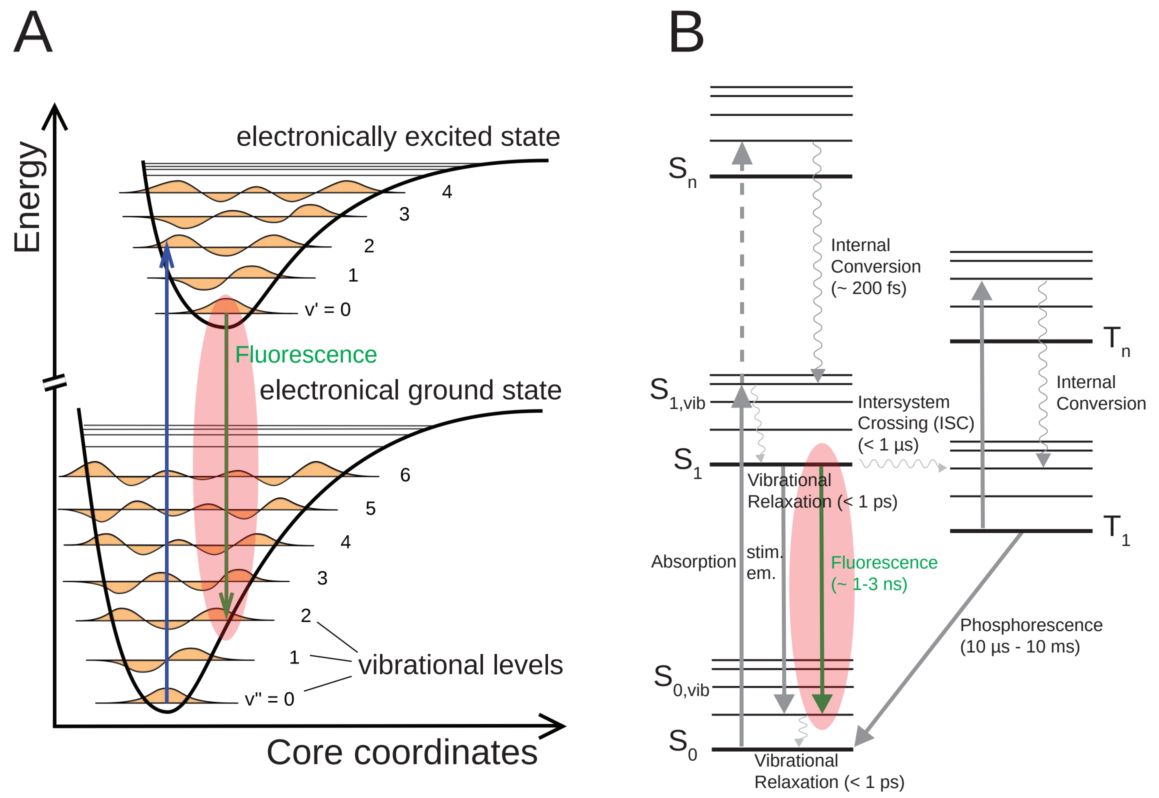

Figure 1.1: (A) Illustration of the Franck-Condon principle. (B) Jablonski diagram of the possible transitions in an electronic five-level system. Special attention is paid to the molecular de-excitation that generates fluorescence.

tively long life time (typically 1-3 ns) because surrounding molecules cannot take the large energy needed to let our molecule relax to the electronic ground state. [4] Relaxation finally occurs spontaneously as *fluorescence* into a higher vibrational state of the electronic ground state producing radiation with a frequency matching the according energy difference. From figure 1.1 (A) it also becomes clear that fluorescence is generally red-shifted to its excitation radiation with the frequential difference of which being called the *Stokes shift*. The actual wavelength of the fluorescence may vary between different solvents because the molecular surrounding strongly influences accommodation of the excited state.

Another particularity of a molecule's electronic structure is that strong spin-orbit coupling may cause the spin of one of the two binding electrons to flip in the excited electronic state. As a result the total spin S is increased to 3 and the molecule afterwards resides in a (vibrationally excited) triplet state T_1 which has a slightly lower energy than S_1 as depicted

---

[4] Alternatively, the molecule could also be de-excited by stimulated emission as indicated in figure 1.1 (B).

in figure 1.1 (B). In the illustration of figure 1.1 (A) another potential energy curve would be present lying close to and energetically slightly lower than the first excited singlet state. In fact, the curves would cross at an intersection point where so-called *Intersystem crossing* from S_1 to T_1 may take place. If the electron is not further excited to T_n it is trapped in T_1 for a relatively long period of time (10 μs - 10 ms) because relaxation to ground state S_0 is spin-forbidden. However, spin-orbit coupling finally allows the electron to be de-excited producing another form of spontaneous emission called *phosphorescence*. Both the presence and the absence of significant intersystem crossing can be exploited in different techniques of fluorescence microscopy. As will thoroughly be discussed in chapter 4 this work takes advantage of dyes exhibiting only minor triplet buildup.

1.2.2 Fluorescence microscopy

While the phenomenon of fluorescence was first described by G. G. Stokes in 1852 it took another 100 years to open up the door for widespread use of fluorescence as a contrast mechanism in microscopy. [15] The breakthrough came with the invention of immunohistochemistry - a technique to specifically bind antibody-tagged fluorescent molecules to antigens. [16] In this manner it was finally possible to label only the biological molecules of interest thus greatly improving the selectivity and specificity of fluorescence microscopy. Enhancement of the fluorescent signal can be accomplished by using secondary antibodies tagged with multiple fluorophores in addition to primary antibodies.

Despite its great success in biological imaging up to present days a drawback that accompanies immmunolabeling is its lack of live cell compatibility. A valuable remedy for this has been introduced in 1994 when fluorescent proteins could be shown to be expressible in other organisms. [17,18]

Apart from staining molecules with organic fluorophores or fluorescent proteins another promising approach is the use of quantum dots (QDs) as biological labels. Originally used in material sciences these luminescent semiconductor nanoparticles made of, e. g., CdS, ZnS or PbS are characterized by low photobleaching rates and size-dependent emission spectra. [19,20]

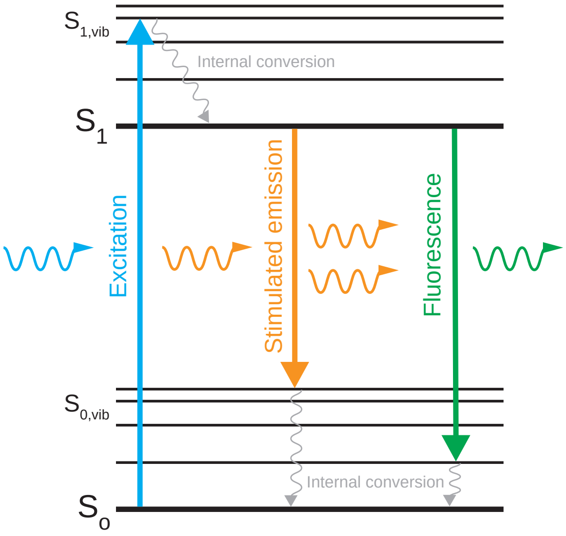

Figure 1.2: A vibronical excitation is rapidly followed by radiationless internal conversion to the vibrational ground state of S_1. Now an incoming photon with an energy gap matching frequency can induce emission of another (coherent) photon through stimulated emission. Alternatively, spontaneous emission takes place within a few nanoseconds resulting in the emission of a fluorescence photon.

1.2.3 Principles of STED nanoscopy

The following lines seek to clarify how stimulated emission depletion (STED) is capable of breaking the diffraction limit of light thus providing some fundamental knowledge about the process which is vital for the further understanding of this thesis.

It is known from section 1.2.1 that a vibronically excited fluorophore has two basic relaxation pathways: It can either return to the ground state through spontaneous emission of fluorescence (typically within 1-3 ns for a conventional fluorophore) or be subject to stimulated emission induced by another photon with a wavelength that matches the energy gap between S_1 and S_0 (Figure 1.2). If we neglect the rates of vibrational relaxations the population of state S_1 at time t is given by

$$\frac{\mathrm{d}\,[\mathrm{S}_1]}{\mathrm{d}t} = k_{\mathrm{exc}}\,[\mathrm{S}_0] - (k_{fl} + k_{\mathrm{STED}})\,[\mathrm{S}_1] \tag{1.5}$$

where $\mathrm{k}_{\mathrm{exc}}$, k_{fl} and $\mathrm{k}_{\mathrm{STED}}$ are the rate constants of excitation, fluorescence emission and stimulated emission, respectively. The idea of STED is now to optically drive stimulated emission from S_1 to S_0 with a so-called STED beam in order to deplete the population of S_1 as much as possible. [7] To see how that is possible we have to consider first that each rate constant k_{n} is a product of cross section σ_{n}, reciprocal photon energy γ_{n} and intensity

I_n [21]:

$$k_\mathrm{exc} = \sigma_\mathrm{exc} \cdot \gamma_\mathrm{exc} \cdot I_\mathrm{exc} \tag{1.6a}$$

$$k_\mathrm{STED} = \sigma_\mathrm{STED} \cdot \gamma_\mathrm{STED} \cdot I_\mathrm{STED} \tag{1.6b}$$

$$k_\mathrm{fl} = 1/\tau_\mathrm{fl} \tag{1.6c}$$

The rate constant of fluorescence is given by the inverse fluorescence lifetime τ_fl. Obviously, the fluorescence lifetime is an intrinsic molecular property whereas the other rate constants - especially that of stimulated emission - can be tuned by changing the applied light intensity of the respective beam.

Two principal cases can be differentiated: Either excitation and STED beam act simultaneously as in CW mode or they act successively which corresponds to pulsed mode. [7, 22] Assuming a normalized population $[\mathrm{S}_0] + [\mathrm{S}_1] = 1$, a comparatively low excitation rate k_exc and stationary state conditions $\frac{\mathrm{d}[\mathrm{S}_1]}{\mathrm{d}t} = 0$ the population of S_1 in the CW case can be calculated as

$$[\mathrm{S}_1]\left(I_\mathrm{STED}\right) = \frac{k_\mathrm{exc}}{k_\mathrm{exc} + k_\mathrm{fl} + k_\mathrm{STED}} \tag{1.7}$$

In pulsed mode excitation and de-excitation through stimulated emission depletion are temporally separable with the STED pulse lagging behind the excitation pulse by typically some tens of picoseconds for optimum depletion. [23] Given the initial conditions $[\mathrm{S}_1]\left(t_0\right) = 1$ and $[\mathrm{S}_1]\left(t \rightarrow \infty\right) = 0$ equation (1.5) can be solved to yield

$$[\mathrm{S}_1]\left(t\right) = e^{-(k_\mathrm{fl} + k_\mathrm{STED})t} \tag{1.8}$$

With a rectangular pulse width τ_p the population of state S_1 after each pulse is given by

$$[\mathrm{S}_1]\left(I_\mathrm{STED}\right) = e^{-k_\mathrm{STED}\tau_\mathrm{P} + k_\mathrm{fl}\tau_\mathrm{P}} \tag{1.9}$$

thus yielding the STED power dependence of the S_1 population.

A direct comparison of equations (1.7) and (1.9) evidences that strong depletion can be expected if the STED rate clearly outperforms the fluorescence rate, i. e., if $k_\mathrm{STED} >> k_\mathrm{fl}$. [5] Considering equation (1.6) we see that this is accomplished by applying high STED intensities. From a physical point of view this corresponds to a situation where the process of stimulated emission is saturated thus effectively quenching fluorescence de-excitation. This

---

[5] A constant excitation rate k_exc is assumed.

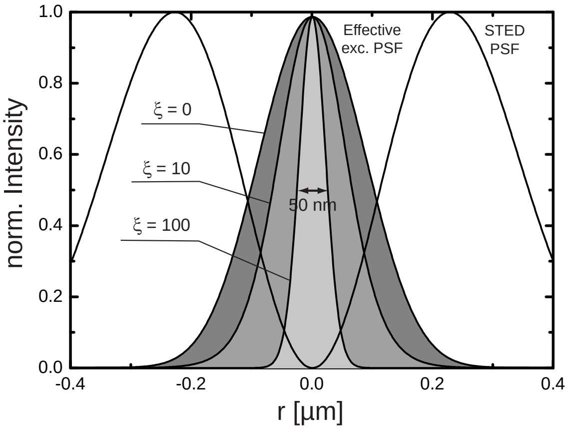

Figure 1.3: Pulsed-mode simulation of the effective excitation PSFs for different values of the saturation factor ξ. The higher the value of ξ and hence the applied STED power the narrower the effective PSF's FWHM. $\xi = 0$ corresponds to the confocal PSF. Note the STED beam's line profile: It features a central zero allowing for undepleted fluorescence only in this spot.

causality is also the key for overcoming the diffraction limit in STED microscopy. To this end the STED beam needs to be spatially shaped such that it incorporates a zone of zero intensity, e. g., by inserting a vortex phase plate into the beam which imprints a helical 0-2 π phase ramp on the beam's wavefront. [24] When the beam is focused in such a way, destructive interference leads to a central zero intensity region which becomes narrower with increasing STED intensity. Superimposing the STED beam with a diffraction-limited excitation beam then yields an effective point spread function (PSF) [6] which exhibits a full width half maximum (FWHM) that can eminently be smaller than the diffraction limit (compare figure 2.7). Figure 1.3 displays the shape of the effective PSF for different values of the saturation factor $\xi = \mathrm{I_{STED}}/\mathrm{I_{sat}}$ where $\mathrm{I_{sat}}$ is the STED intensity at which half of the initial fluorescence is switched off. Increasing values of ξ and thus increasing STED intensities lead to narrower full width half maxima of the effective PSF. While the effective PSF for the case $\xi = 0$ simply corresponds to the diffraction-limited confocal PSF of $\sim$ 230 nm FWHM strong stimulated emission depletion at $\xi = 100$ narrows the FWHM to $\sim$ 50 nm. [7] In principal unlimitedly small FWHM could be reached as $\mathrm{I_{STED}} \rightarrow \infty$. The resulting lateral spot size Δr at a given STED power can be estimated using the formula

$$\Delta r \approx \frac{\lambda}{2n \sin \alpha \sqrt{1+\xi}} \tag{1.10}$$

---

[6] A point spread function is the irradiance produced by the optical system with an input point source.

[7] The calculation was performed for excitation and STED wavelengths of λ = 635 nm and λ = 750 nm, respectively.

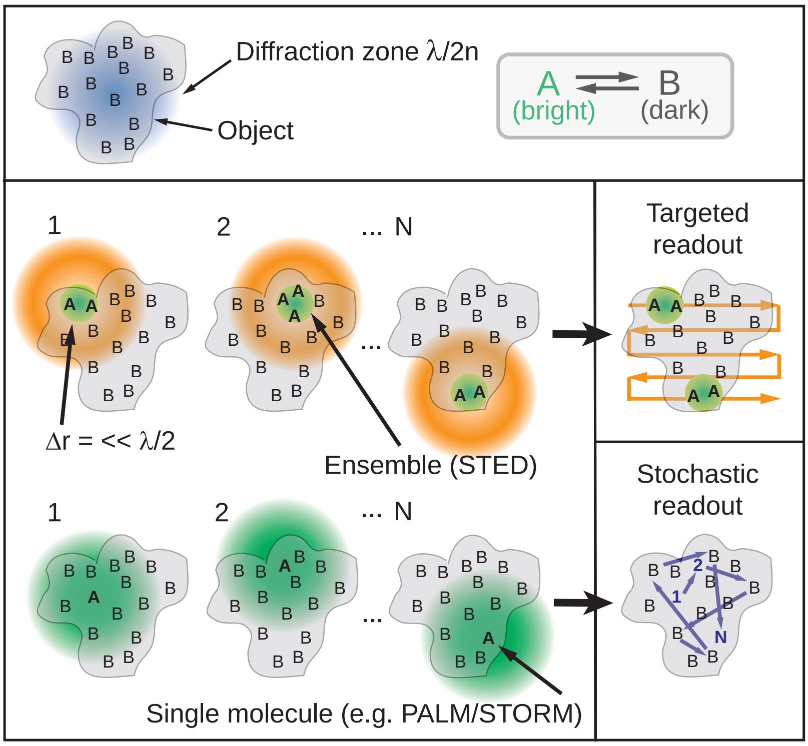

Figure 1.4: An illustration of the different readout schemes for superresolution microscopy techniques. In STED microscopy the image is recorded by targeted readout of an ensemble of fluorescent molecules within a subdiffraction-sized focal volume Δr. Single-molecules techniques (e. g., PALM/STORM) use stochastical switching of individual molecules and subsequent localization for assembling an image.

which resembles the usual Abbe formula (eq. (1.1)) but features an additional square root term that describes the nonlinear reduction of the FWHM with increasing STED intensity. [25] It is evident that the spot size in STED microscopy is no longer limited by diffraction.

In order to acquire an entire superresolved image of a sample the fluorescent markers of the object need to be localized somehow. In the case of STED this is achieved by spatially translating the shaped STED beam across the specimen as shown in figure 1.4. An ensemble of initially dark molecules will then be excited within a subdiffraction-sized excitation volume Δr at each position r_{i} of the STED beam rendering the readout targeted. [26] It is important to understand that this readout scheme is fundamentally different to that of single-molecule based superresolution techniques such as PALM/STORM. There, the sample is weakly illuminated with a usual diffraction-limited beam to excite only one individual molecule within the focal volume. If this is done many times the molecules are stochastically switched on and off and their positions can computationally be localized. Nevertheless both techniques - and essentially all contemporary superresolution methods - share the common ground of recording sub-λ features sequentially in time. [26]

To sum up STED microscopy utilizes two superimposed laser beams: A conventional beam for fluorescence excitation and a STED beam exhibiting a central zero intensity zone. By increasing the intensity of the latter fluorescence is effectively quenched by stimulated emission anywhere except for the beam center. This yields a subdiffraction-sized effective excitation PSF which can be scanned across the specimen for a targeted fluorescence readout. As a result an image is assembled the resolution of which not being limited by diffraction anymore.

1.3 Modern microscopy and lithography

In this section the most important contemporary microscopy and lithography techniques will be introduced and their distinct advantages and shortcomings will briefly be explained.

One of the most prominent types of high-resolution microscopy is **electron microscopy (EM)**. In high-resolution transmission electron microscopy (HRTEM) collimated kilovolt electron beams illuminate thin samples (thickness on the order of tens of nanometers). The electron wave field at the other side of the sample is then imaged by a series of electron lenses onto a detector at high magnification providing images with atomic resolution due to the electrons' short de Broglie wavelength. [27] Clearly, this method has made significant contributions to the understanding of fundamental questions in material science and biology. [28, 29] Up to present days the method has continuously been developed so that nowadays three-dimensional tomography of structures as large and complex as whole prokaryotic cells is possible with molecular resolution. [30] Despite this success EM has the intrinsic disadvantage of low sample penetration depth. As mentioned above the preparation of thin samples permits transmission of radiation in HRTEM but this requires sample sectioning. Furthermore, electron-beams are harmful to biological material thus impeding live cell imaging and the technical complexity of electron microscopes is high.

Other types of microscopy that excel at achieving very high resolution but have the drawback of being surface-bound techniques include **near-field scanning optical microscopy (NSOM)** and **atomic force microscopy (AFM)**. [31, 32]

Electron beams can not only be used for imaging but also for the structuring of resist film covered surfaces in **electron beam lithography (EBL)**. The film is sensitive to electrons and energy is deposited in the desired pattern. Scanning the beam across the surface thus produces defined structures. [33] EBL is used for research into the scaling limits of integrated circuits, for instance. [34] Working with a variety of materials it is a very flexible technique and offers nearly atomic resolution. However, throughput is a major concern which makes it much slower than optical lithography. [8] Additionally, secondary electrons are produced derogating pattern quality. Similar to EM systems EBL machines are moreover very expensive and complicated.

A common benefit of all kinds of light microscopy is that a sample can be illuminated with propagating light from the far-field which greatly simplifies experimental effort. The wavelength of the irradiating light often lies in the visible range of the electromagnetic spectrum. Visible light at moderate intensities does not damage biological material and has a much larger penetration depth than, for instance, electron beams. Conventional lenses and optics can be used to tightly focus the light onto the sample and the detected signal only stems from this focal region. Yet, as described in section 1.1 diffraction limits the focal spot size - and therefore similarly also the resolution - to approximately half the wavelength used. **Confocal microscopy** is a technique that was invented in 1955 and has extensively been used in the life sciences from then on. [35] The main vantage of confocal fluorescence microscopy in comparison to conventional (wide-field) fluorescence microscopy is the avoidance of detecting light from out-of-focus planes thus enabling optical sectioning of thick specimen. The straightforward principle of confocal microscopy is schematically displayed in figure 1.5. [8] After passing through a pinhole aperture that is situated in a conjugate plane (confocal) with a scanning point on the specimen and a second pinhole aperture positioned in front of the detector the illuminating light is focused onto the sample. From following the sketched beam path we can infer that only light of the focal plane is detected whereas any other light is blocked by the pinhole. Even if the size of the pinhole is significantly smaller than an Airy disc [9] the resolution of the confocal microscope is only slightly improved compared to a conventional one. This is because the technique is still diffraction-limited. In this thesis confocal images are often taken as a standard reference to be compared to the newly developed methods herein.

Among the different types of optical far-field microscopy those that exploit nonlinear

---

[8] The figure is based on an illustration found on the webpage `http://fb6www.uni-paderborn.de/ag/ag-sol/fgruppe/mainframe/microscope_e.htm`. Other depictions of the confocal principle can be found in any textbook on confocal microscopy.

[9] An *Airy disc* is defined as the distance between the primary intensity minima of an intensity distribution ς produced by focusing a light beam (ς is referred to as a *point-spread function* (PSF), see also section 2.2.3 for further explanation). The size of an Airy disc is $\Delta r = 1.22\lambda/\mathrm{NA}$ in lateral direction and $\Delta z = 4n\lambda/\mathrm{NA}^2$ along the optical axis where $\mathrm{NA} = n\sin(\alpha)$ is the numerical aperture of the system.

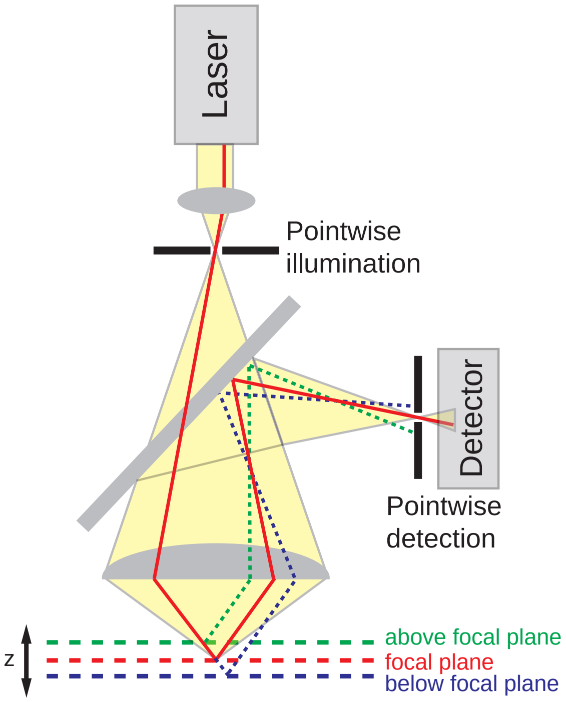

Figure 1.5: In confocal microscopy only light of the focal plane (red) is detected. Light from out-of-focus regions is blocked by a pinhole thus providing optical sectioning.

optical effects under strong irradiation have attracted much interest. [36–38] The main advantage of **multiphoton microscopy** is that a detection signal is generated only in the very focus where the light intensity is orders of magnitude larger than in surrounding areas. The (small) resolution enhancement of $\sqrt{2} \approx 1.4$ for two-photon microscopy is canceled out by the fact that doubled wavelengths need to be used to match the resonance of a fluorophore. Nevertheless, the longer wavelengths (mostly in the infrared range) used in multiphoton microscopy prove to be useful for imaging thick specimen because of their favourable tissue penetration properties and the low photodamage associated with red wavelengths.

Using extreme ultraviolet (EUV) light it is possible to structure surfaces with very high resolution in **EUV lithography**. A common approach is to employ 13 nm laser-plasma sources for lithography. [8] Owing to the extremely short wavelengths of EUV light this method indeed achieves impressive resolution but is economically disadvantageous because of expensive light sources. Another problem is the fact that air absorbs around 13 nm which means that the whole apparatus needs to be kept evacuated during operation. Although not subjected to the diffraction limit of light **x-ray lithography** suffers from the generation of secondary electrons. Another obstacle is dimension control of used masks since conventional lenses cannot focus x-rays. [8]

Optical lithography (photolithography) provides good experimental manageability at reasonable financial expenses because it operates at better accessible wavelengths than EUV lithography. However, diffraction of light limits the achievable resolution to approximately 100 nm in this case. [8]

Very generally, the above list of contemporary methods in microscopy and lithography suggests that near-field and non-optical methods, on the one hand, provide top resolution below the diffraction limit but are rather complex and/or expensive in use. On the other hand, most optical technologies are easy to use (far-field observation/manipulation, conventional lenses) but can't reach subdiffraction resolution because of light's wave nature. Hence, combining the beneficial properties of both forms - subdiffraction resolution with conventional optics - would render superior imaging/writing methods. Fortunately, such tools are latterly available and shall be introduced as superresolution microscopy. [26, 39]

The idea of **reversible saturable optical fluorescence transition (RESOLFT) microscopy** is to reversibly photoswitch an ensemble of fluorophores between a bright on state and a dark off state. [40] If an exciting and a depleting laser are spatially superimposed and the depletion of a state can be saturated anywhere except for the central part of the respective beam, the size of the effective PSF is reduced to

$$\Delta_{\text{eff}} \approx \frac{\Delta}{\sqrt{1 + I/I_{\text{sat}}}} \tag{1.11}$$

where Δ is the size of the diffraction-limited PSF, I the intensity of the depleting laser and I_{sat} the intensity at which 50% of the initial signal is depleted. [25] Equation (1.11) implies that in principle unlimitedly small sizes of the PSF are achievable as $I \rightarrow \infty$. The first concept of the RESOLFT family was **stimulated emission depletion (STED) microscopy** (see section 1.2.3 for a thorough desciption) which uses the ground state of a fluorophore as the dark state. [7] Since then other RESOLFT concepts such as **ground-state depletion (GSD) microscopy** and **RESOLFT with photoswitchable proteins** have been implemented. [41, 42] The former method employs the triplet state as the dark state, the latter utilizes conformational switching between a fluorescent and a non-fluorescent state in a protein.

Different concepts to break the diffraction limit in fluorescence microscopy are based on photoswitching of individual fluorophores with subsequent localization and are dubbed **photoactivation localization (PALM)**, **stochastic optical reconstruction (STORM)** and **flu-**

orescence photoactivation localization (FPALM) microscopy. [43–45] In these schemes resolution is defined by the localization accuracy of the fluorophores. Better localization hence improves resolution but simultaneously is accompanied by longer data acquisition times. Depending on the desired application a tradeoff between these two issues is necessary.

STED and PALM/STORM are capable of achieving three-dimensional superresolution and have been extended to subdiffraction multicolor imaging. [46–51] Live-cell imaging is as well possible as - in the case of STED - video-rate imaging. [51–54] Sharing the great advantage of not being fundamentally limited in resolution both techniques may be regarded as complementary each having certain particularities. STED, for instance, allows for fast image acquisition and live-cell imaging while PALM/STORM setups are rather easy and cost-effective in construction and maintainance.

The interference techniques **4Pi microscopy** and **I^{5}M microscopy** are characterized by resolution gain along the optical axis. [55, 56] This is accomplished by coherent illumination and detection with two opposing lenses thus enlargening the effective numerical aperture of the system. [10] The axial resolution gain of 4Pi microscopy has successfully been combined with lateral superresolution of STED to yield an almost spherical PSF. [57]

Finally, **structured illumination microscopy (SIM)** is capable of doubling conventional wide-field resolution by illuminating the sample with a series of excitation light patterns. [58, 59] The recorded images then contain encoded high-resolution information which can afterwards be extracted to construct the image. Yet, resolution enhancement beyond doubling cannot be obtained and the diffraction limit is not fundamentally overcome by this means. However, if fluorescence emission is saturated using high excitation intensities much finer excitation patterns are generated and resolution below 50 nm is possible in **saturated structured illumination microscopy (SSIM)**. [60] Note that SSIM closely resembles the RESOLFT concept as it relies on saturating the emission of a reversibly photoswitching fluorophore.

In photolithography a comparable developmental progress towards all-optical superresolution has been missing up to present days. Although it was recognized already some years ago that STED (and also other RESOLFT concepts) could provide a base for the development of a subdiffraction writing technique it was not until 2009 that this suggestion has been acted on. [61] Three STED inspired approaches have been published simultaneously which differ in the processes that are depleted and in the manner the depletion is performed. [62–64]

---

[10] Note that both techniques are still diffraction-limited and obey the Abbe formula (equation (1.1)). Resolution enhancement stems from an enlargened numerical aperture

In a technique termed **absorbance modulation (AM)** a film of photochromic molecules on top of a photoresist is switched between a transparent closed form and an opaque open form using two different wavelengths. [62] If the transformation to the opaque form is saturated in all areas of the depleting beam except for the central part, a tiny aperture is created through which a subdiffraction-sized writing beam may act. This is somewhat different from **resolution augmentation through photo-induced deactivation (RAPID)** where one wavelength is used to initiate polymerization in a negative-tone photoresist and another wavelength saturates the deactivation of the the initiating species. [63] Only one infrared laser is needed for RAPID because the initiation is accomplished with a two-photon process whereas depletion occurs as a one-photon process. The third method presented by Scott *et al.* works similarly to RAPID but uses two individual colors in the blue and UV region, respectively. [64]
While all three techniques provide subdiffraction optical writing of features down to 40 nm the photophysics/photochemistry involved in the RAPID-like methods is still not well understood. This exacerbates the tight control of defined molecular states necessary for RESOLFT techniques. Furthermore, the polymerization deactivating radicals are reactive, short-lived species and have various ways to act on the process adversely. In all cases the sample is prepared as in classical photolithography necessitating the use of specific resists with subsequent washing steps. Therefore sample preparation for these methods can be an intricate task.

Altogether, subdiffraction fluorescence microscopy is a rapidly developing field of research combining ultrahigh resolution with ease of use. Within the set of complementary concepts currently available STED microscopy stands out because it is compatible with conventional fluorophores and standard labeling protocols of biology. Another advantage of STED is its informative value of raw data making it the only purely physical superresolution technique. It therefore is a straightforward idea to utilize this concept also for optical writing beyond the diffraction limit. In this context it would be desirable to finally develop a form of STED lithography that brings together subdiffraction resolution and facile sample preparation.

1.4 Thesis objectives

As the preceding sections have shown STED nanoscopy has emerged as a valuable tool for modern life science combining ultrahigh resolution known from near-field microscopy with ease of use typical for far-field fluorescence microscopy. Gradually approaching macromolecular resolution with STED nanoscopy it becomes feasible to study the relative assembly of differently labeled proteins using two color channels - a major quest of molecular biology. [48,65] This thesis aims at presenting the development of **dual-color STED nanoscopy** with near-macromolecular resolution in both color channels at shortened image acquisition times (chapter 2). [66] Different applications to biological questions as well as the method's combination with a 3D-reconstruction technique will corroborate the setup's functionality (sections 2.3.2 and 2.3.3, respectively). [67,68]

The utilization of high quality fluorescent dyes is of exceptional importance for STED nanoscopy. Chapter 3 therefore presents the **characterization of new fluorinated rhodamine dyes** for use in STED nanoscopy. The good performance of these dyes is evidenced by several superresolved bioimages.

While STED is nowadays an established technique for superresolution optical imaging the method's application potential for optical manipulation of matter has for long time remained unexplored. Only very recently have STED-like techniques been used to improve resolution in photolithography. [62–64] They all, however, require tight control of complex processes such as switching of photochromic molecules or radical polymerizations. A more straightforward approach would take advantage of the basic and well-known STED effect on fluorescent molecules. Only minor design modifications of the dual-color STED setup enable the first ever realization of **STED nanolithography** potentially paving the way for simplified high-resolution optical data storage (chapter 4).

2 Dual-color STED microscopy at 30 nm focal plane resolution

This chapter describes studies towards a substantially improved dual-color STED setup. After outlining the necessity for these efforts and comparing the method with existing techniques a thorough description of the setup is given along with a detailed analysis of experimental data. Using the example of fluorescent nanobeads previously unprecedented dual-color nanoscopy with STED will be evidenced. Thereafter superresolving images of neurofilaments are shown to prove the applicability of the method to biologically relevant systems. Moreover, the first 3D-reconstruction of dual-color STED images and the setup's employment for the elucidation of early steps in the assembly of mouse retina photoreceptor ribbon synapses will be presented.

2.1 Motivation

Owing to its sensitivity, noninvasiveness and 3D-potential far-field fluorescence microscopy [69] is a suitable method to study biological systems. An often recurring problem thereby is the determination of different proteins' relative assembly. In a fluorescence microscope working in confocal mode such spatial correlations can be revealed by imaging differently labeled fluorophores using two (or more) excitation wavelengths. [70] Yet, diffraction sets an upper limit to a confocal microscope's resolution thus impeding a view on the macromolecular scale. The resolution enhancement achieved by STED, however, bears the potential to discriminate between two closely located fluorophore-agglomerations. Hence, a STED setup with ultrahigh resolution in two color-channels could provide a means for substantiated statements concerning protein colocalizations.

Recently, different approaches to accomplish multicolor nanoscopy have been presented. Aside from methods that are based on (conformational) switching and computational localization of individual switchable fluorophores [49–51] the first and - by that time - only dual-color STED microscope was built by Donnert *et al.*. [48] While the former methods may have the advantage of requiring little technical effort STED greatly benefits from the fact of being based solely on photophysical phenomena without the need for any computational postprocessing. [26]

Despite its capability to, e. g., resolve nanoclusters of mitochondrial outer membrane protein Tom20 in relation with the F1F0ATP synthase the resolution of the aforementioned dual-color STED microscope's color-channels is disproportionate. [48] The channel operating with green emitting dyes (termed the "green channel" in the following) has been shown to resolve structures as small as $\approx$ 30 nm. Yet, the channel working with red-emitting dyes (from now on termed the "red channel") displayed only a moderate increase in resolution on the order of 65-80 nm due to technical limitations. When taken into consideration that many important cellular structures such as neurofilaments, have sizes which are significantly smaller than that [71], the need for higher resolution in the red channel of the dual-color STED microscope is clearly obvious.

Additionally, the data acquisition times of dual-color STED images need to appreciably be reduced. Working at a laser pulse repetition rate of 250 kHz in both color channels the recording times of the dual-color STED microscope by Donnert *et al.* are comparatively long potentially leading to, e. g., undesirable sample drift.

In a nutshell, a flexible dual-color STED microscope providing near-macromolecular resolution in both color channels at a reasonably short image recording time shall be developed and shown in experimental practice.

2.2 Experimental implementation

2.2.1 Design considerations

In fluorescence microscopy the choice of the fluorescent dye generally is a crucial parameter as it determines image brightness and (in combination with the used laser source) detrimental photobleaching. [72] For STED microscopy the need for fluorophores with low photobleaching and high quantum yield is even higher because of the intense STED beam that acts on the sample and forces the molecule to undergo multiple cycles between electronic states S_0, S_1 and T_1 (i. e., the ground state, the first excited singlet state and the energetically lowest triplet state, respectively). A suggestive strategy for optimum performance in STED microscopy is therefore to carefully adapt the laser systems to the photochemistry and photophysics of an

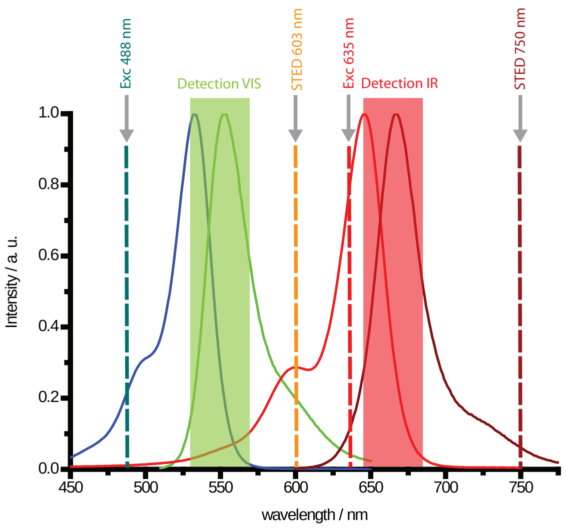

Figure 2.1: Laser lines and detection windows of the dual-color STED microscope in relation to the spectra of the fluorophores Atto 532 (green) and Atto 647N (red).

adequate dye. [66]

STED in the visible range of the electromagnetic spectrum has previously been shown to work well both with synthetic organic fluorophores [65,73] and fluorescent proteins. [74,75] For the dual-color STED studies presented here the organic fluorophores Atto 532 [76] and Chromeo 488 [77] were chosen for the green channel because of their well-known characteristics. The red channel is operated by dyes Atto 647N and Atto 633 [76], respectively, where the suitability of this fluorophore family to perform well in STED microscopy has been demonstrated, as well. [78]

A challenging problem aside from the choice of the dyes lies in the avoidance of cross-talk between the two color channels of the dual-color STED microscope. This means that ideally neither beam of one color channel is able to excite dye molecules of the other color channel. Additionally, the detection scheme has to be chosen such that the fluorescence from one color channel is not misleadingly detected by the other color channel, too. The configuration employed in this work is displayed in figure 2.1. Here, the absorption and fluorescence spectra of Atto 532 and Atto 647N are displayed along with laser lines and detection windows of the dual-color STED setup. The green channel working with Atto 532 is excited at a wavelength of $\lambda = 488$ nm with depleting light at a wavelength of $\lambda = 600$ nm. Analogously, the red dyes are excited at $\lambda = 635$ nm and depleted at $\lambda = 750$ nm. Clearly, cross-talk in the detection is avoided by mounting fluorescence filters which only transmit light of the desired wavelengths. A persisting problem, however, is that the intense STED beam at 600 nm would inevitably excite - and likewise immediately bleach - red-emitting fluorophores if the dual-color image was taken during one individual scan. Following an approach by Donnert *et al.* [48] this problem can be circumvented by scanning the sample sequentially with the red channel first followed by the green channel. This procedure ensures that the two color channels operate completely independent.

After having devised a viable scheme to accomplish dual-color STED microscopy the required light sources have to be chosen attentively. Bearing in mind that the objective is to reach unprecedentedly high resolution in both color channels a prerequisite of the laser system is maximum flexibility in order to exploit the method's whole potential. A laser system consisting of a Nd:YVO_4 pump laser (Verdi V-18, Coherent, USA) and a mode-locked, regeneratively amplified Ti:Sa-oscillator (Mira 900, RegA, Coherent, USA) followed by an OPA (Coherent, USA) is capable of meeting these demands for the green channel as both wavelength and repetition rate can be varied extensively in a range from 10 kHz to 300 kHz and 500 nm to 700 nm, respectively. It has been shown previously that the *triplet/dark state-relaxation* (D/T-Rex) modality significantly reduces photobleaching at a repetition rate of 250 kHz thus tolerating higher STED powers. [79] This is due to enlarged interpulse time intervals giving the molecule enough time to abandon bleaching-prone dark states. Therefore only minor changes in the tuning of the laser system are necessary for the green channel including the optimization of the regenerative amplifier's (RegA) wavelength to λ = 800 nm.

Red-emitting fluorescent dyes with fairly low triplet formation and triplet bleaching (e. g., Atto 633 or Atto 647N) relax the need for a technically demanding T-Rex modality at low laser repetition rate in the red channel. In order to maintain flexibility concerning the used STED wavelength it is reasonable to stick to pulsed lasers because simpler CW systems have proven to be powerful in STED microscopy [22] but are mostly not tunable. Since a STED wavelength of $\approx$ 750 nm is envisaged a standard Ti:sa-oscillator (Verdi V-10, Mira900, Coherent, USA) appears to be a good choice. Working at a repetition rate of 76 MHz this laser substantially shortens pixel dwell times so that the overall image acquisition time is reduced by an order of magnitude as compared to a T-Rex scheme.

2.2.2 The optical setup

The light sources described in section 2.2.1 constitute the fundament of an optical setup for dual-color STED microscopy. Figure 2.2 depicts the optical design of the microscope. The pulses of the STED beam for the green color channel are centered around a wavelength of λ = 600 nm. The light is provided by a laser system based on a frequency-doubled cw

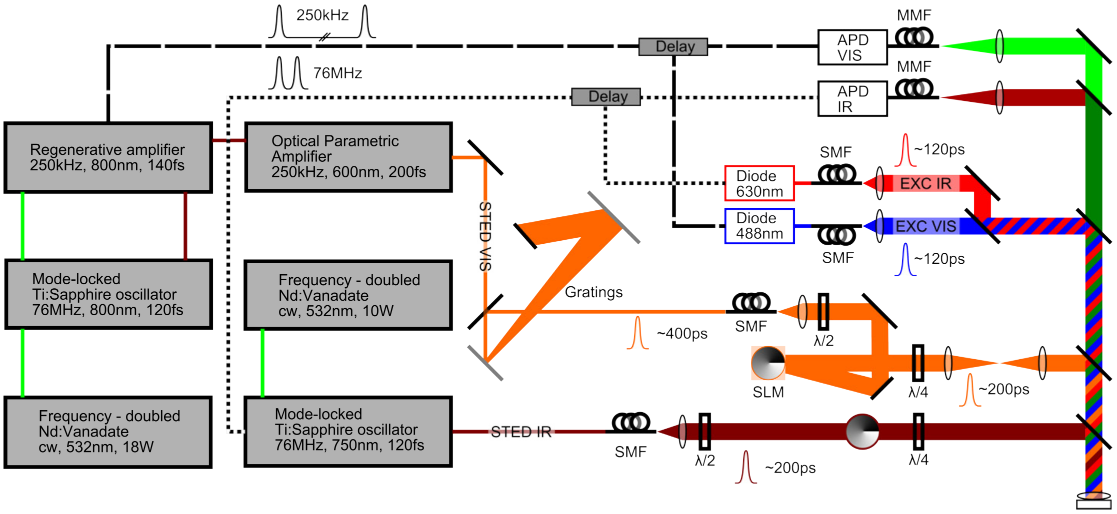

Figure 2.2: The optical setup of the dual-color STED microscope.

Nd:YVO$_4$ laser (Verdi V-18, Coherent, USA) working at a wavelength of 532 nm and an output power of 18 W. The light is split with 7 W pumping a femtosecond Ti:sa-laser (Mira900, Coherent, USA) and 11 W feeding a regenerative amplifier (RegA9000, Coherent, USA). The output pulses of the RegA are characterized by a duration of 140 fs at a repetition rate of 250 kHz and a wavelength of 800 nm while the output power is $\sim$ 1.4 W. Half of this light is then used to pump an optical parametric amplifier (OPA9400, Coherent, USA) which converts the wavelength to $\sim$ 600 nm ($\tau_{\text{pulse}} \approx$ 200 fs). After passage of a gratings line to prestretch the pulses to approximately 400 ps the light is coupled into a 1.5 m long single-mode fiber (Schäfter und Kirchhoff, Germany) for spatial cleanup of the beam shape. Chirp compensation within the fiber causes the pulses to get slightly compressed to $\sim$ 200 ps which is a suitable pulse duration for the STED beam. The beam is then directed towards a spatial light modulator (Hamamatsu, Japan) in order to imprint a helical 0-2 π phase ramp on the wavefront entering the objective lens for the typical donut shape of the STED PSF (compare figure 2.3). [65] Since it has been shown that circularly polarized light most effectively allows for 2D-superresolution in STED microscopy [24,80] this polarization is ensured through two wave plates - a half wave plate in front of the SLM and a quarter wave plate behind it. A 4-f setup is incorporated to ensure that the SLM's surface is correctly imaged to the back aperture of the microscope's objective lens.

Another femtosecond Ti:sa laser (Mira900, Coherent, USA) pumped by a 532 nm cw Nd:YVO$_4$ laser (Verdi V-10, Coherent, USA) emits pulses of 120 fs duration around a central wavelength of λ = 750 nm. This light is supposed to serve as the STED beam for the red channel. At the output of a 80 m long single-mode fiber (Thorlabs, USA) the pulses are stretched to 150 ps due to dispersion within the fiber. In contrast to the green channel a polymer phasemask is chosen to impart the necessary phase retardation for the donut shape of the STED beam. This has some advantages compared to the use of a SLM: Apart from being significantly cheaper the polymer plate allows for a more compact setup design as well as for higher average powers which could be important for cw-STED implementations. [22]

The respective excitation beams are delivered by two separate laser diodes (Picoquant, Germany) working at 488 nm and 635 nm, respectively. Triggering the excitation diodes to the STED lasers via an electronic delay box renders possible to temporally shift the pulses thus gaining an optimum STED effect.

In this dual-color STED implementation four beams of wavelengths covering nearly the whole visible spectrum need to be superimposed. A loss-free configuration therefore is a truly challenging task when taking into account that additionally two fluorescence wavelengths need to be guided, as well. Such an experimental setup imposes high demands on the optics in use. Here, spatial overlap is accomplished by a combination of dichroic mirrors (AHF Analysentechnik, Tübingen, Germany and Mikroschicht Optik GmbH, Jena, Germany) with just the right optical characteristics to avouch a maximum of detected fluorescence.

In order to tightly focus the beams onto the sample a high-NA microscope objective lens has to be used. For the work presented here an oil-immersion objective lens with NA = 1.4 was chosen (Leica, Germany). Back-emitted fluorescence is collected by the same objective and reaches the detector after passing through the dichroic mirrors. The images are recorded by line-scanning the sample with a piezo-stage (NanoMax, Melles Griot, Germany) across the fixed beams.

Fluorescence photons are detected by single-photon-counting avalanche photodiodes (APD, Perkin Elmer Optoelectronics, Canada) via multi-mode fibers with a diameter of 62.5 μm. These fibers thus allow for confocal detection of the fluorescence. Under consideration of the excitation beams' PSFs (compare figure 2.3) the sizes of the pinholes correspond to 0.73 Airy disks in the green channel and 0.53 Airy disks in the red channel, respectively, which is close to the benchmark value of 0.63. [81] To completely discard non-fluorescent light suitable band-pass-filters are placed in front of the fibers (520/40 or 545/50 and 670/40, AHF Analysentechnik, Tübingen, Germany).

A time-correlated single photon counting (TCSPC) board (Becker and Hickl, Germany) analyses the APDs' signals and the custom-built software package 'Imspector' controls the measurement.

In the green channel the detection is gated which means that signals are merely detected within a certain time window of - in our case - 25 ns. If this time window is synchronized to the excitation pulses this has the distinct advantage of detecting fluorescence only because organic fluorophores typically exhibit fluorescence lifetimes of $\sim$ 1-3 ns. Most of the noise occurring during the comparatively long interpulse time of 4 μs (for a laser working at a repetition rate of 250 kHz) is therefore discarded. This procedure makes sense if there is only a short signal period within a certain time interval - as is the case if the repetition rate of the laser is low. Therefore an analogous configuration is not needed for the red channel which works at a significantly higher repetition rate.

For an enlarged field of view on the sample a wide-field microscope based on a CCD camera is also incorporated into the optical setup (not explicitly shown in figure 2.2). This considerably simplifies the quest of locating regions of interest within a sample.

2.2.3 Characteristics of the setup

Having constructed an optical setup it is useful to subsequently characterize it thoroughly with respect to parameters such as power and spectra. In the case of a microscope the point spread function (PSF) is characteristic for each setup and provides a good measure for predicting its performance. Very briefly, a PSF ς mathematically describes the spread of radiant flux from $\mathrm{d}y\,\mathrm{d}z$ to an image point so that the according flux density corresponds to

$$\mathrm{d}I_i\,(Y,Z) = \varsigma\,(y,z;Y,Z)\,I_0\,(y,z)\;\mathrm{d}y\,\mathrm{d}z \tag{2.1}$$

If the light source is incoherent the flux-density contributions from each of its elements are additive, so

$$I_i\,(Y,Z) = \iint\limits_{-\infty}^{\infty} I_0\,(y,z)\,\varsigma\,(y,z;Y,Z)\;\mathrm{d}y\,\mathrm{d}z \tag{2.2}$$

In the absence of any kind of aberration $\varsigma\,(y,z;Y,Z)$ corresponds in shape to the diffraction figure of a point source at (y,z). [1] Aberrations caused by deficient optics or misalignment of the setup will broaden and/or distort the PSF leading to a blurred image. Moreover, there is a strong interrelation between the PSF's quality and the resolution capabilities of

---

[1] The derivation of equations (2.1) and (2.2) is described, for instance, in reference [82].

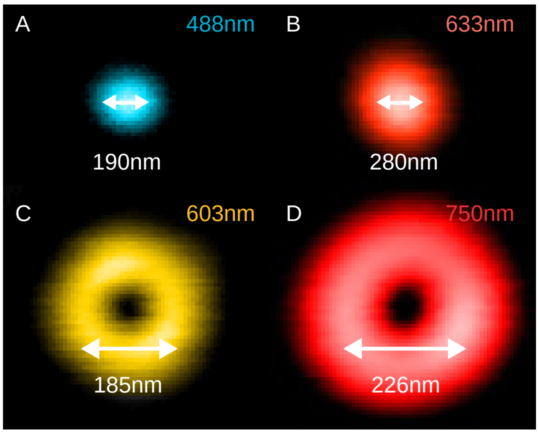

Figure 2.3: PSFs of the dual-color STED setup. (A): Excitation PSF of the green channel (λ = 488 nm). (B): Excitation PSF of the red channel (λ = 633 nm). (C): STED beam of the green channel (λ = 603 nm). (D): STED beam of the red channel: (λ = 750 nm). Numbers correspond to measured FWHM.

the imaging system. Through knowledge of a system's PSF one can therefore assess its imaging behaviour. In practice, the determination of a PSF is not a trivial task as in the above explanations point light sources are assumed which are naturally not available. Yet, a good approximation to the true PSF of a confocal microscope can be made if very small light sources are used. In our case colloidal gold nanoparticles with a diameter of 80 nm are chosen as pseudo light sources. Under focused irradiation the nanoparticles scatter light through the objective lens which can be detected with a PMT. By raster-scanning the sample around the nanoparticle an image is created that nearly reflects the setup's true PSF. [83, 84] Figure 2.3 displays the lateral PSFs of the dual-color STED setup presented in figure 2.2. While the two topmost PSFs belong to excitation beams with wavelengths of λ = 488 nm and 633 nm, the two donut-shaped PSFs correspond to STED beams at λ = 603 nm and 750 nm, respectively. With FWHM of 190 and 280 nm the shapes of the excitation beams are close to the theoretical limit of the according noise- and aberration-free PSFs (FWHM = 174 nm and 226 nm). The symmetry of the PSFs in figure 2.3 is comparatively high which also suggests that perturbing aberrations are more or less absent. Since in the described setup four beams spanning a large wavelength range need to be spatially overlapped and focused through the objective a complete absence of chromatic aberration cannot be achieved. As a compromise the STED beams which require optimum shape of the PSF are aligned perfectly whereas the excitation beams are slightly de-collimated so that focusing of all beams on one distinct spot is possible. In this manner small spherical aberrations are introduced to the

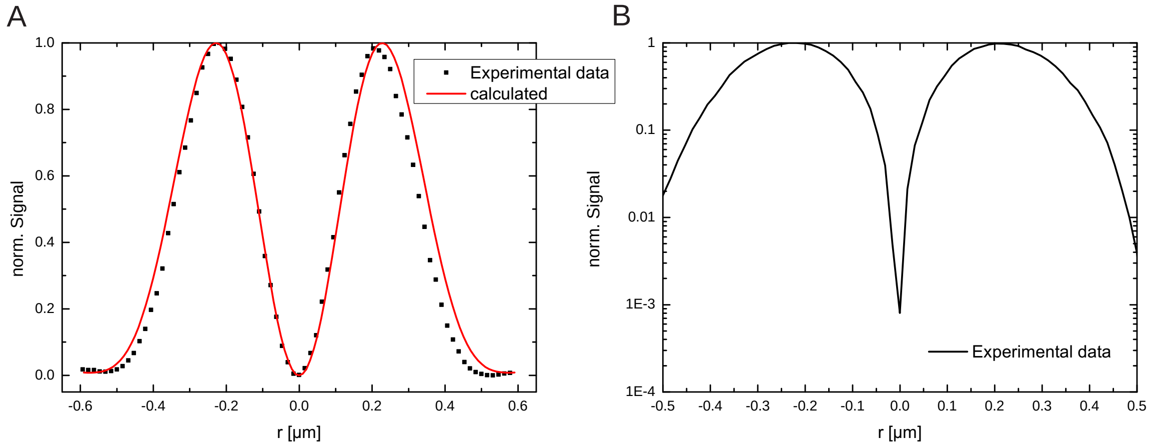

Figure 2.4: Line profile of the IR-donut at $\lambda = 750$ nm. (A): The scattered points correspond to measured and the red line to calculated data. (B): Logarithmic delineation of measured data.

wavefronts of the excitation beams. But figure 2.3 proves that this effect is fairly small and does not distort the shape of the PSFs significantly.

Just like in confocal microscopy the excitation PSF is important in STED microscopy, as well. However, for the latter method the significance of the STED beam is even higher because of its high intensity. Especially, remaining intensity in the center of the donut is known to deteriorate image quality in STED microscopy. For instance, a remaining signal of only 0.3% in the minimum results in a reduction of the peak intensity by 25% if a STED intensity is applied that brings about a resolution enhancement of factor 10 compared to confocal microscopy. [85] Hence, it is advisable to examine the donuts of figure 2.3 a little closer. In figure 2.4 the line profile of the IR-STED donut (figure 2.3 (D)) is shown. The comparison between experimental and calculated data in (A) clearly shows that the shape of the utilized donut is close to optimal. Especially in the crucial region around the central zone the accordance is very good. Small deviances on the beam's outer part may stem from weak spherical aberrations. In order to further analyse the zero intensity zone a logarithmic delineation of the experimental data is given in (B). It can be estimated from the experimental data that there is a remaining signal intensity of less than 0.1% which corresponds to the noise level. Consequently, it can be expected that - when used for optical imaging with STED - the setup's resolving capabilites will be nearly optimal.

Aside from checking and optimizing the setup's PSFs another important characteristic of a STED setup (or rather of a STED setup in combination with a certain dye) is the efficiency with which a molecule is de-excited from a fluorescent state by the application of a STED beam. In the introductory chapter the dependence of fluorescence inhibition on the applied STED intensity has been described. If $\mathrm{F_{STED}}$ is the amount of fluorescence under exposure to a stimulated emission beam with intensity $\mathrm{I_{STED}}$ and $\mathrm{F_{exc}}$ the fluorescence invoked by the exciting beam only, we can define $\eta = \frac{\mathrm{F_{STED}}}{\mathrm{F_{exc}}}$ as the fraction of remaining fluorescence in case of a switched on STED beam. Augmenting $\mathrm{I_{STED}}$ reasonably drives the transition $\mathrm{A} \rightarrow \mathrm{B}$ where A is a fluorescent and B is a non-fluorescent state (usually the ground state). For temporally separated excitation and inhibition light, after averaging over the dye's orientation, the suppression factor can usually be well approximated by an exponential

$$\eta \propto e^{-\ln 2 \cdot \mathrm{I_{STED}}/\mathrm{I_{sat}}} \tag{2.3}$$

where the saturation intensity $\mathrm{I_{sat}}$ denotes the value of $\mathrm{I_{STED}}$ where half of the initial fluorescence is depleted. [85] This value is an intrinsic property of the used fluorescent substance and is a function of the orientational distribution and rotational behavior of the dye molecules, as well as the wavelength, temporal structure, and polarization of the inhibition light. [85] The interconnection between $\mathrm{I_{STED}}$, $\mathrm{I_{sat}}$ and the FWHM Δx of a resulting spot in STED microscopy is

$$\Delta x \propto \lambda / n\sqrt{\xi} \tag{2.4}$$

with

$$\xi = \mathrm{I_{STED}}/\mathrm{I_{sat}} \tag{2.5}$$

where λ is the inhibition wavelength, n the refractive index and ξ the saturation factor. Consequently, the acquaintance of ξ can give a good estimate of the resolution achievable with the present experimental setup. [2] Therefore a so called "depletion curve" - η as function of $\mathrm{I_{STED}}$ - is recorded to smoothly test the system's capacity. In figure 2.5 such a curve is shown for an aqueous solution of dye Atto 633 at a STED wavelength of λ = 780 nm. Reading off the saturation intensity $\mathrm{I_{sat}}$ from experimental data yields a value of approximately 377 MW/cm^2. This, however, is by far larger than reported elsewhere in similar experiments where $\mathrm{I_{sat}} \approx 7\ \mathrm{MW/cm^2}$. [78] An explanation for this discrepancy lies in the preparation procedure of the sample. The dotted curve of figure 2.5 was obtained with a sample containing a reservoir of aqueous dye solution which is a very convenient way of sample preparation and mostly gives good indications on the functional capability of the

---

[2] It is to be noted that the FWHM of a resulting spot is not fully equivalent to the system's resolution. Aside from the PSF resolution is determined by the object itself and the signal-to-noise ratio, as well. Generally, resolution is better described by *Lord Rayleigh's criterion* or - more rigorously - by *Sparrow's condition*. [82]

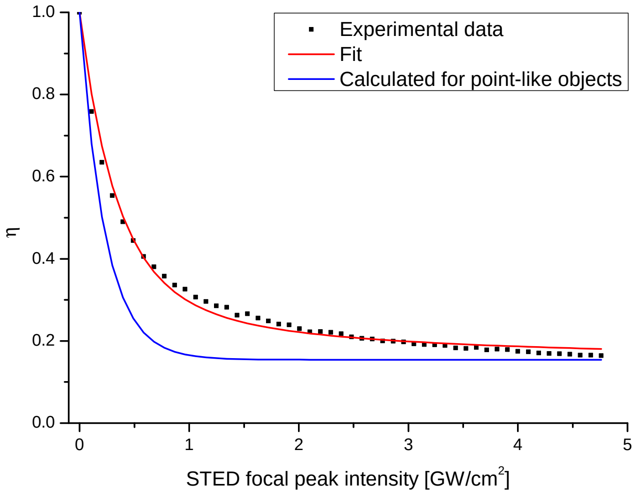

Figure 2.5: The depletion curve of an aqueous solution of dye Atto 633 measured with the red channel of the dual-color STED setup. η is the fraction of remaining fluorescence under stimulated emission depletion. Experimental data (dotted) is fitted by an exponential function of type equation (2.3) (red line). Fitted parameters are then used to calculate the depletion curve in the case of point-like emitters (blue line).

experimental setup. For example, it can immediately be recognized whether full depletion saturation is accomplished through STED and to which extent different dyes can be depleted relative to each other. Such information is sufficient in most cases and also for the purpose of characterising a setup. Yet, the outcome of such an experiment cannot be considered quantitative for several reasons. Most importantly, in a thick aqueous dye solution the entire focus area is tightly filled with fluorescent molecules. This causes the STED effect to vary in magnitude depending on the particle's position relative to the STED PSF. While molecules near the center of the PSF can be depleted almost completely, the effect is much smaller for fluorophores situated in the focal periphery. In total this 3D-issue may misleadingly indicate a low overall stimulated emission depletion and explains why the graph in figure 2.5 does not further decay than approximately $\eta = 0.15$. [3] The red line in figure 2.5 therefore shows the result of a fit to equation (2.3) under consideration of this issue. Here, a three-dimensional, effective PSF was computed to model the situation of superimposed excitation and STED PSFs in a large fluorophore-filled volume. Obviously, the fit nicely reflects experimental reality.

To completely avoid the problem of recording experimental data which is averaged over a

---

[3] Fast diffusion of molecules in and out of the focus during data recording may also contribute to the high background.

PSF fluorescent nanoparticles could be used which are smaller in size than the PSF and depletion thus takes place only in the central part of the PSF. [86] Ideally, single emitters were to be employed since in this case a logical ‘on’ and ‘off’ situation could be generated and after recording enough photons η would directly reflect the probability of a molecule to remain fluorescent. [87, 88] This procedure, however, is somewhat elaborate and time-consuming. Fortunately, a reliable and relatively simple workaround can be performed by using the fitted parameters of figure 2.5. Decomposing the effective PSF into hypothetical PSFs with varying intensities and using the previously fitted parameters yields a multitude of depletion patterns. The weighted average of which will then model the depletion curve that would have been obtained with single emitters. Such a curve is shown as the blue line in figure 2.5. The resulting value of $\mathrm{I_{sat}}$ = 159 MW/cm^2 reflects the ‘true’ saturation value much better. Still, the value is comparatively high which is a consequence of reusing the fitted parameters describing the decay of the experimental data (red curve in figure 2.5) for the simulation of the curve that would have been obtained with point-like emitters (blue curve in figure 2.5).

For the purpose of this work, namely to develop and construct an optimized superresolving dual-color setup, the depletion curve of figure 2.5 provides the desired information that the setup’s IR channel clearly reaches STED intensities far beyond $\mathrm{I_{sat}}$. This especially holds when taking into account that for the reasons given the actual value of $\mathrm{I_{sat}}$ is much smaller than measured.

2.3 Results

In the preceding sections the route to a dual-color STED setup has been disclosed and some characteristical features of the constructed optical setup have been highlighted. Technical expertise gained from there strongly suggests an efficiently working dual-color STED nanoscope with a significantly improved resolution of the red channel.

This section aims at comprehensively presenting results obtained with the setup. Starting from fluorescent nanobeads which prove to be suitable test objects to explore the system’s ultimate resolving capabilities (section 2.3.1) the discussion will expand upon imaging of biologically relevant neuronal systems in section 2.3.2. In section 2.3.3 the so far first 3D-reconstruction of high-resolution STED images will be presented. Finally, section 2.3.4 deals with the successful application of the setup in a study of the involvement of presynaptic proteins during early steps in the formation of photoreceptor ribbon synapses in mouse retina.

A listing of relevant measurement parameters such as pulse energies and sample preparation procedures can be found in the appendix (Tab. A.1).

2.3.1 Dual-color superresolution with fluorescent nanobeads

Fluorescent nanobeads are small spherical particles with diameters in a broad range between 20 nm and several micrometers. They are mainly made of silica or polystyrene labeled with proprietary dyes and are mostly dispersed in water upon purchase. Carboxylate-modification of the surface also allows for covalent attachment of ligands if desired. Not only for STED microscopy have these particles proven to be very useful as they represent well manageable test objects to illustrate the capability of an imaging method. [89–91] The beads chosen for this work are yellow-green and crimson fluorescent, respectively, with diameters of 24±4 nm (Invitrogen, USA). In addition to their narrow size distribution these beads feature very stable and bright dyes with absorption/emission characteristics which resemble the dyes used for immunolabeling of biological samples. In addition, sample preparation is fairly easy and well reproducible. All in all these nanobeads appear to be well suited for a systematical investigation of the dual-color STED microscope's performance.

Figure 2.6 displays the image of a 1:1-mixture consisting of yellow-green and crimson beads recorded with the dual-color STED setup described in section 2.2. Images (B) and (C) correspond to raw and nonlinearly deconvolved STED data whereas the blurred picture in (A) was taken in confocal mode. It is visible to the naked eye that the STED images excel in sharpness with individual beads being clearly distinguishable. It is important to note that the resolution gain is reached by an all-physical method without the need for computational image reconstruction. Further deconvolution of the data with an estimated effective PSF (see section A.2 for an explanation) merely smoothes the images and reduces noise. For figure 2.6 (D) the images of 22 crimson and 16 yellow-green beads have been overlaid. A custom-built algorithm is then used to generate averaged bead shapes. The FWHM of which are shown by the line profiles and evidence a resolution of at least 33 nm in the red channel and 31 nm in the green channel, respectively. Figure 2.6 (E) illustrates the resolution enhancement by magnifying the boxed area of figure 2.6 (A) and comparing the confocal image with the deconvolved STED image. Due to the diffraction-limited PSF the entire area is color-filled in confocal mode whereas the contributing beads can manifestly be discerned in the STED picture.

Compared to the first implementation of two-color STED microscopy a further doubling of the red channel's resolution has been achieved. [48] As already explained in section 2.2.1 the improvement originates from adapting the light source to the photophysics of the dye.

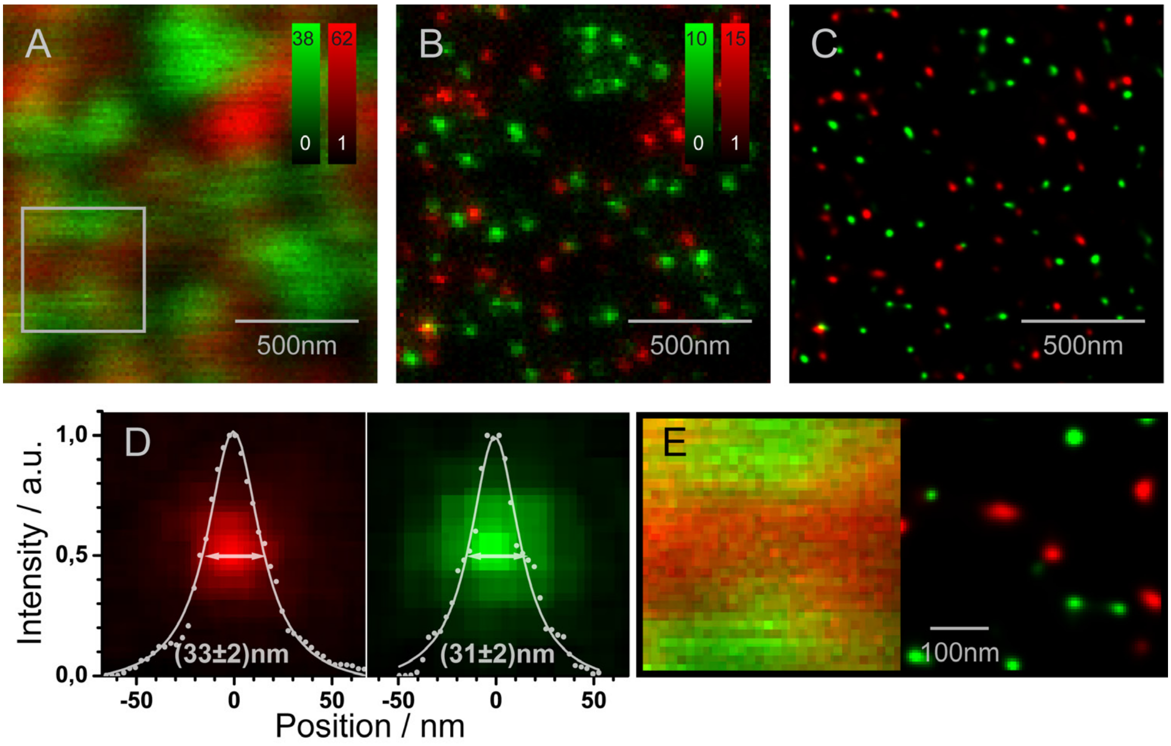

Figure 2.6: Confocal (A), raw (B) and nonlinearly deconvolved (C) STED image of fluorescent nanobeads (1:1-mixture of crimson and yellow-green beads). (D): Line profiles through averaged raw STED data taken from several beads reveal a FWHM of $\sim$ 33 nm and $\sim$ 31 nm for the red and the green color channel, respectively. (E): Magnified view of the boxed region in (A) and (C), highlighting the gain in resolution.

Concretely, the cognition that dyes like Atto 647N and Atto 633 merely show minor population of the bleaching-prone triplet state redundantizes a complex T-Rex implementation with a low repetition rate laser in the red color channel. For such technical reasons the setup built by Donnert *et al.* was not capable of using STED wavelengths below 780 nm which is rather inefficient for the mentioned dyes (compare figure 2.1). The setup presented here employs a standard Ti:Sa-laser at λ = 750 nm for fluorescence inhibition. Considering the fact that the cross section for stimulated emission is proportional to the fourth power of the applied wavelength (compare equation (4.11)) such a reduction truly boosts the STED effect and enables much better resolution in imaging.

It is momentous to understand that the measured FWHM of 33 nm and 31 nm for the red and green channels of the dual-color STED microscope represent an upper bound to the true resolution. To explain this fact in some more detail we should bring to mind the process of image formation in the confocal and STED microscope, respectively. The confocal PSF h_{conf} results from multiplication of the excitation PSF h_{exc} with the convolution product of detection PSF h_{det} and pinhole shape ph :

$$h_{\text{conf}} = h_{\text{exc}} \cdot (h_{\text{det}} \otimes \text{ph}) \tag{2.6}$$

If the confocal PSF is superimposed by a STED PSF (with the donut shape of figures 2.3 C and D, for example) the resulting STED image is formed by an effective PSF h_{eff}, the size of which being dependent on the applied inhibition power according to equations (2.4) and (2.5). Thus, the effective PSF h_{eff} is the product of h_{conf} and the fraction $\eta\left(r\right)$ of remaining fluorescence in case of a switched on STED beam at each point r on the PSF,

$$h_{\text{eff}} = h_{\text{conf}} \cdot \eta\left(r\right) \tag{2.7}$$

Figure 2.7 illustrates this situation. As depicted in figure 2.8 the image itself is a convolution of object and effective PSF,

$$\text{Img} = \text{obj} \otimes h_{\text{eff}} \tag{2.8}$$

Because we know that the product of a convolution will always be larger than its (nonnegative) components, it is justified to state that the measured FWHM of a non-pointlike object is always larger than the effective PSF. Using the example of crimson-fluorescent nanobeads measured with the red channel of the dual-color STED setup a measured FWHM of 33 nm corresponds to an effective PSF of only 30 nm full width half maximum as shown in figure 2.8. Hence, the true resolution of the system is even better than indicated by the measured FWHM.

2.3.2 Unprecedented resolution of double-stained neuronal proteins

The preceding section has proven that our dual-color STED microscope is capable of resolving structures as small as 30 nm. Yet, these measurements were performed on fluorescent nanobeads which indeed are useful test objects but lack any particular research interest. Aside from being interesting in itself a newly developed method must also be measurable against the needs of potential fields of application. Perhaps the greatest promise of fluorescence nanoscopy lies in the observation of previously unresolved structural details in biological processes at the cellular and molecular scale. [39] It is thus consequentially that the next incremental step in the development of dual-color STED microscopy involves its application to such systems.

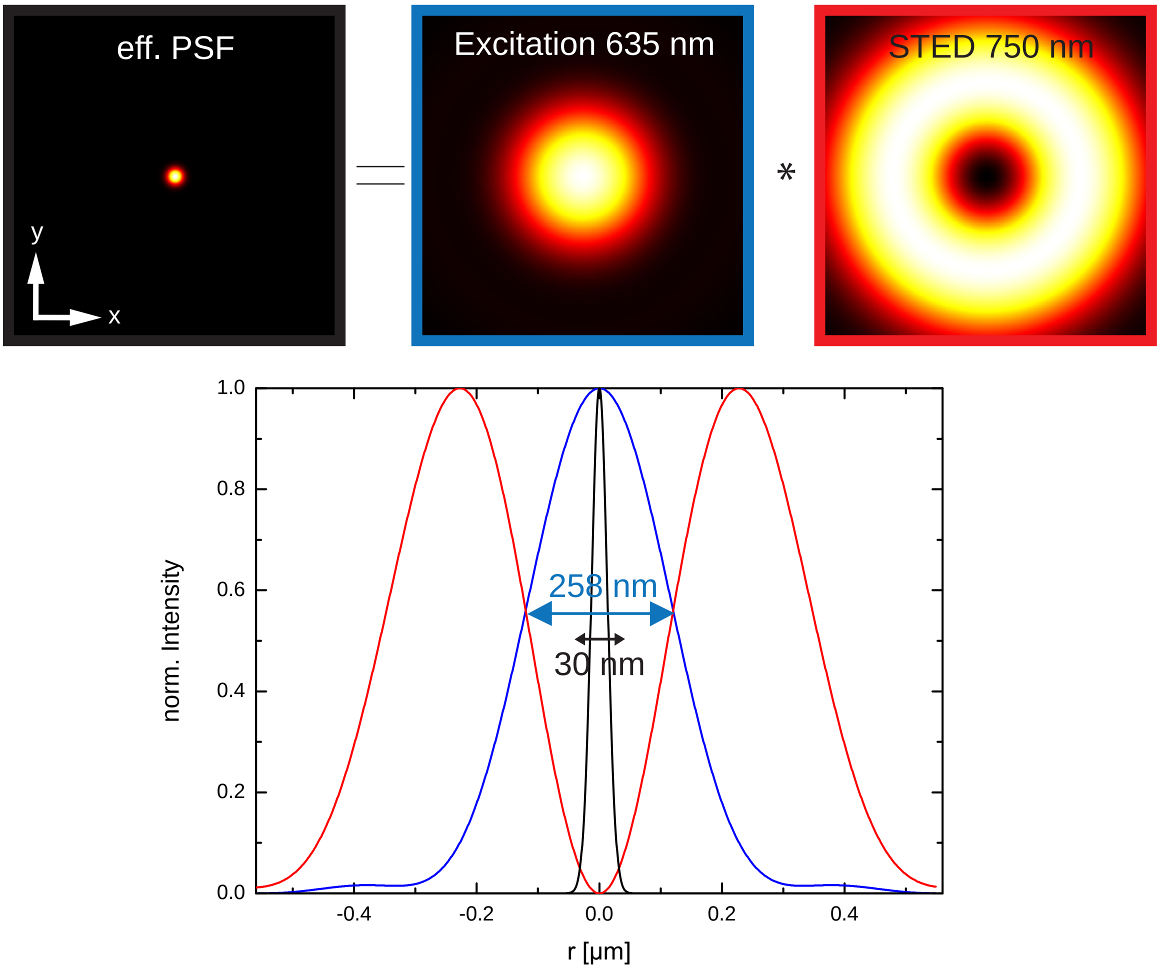

Figure 2.7: The effective PSF results from multiplication of the confocal excitation PSF and the STED PSF. It has a FWHM of only 30 nm as compared to 258 nm for the confocal PSF assuming the displayed wavelengths and the resolution capability measured in the bead measurements.

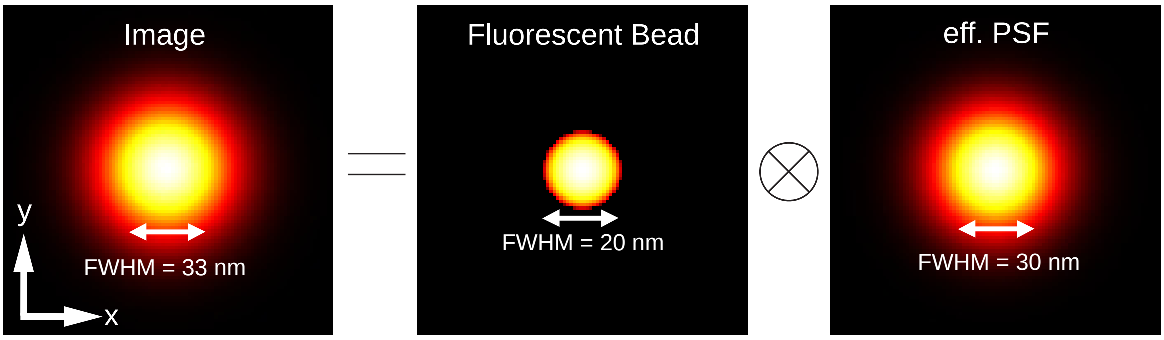

Figure 2.8: An image is the convolution product of object and effective PSF. STED measurements on beads yielded a FWHM of 33 nm which is consistent with an effective PSF of FWHM = 30 nm if a crimson-fluorescent bead with a diameter of 24 nm (FWHM = 20 nm) is considered.

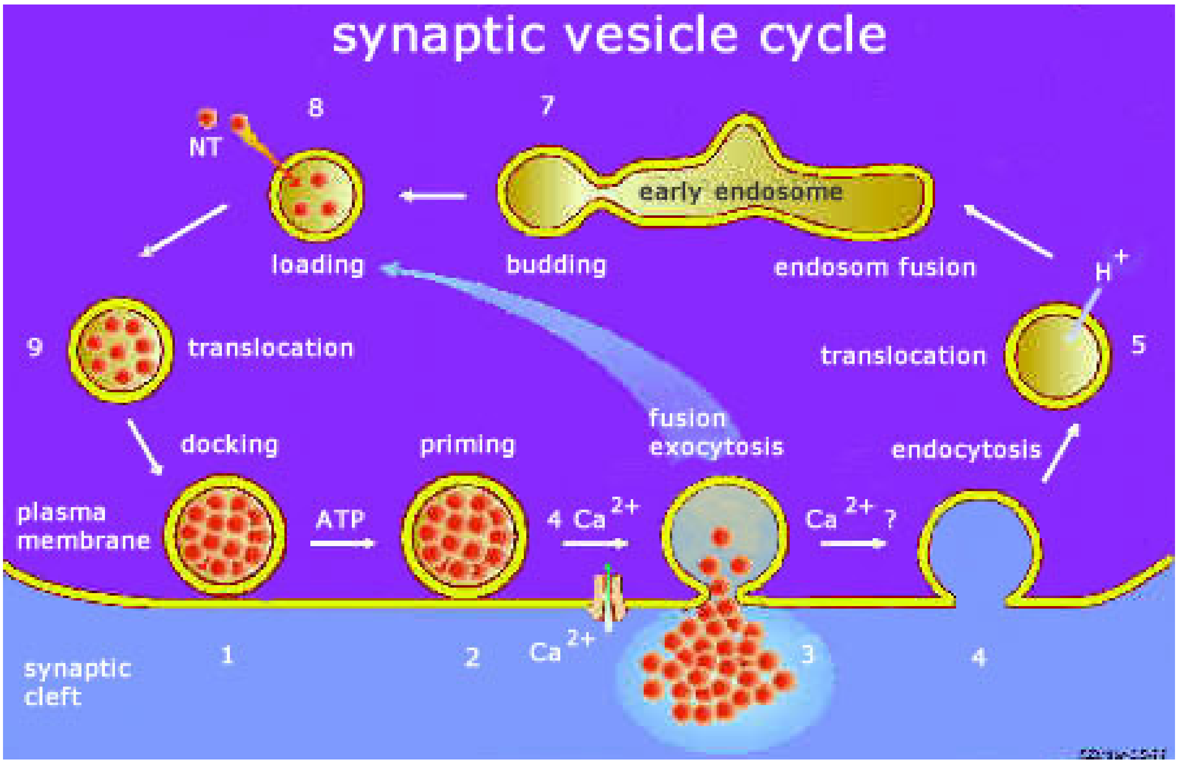

Figure 2.9: Illustration of the synaptic vesicle cycle. After Ca^{2+}-mediated neurotransmitter (NT) release (step 3) the synaptic vesicle is finally recycled and capable of loading new neurotransmitters (step 8). Image taken from ref. [93].

Synaptic vesicles are tiny secretory vesicles that can be found in nerve cells. Their function is to store neurotransmitter molecules (e. g., Acetylcholine, glutamate, glycine) which contribute to fast signal transmission at chemical synapses. An action potential leads to a rise of the Ca^{2+} concentration in the presynapse via voltage-gated calcium channels. The increase of the Ca^{2+} concentration then triggers transmitter release. After having released the neurotransmitters the vesicles need to be recovered quickly which is accomplished by local recycling from the plasma membrane of the nerve terminals. Figure 2.9 illustrates this process which is known as the synaptic cycle. [92] For a review of state-of-the-art research in this field reading reference [94] is recommended.

As the synaptic vesicles are approximately 50 nm in diameter they are not resolvable with conventional confocal microscopy. Hence, for an investigation of these objects high-resolving methods like electron microscopy have been employed. [95] This however bears the intrinsic disadvantage of being 3D-compatible only with major efforts (e. g., through electron tomography) [96] and live-cell imaging is not possible in that way. STED microscopy, on the other hand, offers the necessary resolution without suffering from the mentioned drawbacks. This clearly renders it a good choice to study synaptic vesicle systems.

Synaptophysins are a class of synaptic vesicle proteins that may regulate SNARE [4] function at the synapse. [94] Syntaxin 1, on the other hand, is a protein of the plasma membrane involved in neurotransmitter release. [97] We examined this system to demonstrate dual-color STED imaging with unprecedented resolution for biological imaging. [5] Samples were prepared from cultured hippocampal neurons of neonatal rats. Since the microscope does yet not provide enhanced resolution along the optical axis the samples were mechanically sliced to yield very thin sections with a thickness of $\sim$ 100 nm. [68] It is thus possible to achieve notably sharper images because no out-of-focus fluorescence is collected by the confocal z PSF. [6] Figure 2.10 compares the confocal with the STED image of Atto 532-labeled syntaxin 1 and Atto 633-labeled synaptophysin. [7] Apparently, the STED images (B) and (C) unfold structural details that remain concealed in the confocal image (A). It can be observed that both the STED raw data (E) and the deconvolved image (F) reveal protein clusters of 41-nm distance (G). Single red antibodies imaged with the red channel of the microscope exhibit full width half maxima of approximately 33 nm. When taking into consideration that that the effective PSF of the microscope is larger than the size of these tiny particles it can be inferred that the resolution of the red channel is <35 nm. Thus, the dual-color STED setup opens up new perspectives to study the spatial distribution of these proteins. The images suggest that the proteins appear to cluster in different areas in the cells. This is not surprising as the proteins are mostly located in different structures of the synapse. Conventional imaging techniques are unable to resolve the location of the proteins due to the spatial confinement of the synapse.

In the lower left corners of figures 2.10 (A-C) ring-like structures containing red and green fluorophores are located. These structures are 300 nm silica beads double-stained with Atto 532 and Atto 633 which were coembedded along with the cells to serve as anchor points during overlay of green and red images. [8] Interestingly, the beads nicely exemplify two associated features of figure 2.10: Firstly, the ring-like structures stem from the fact that the

---

[4] SNARE-proteins are key factors for the fusion of biological vesicles allowing specificity in recognition and katalysing the fusion.

[5] Colocalization of Synaptophysin and Syntaxin 1 could reveal a spatial proximity of vesicles and membrane. A thorough colocalization analysis, however, was not the aim of the presented work. Rather, it focuses on method development demonstrating the potential of dual-color STED nanoscopy.

[6] This technique and its application to 3D-image reconstruction will be further discussed in section 2.3.3.

[7] For reasons of simplicity the color channels are sometimes termed ‘green’ and ‘red’. A compendium of the used dyes for the dual-color images can be found in section A.3. Protocols of cell culture and immunocytochemistry are also given there.

[8] This procedure is further explained in section A.1.

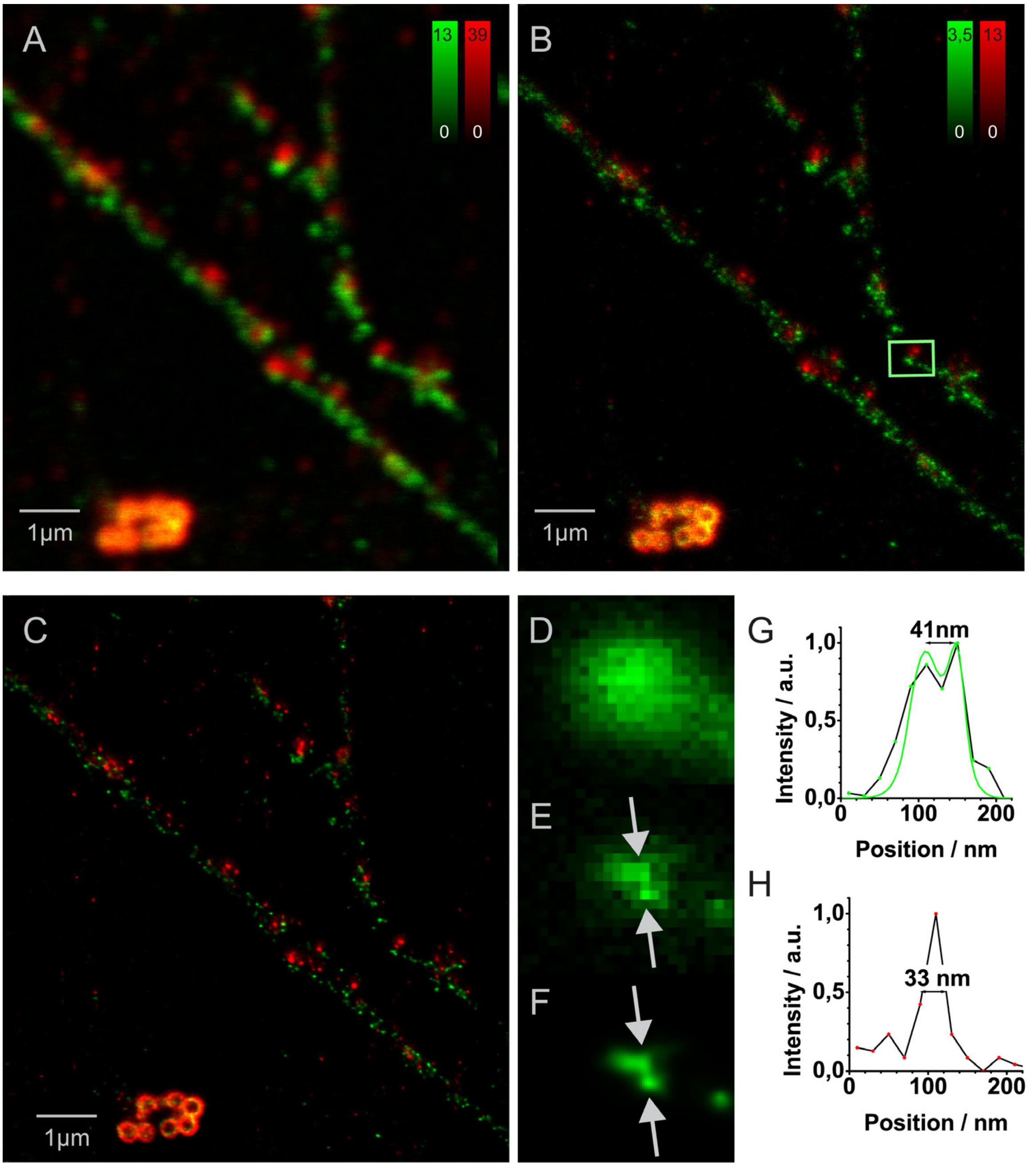

Figure 2.10: Synaptic proteins synaptophysin (red) and syntaxin 1 (green) in neurons. (A) confocal image, (B) STED raw data, and (C) STED image after nonlinear deconvolution. (D-F) Extract of the green channel of the boxed area in (B). (G) Corresponding line profiles through the structures in (E) and (F). (H) Profile of a dye-conjugated antibody or antibody complex.

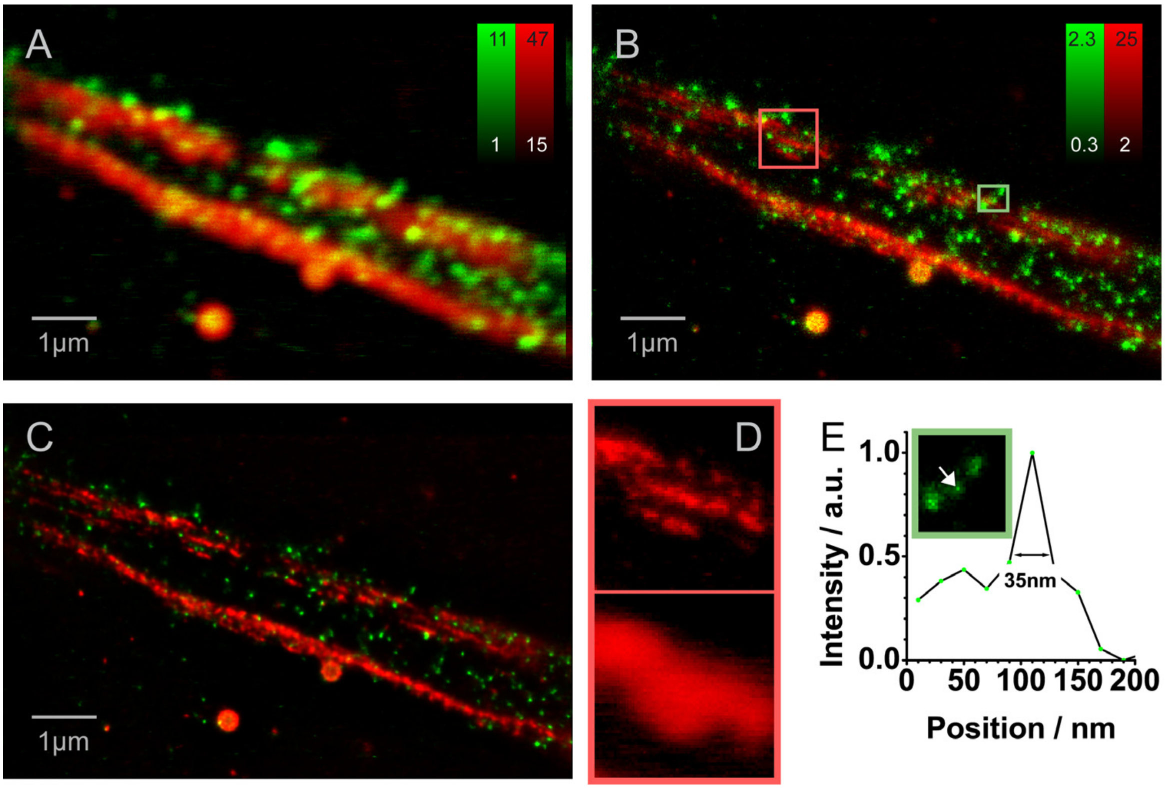

Figure 2.11: (A) Confocal, (B) STED and (C) nonlinearly deconvolved STED images of Neurofilament-L (green) and α-internexin (red). (D) shows an outtake of the red box in (B) comparing STED and confocal imaging while the line profile in (E) belongs to the green box in (B).

beads get cut during sample sectioning. And secondly, clear resolution of the ring-structures only succeeds with STED microscopy. With confocal microscopy the sectioned beads could easily be confused with entire beads.

One might perhaps argue that it is indeed the sectioning procedure that permits clear comprehension of the highly three-dimensional neurons in figure 2.10. Notwithstanding the obvious advantages of this technique dual-color STED microscopy of neuronal proteins is as well possible with unsliced samples as can be seen in figures 2.11 and 2.12. Here, neurofilament light subunit and α-internexin in entire (nonsliced) fixed differentiated neuroblastoma cells are imaged. Along with actin microfilaments and microtubules intermediate filaments (IF) compose the neuronal cytoskeleton. Neurofilaments are the most abundant neuronal cytosolic IF and consist of three different subunits: neurofilament light, medium, and heavy (NFL, NFM, NFH, respectively). Another major type of IF proteins expressed in adult neurons is α-internexin. While the roles of actin microfilaments and microtubules in neuronal development and function are rather well understood the functions of IF proteins

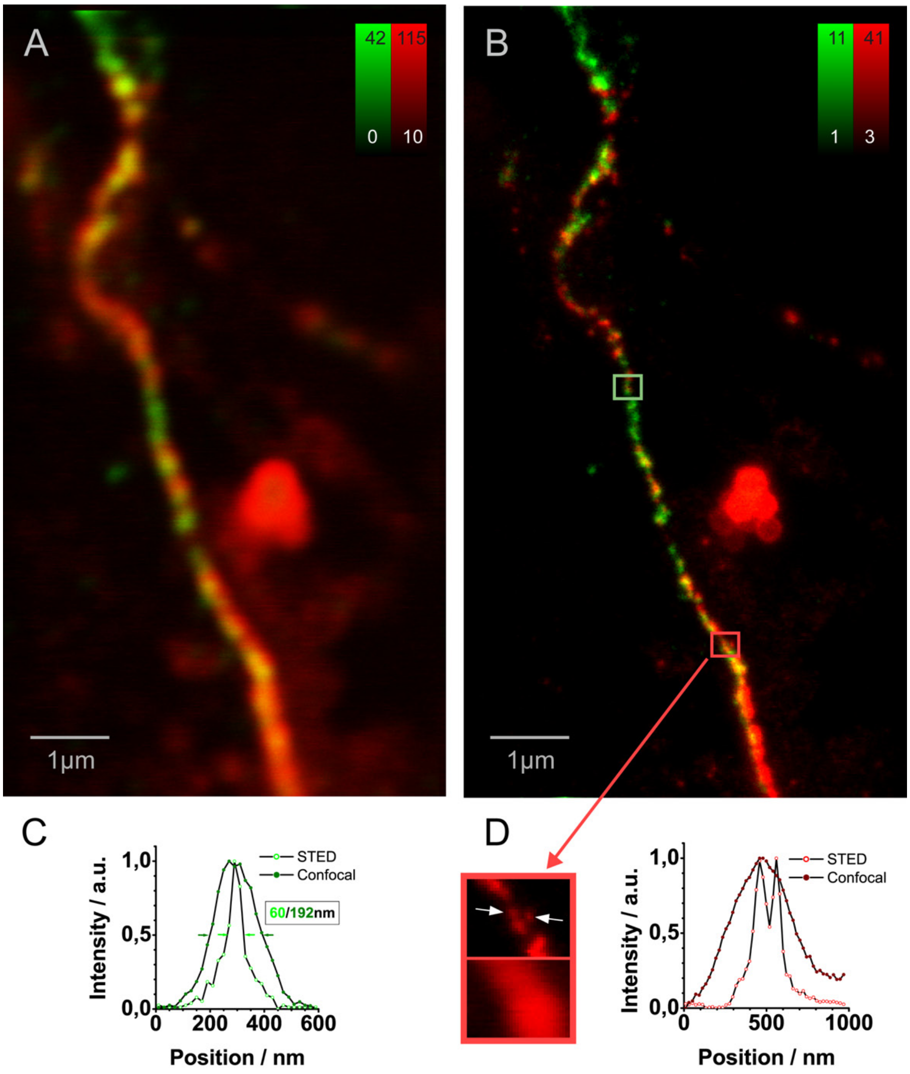

Figure 2.12: Light (green) and phosphorylated heavy (red) neurofilament subunits imaged with confocal (A) and dual-color STED (B) microscopy. The resolution gain is further visualized by the outtakes (C) and (D) which correspond to the green and red boxes in (B), respectively.

in neurons have remained, until recently, more elusive. [98] Generally, these proteins are of scientific interest because they are believed to play important roles in neurodegenerative diseases. [98, 99]

The STED image of figure 2.11 reveals three well-separated α-internexin strands that are conventionally unresolvable as can be seen in subfigure (D). The green color channel of the microscope is able to discern light subunits with FWHM of less than 40 nm (E). It turns out that NFL and α-internexin show different organizations within the axon.

In figure 2.12 again a notable resolution enhancement in contrast to confocal imaging is achieved by dual-color STED microscopy. The green NFL structures exhibit FWHM of approximately 60 nm with STED in comparison to 192 nm with confocal imaging. It needs to be pointed out that the measured FWHM is co-determined by the actual width of the filament bundles plus the detection complex (antibodies and dye molecules) and thus does not directly reflect the microscope's resolution. The actual resolution is expected to be even better (on the order of 35-40 nm as in figure 2.11). The graph in figure 2.12 (D) displays a line profile of the magnified outtake next to it. There, small domains of phosphorylated NFH are separated by STED which remain hidden in the confocal case.

Altogether, these measurements demonstrate that sub 40-nm resolution STED in biological samples is possible not only with one color channel but also in a dual-color arrangement.

2.3.3 3D reconstruction of high-resolution STED microscope images

The results presented so far have shown lateral resolution enhancement in multicolor STED microscopy. Resolution along the optical axis, however, has remained unaffected and equals the one achieved with conventional confocal microscopy. A logical step in the development of dual-color STED therefore is the improvement of spatial resolution along the axial dimension. Several principally different routes are feasible to this end, each with distinct advantages and drawbacks: An all-optical approach can be done by combining the lateral resolution increase of STED with axial resolution increase provided by 4Pi-microscopy. [57,100] This method is capable of achieving impressive results but suffers from a somewhat laborious alignment of the setup. Likewise, the technical demands of such a system are comparatively high. An alternative way that circumvents the 4Pi-configuration utilizes another phase plate for the STED beam to yield a PSF featuring a central zero-intensity zone along the optical axis. In combination with the classical, lateral STED donut this produces 126-fold smaller effective focal volumes than confocal microscopy. [46] Yet, this method necessitates splitting of the available STED power thus giving up a portion of stimulated emission depletion - and therefore also spatial resolution - in the lateral direction. The approach presented here tackles the issue of 3D-STED not from the optical but from the sample preparation side by providing thin samples (< 100 nm) obtained through sectioning of whole cells. [9] These samples are subsequently imaged with our dual-color STED setup to allow for 3D image reconstruction. In total, this yields multicolor STED microscopy with three-dimensional

---

[9] The novel sample sectioning procedure has been developed by Punge *et al.*. [68]

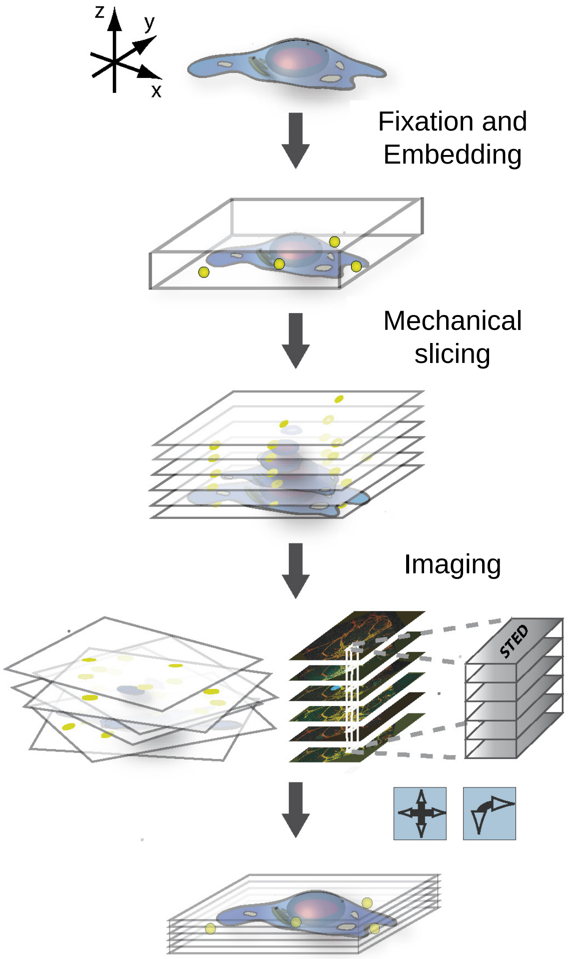

Figure 2.13: Schematic representation of the sectioning procedure for a 3D-reconstruction of STED images.

resolution of 35 × 35 × 80 nm^3 and eliminates the problem of out-of-focus fluorescence and photobleaching. [68]

Resin embedding and mechanical sectioning has been shown before using laser scanning confocal microscopy. [101] It is expected that the technique is even more advantageous for STED microscopy because additionally to providing sharpened images due to eliminated axial out-of-focus fluorescence it avoids prebleaching of axial out-of-focus areas due to high intensity STED light. Figure 2.13 illustrates the workflow of sample preparation. In a first step rat hippocampal neurons were prepared and immunostained as described. [102] Incubation is carried out incorporating two-color fluorescent silica beads (Micromod, Germany) [10] with a diameter of 300 nm as anchor points for posterior image alignment. After fixation the

---

[10] These beads initially were only green-fluorescent but could additionally be red-stained as described in the appendix.

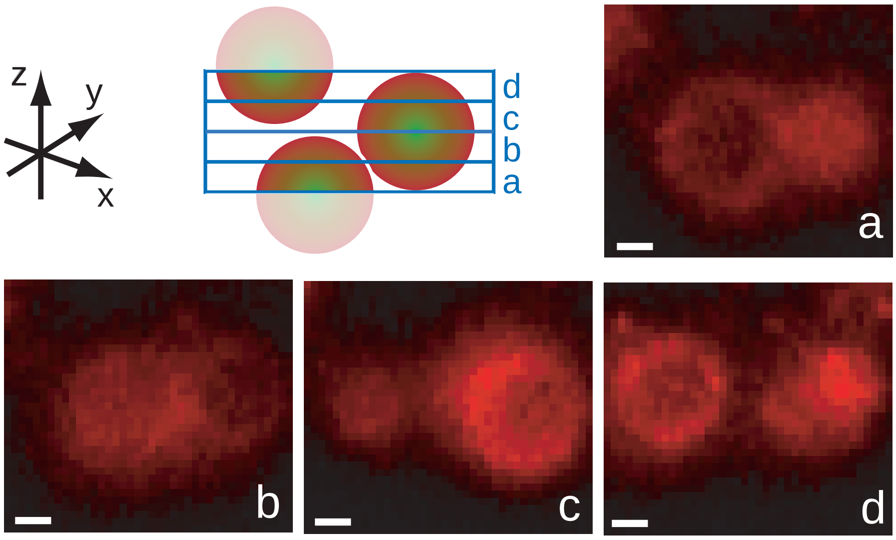

Figure 2.14: STED images of two 300 nm reference beads which are mechanically cut in thin sections (a-d) of 75 nm thickness each as illustrated in the schematic. The images were taken with the red channel of the dual-color STED microscope. Scale bar 100 nm.

cells are embedded in a polymer resin and then mechanically cut to 75-100 nm thin slices with an ultramicrotome (Leica, Germany). The individual slices can then be transferred onto a coverslip for imaging with confocal and STED microscopy. The resulting images are obtained from arbitrarily oriented slices. Proper 3D reconstruction is accomplished by computationally registering the dually labeled beads which have also been cut and can be identified in 2-4 consecutive sections. The process is depicted in the schematic of figure 2.14 where two reference beads are retrieved in sections (a) to (d). The according STED images were acquired with the red channel of the dual-color STED microscope. The ring-like structure stems from the fact that the two-color beads exhibit a core-shell structure with green dye in the center and a surface-staining with red dye.

The advantages of the sectioning technique become apparent when similar structures of highly three-dimensional neurons are imaged by STED microscopy using both sliced and conventional samples. In figure 2.15 the STED images of Atto 532-labeled SNAP-25 and Atto 633-labeled Synaptophysin are directly compared between these two cases. Obviously, individual protein clusters can unambiguously only be identified if sectioned samples are used. In bulk samples out-of-focus fluorescence caused by densely staining the proteins vitiates a clear discrimination of structural details.

With two novel methods at hand - a routinely applicable, laterally superresolving dual-color STED microscope plus a sectioning technique that produces extremely thin samples

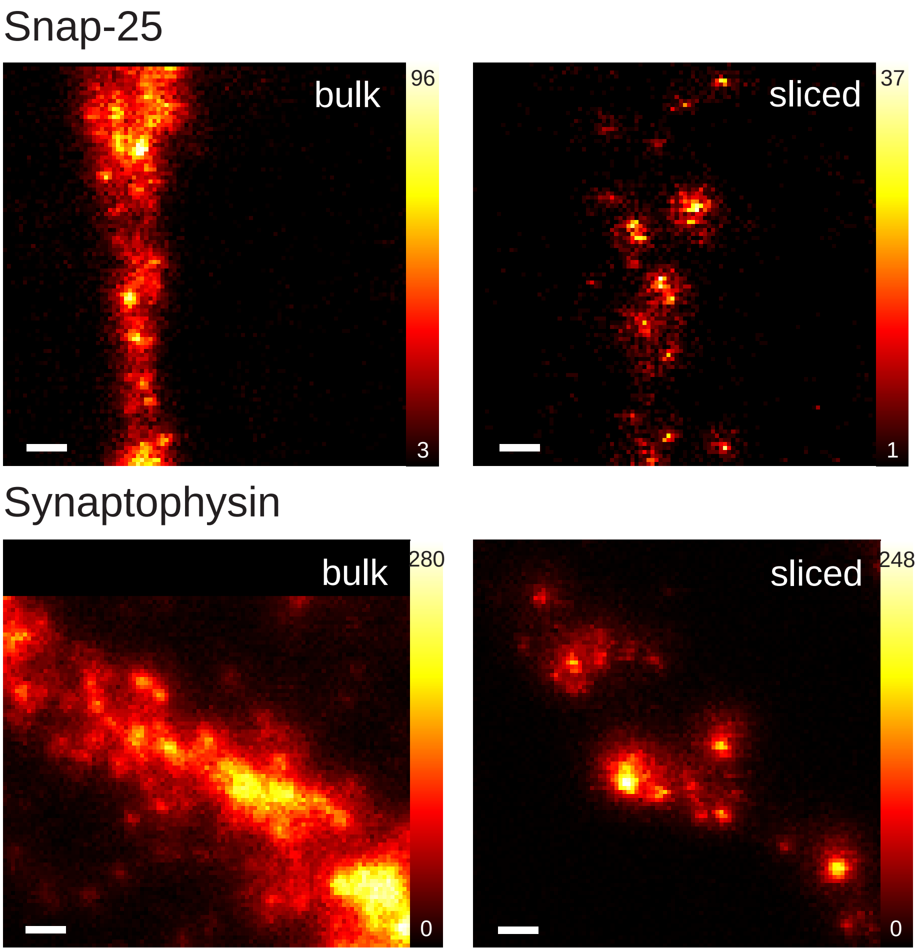

Figure 2.15: A comparison of STED imaging with sliced and conventional samples of SNAP-25 (labeled with Atto 532) and Synaptophysin (labeled with Atto 633). Distinct structural details are only observed with sectioned samples. The section thickness is 100 nm. Scale bar 200 nm.

eliminating out-of-focus fluorescence - the way is paved for three-dimensional reconstruction of dual-color STED images.

To this end large confocal overview pictures of each section are taken first (on a different setup) to serve as a map for retrieving the regions of interest. Localization of these positions in the STED microscope is then performed using a build-in wide-field microscope. In the following high-resolution STED images are acquired in both color channels for all consecutive sections (up to 15). For dual-color overlay and three-dimensional reconstruction the co-embedded beads are utilized as explained. The result of such a reconstruction is depicted in figure 2.16 where Syntaxin labeled with Atto 532 and Synaptophysin labeled with Atto 633 have been imaged. It constitutes the first three-dimensional representation of dual-color

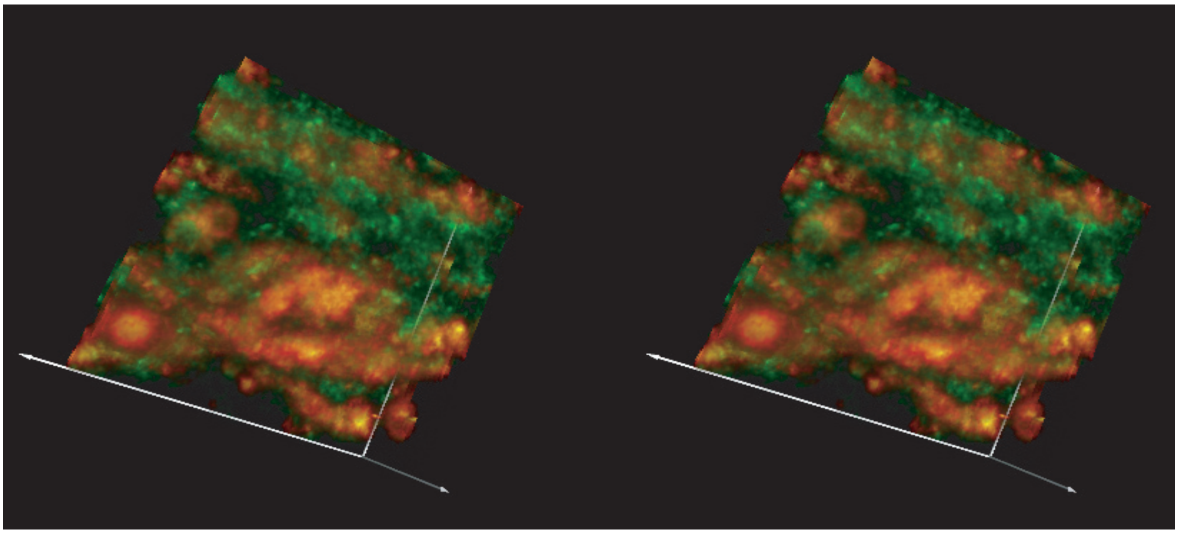

Figure 2.16: The stereoview image of a 3D-reconstruction consisting of several dual-color STED images (green: Syntaxin labeled with Atto 532, red: Synaptophysin labeled with Atto 633). The section thickness is 75 nm. The overall size of the image is 3 × 3 × 1.05 $\mu\mathrm{m}^3$.

STED images with a resolution of 35 × 35 × 80 nm^3 and opens up a novel way to study neuronal networks at ultrahigh resolution.

Despite the great potential of the described method it shall not remain unmentioned that it also compromises on certain aspects of modern microscopy. For instance, live-cell STED imaging [53] is not possible because the cells are cut and consequently killed during the sectioning procedure. Nevertheless, new insight in biological problems can be gained by employing 3D-reconstruction of multicolor STED images. To give a mere example, the spatial distribution of synaptic proteins SNAP-25, Syntaxin-1 and Synaptophysin has been studied by combining dual-color STED microscopy and sample sectioning. Unexpectedly, a colocalization analysis yielded that Syntaxin-1 and SNAP-25, although associated with synaptic vesicle fusion, are not restricted to the space near synaptic vesicle accumulations. [68]

2.3.4 Highlighting the early assembly of mouse retina photoreceptor ribbon synapses with STED microscopy

The results shown so far concentrated on developing the technique of dual-color STED microscopy in terms of resolution enhancement and 3D-capability. New biological insight has thereby been gained virtually “on the fly”. As a matter of course it is as well possible to employ the developed setup for detailed biological investigations. A great advantage in this respect is the system’s flexibility with two color channels because compared to a usual one-

color STED setup it widens the range of applicable dyes. This gives the biologists some freedom for the labeling procedure.
In this section it will be explained how the STED microscope has helped in elucidating the involvement of presynaptic proteins during early steps in the assembly of photoreceptor ribbon synapses in mouse retina. [67]

Neurotransmitter release from synaptic terminals takes places in a certain area of the presynaptic plasma membrane which is termed the *active zone*. [103] The mature *cytomatrix at the active zone* (CAZ, i. e., an electron-dense protein network) of conventional chemical synapses is composed of a set of proteins (e. g., Bassoon). [104] It is believed that the CAZ plays an important role in synaptogenesis. [105, 106] In the course of the formation of these synapses, i. e. before clustering of postsynaptic molecules, presynaptic CAZ proteins are recruited. [107, 108] During the assembly of the proteins precursor vesicles are assumed to be substantially involved. Precursor vesicles are $\sim$ 80 nm dense-core granulated vesicles which are known as *Piccolo-Bassoon transport vesicles* (PTVs). A whole variety of proteins can be found on PTVs including Syntaxin, SNAP-25 and Bassoon. PTVs are transported along axons to nascent synapses and fusion with the presynaptic plasma membrane to form the active zone. [109, 110]
The ribbon is a presynaptic organelle of the retinal photoreceptor synapse and is characteristically covered by synaptic vesicles. [111] Yet, its molecular composition has not been completely clarified. [112, 113] During synaptogenesis and illumination-dependent turnover processes at mature synaptic ribbons sphere-like structures have been discovered. [114, 115] So far, no statement could be made concerning the molecular composition of these spheres. STED microscopy could now demonstrate that these transport units are actually multiple and not single units. Further investigations using additional techniques reveal that they serve as transport units for CAZ proteins in the formation of photoreceptor ribbon synapses during synaptogenesis.

In figure 2.17 the Bassoon-stained transport units (labeled with Atto 633) are imaged with confocal microscopy and with the red channel of our dual-color STED setup. The STED image reveals that seemingly individual sphere-like transport units in the confocal image actually consist of multiple units. Analysis of the size distribution of the particles yields an average diameter of 129±20 nm (SD, n=12). These results are further confirmed by electron microscopy where on average a diameter of 129±36 nm (SD, n=143) has been observed. [67]
The precursor spheres in the above study by Regus-Leidig *et al.* [67] differ clearly from dense

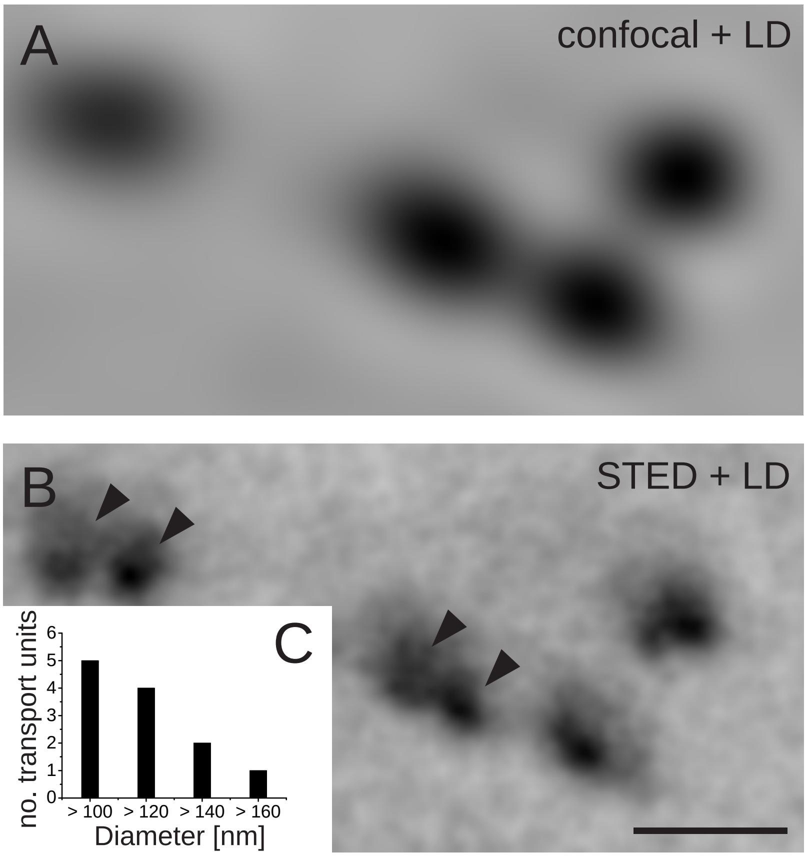

Figure 2.17: STED reveals that precursor spheres in presynaptic assembly of the photoreceptor ribbon contain multiple transport units. (A) Confocal and (B) STED image of Bassoon-labeled transport units stained with Atto 633 (both pictures are linearly deconvolved (LD)). (C): Histogram of the precursor spheres' size distribution as measured with STED (average diameter: 129±20 nm (SD, n=12)). Scale bar: 500 nm.

core vesicles (PTVs) in conventional synapse formation. While PTVs are dense core granulated vesicles [109] precursor spheres and photoreceptors are described as nonmembranous densities surrounded by synaptic vesicles.

Now that it has been found that the precursor spheres act as transport units for presynaptic cytomatrix proteins the question arises how many ribbon compartment proteins are carried by a sphere. Furthermore, the required number of precursor spheres for the formation of a ribbon synapse is of interest. STED microscopy in combination with *in vivo* imaging [52] could provide a means to clarify these questions in the future.

2.4 Summary

This chapter has set forth the development and construction of a dual-color STED setup with 30 nm focal plane resolution in both color channels. In order to achieve optimum performance great importance has been attached to the choice of the light sources. Flexible laser systems were chosen to simultaneously apply high STED powers and maintain full compatibility with standard organic dyes.

The optical setup consists of four superimposed beams - an excitation and STED beam for each color channel. PSF measurements prove the close to optimum alignment necessary for achieving superior resolution. STED depletion curves of red dyes confirm that the maximum STED power of the red channel by far exceeds the saturation intensities of the dyes. Thus, $\mathrm{I}_{\mathrm{STED}} >> \mathrm{I}_{\mathrm{SAT}}$ can be settled and according to equations (2.4) and (2.5) lateral superresolution far below the diffraction barrier is possible.

STED images of red- and green-fluorescent nanobeads reveal an actual resolution capacity of 33 nm and 31 nm, respectively, which corresponds to a further doubling of the red channel's resolution as compared to the first dual-color STED microscope built by Donnert *et al.*. [48] The resolution enhancement is shown to be transferable to complex neuronal systems enabling dual-color studies of synaptic proteins at a resolution of $\sim$ 35 nm.

In a next approach the quest for 3D-superresolution with STED has been tackled by combining the lateral resolution capability of the setup with a novel sectioning technique providing thinly sliced samples of 75-100 nm thickness. As a result extraordinary sharp STED images are obtained which can be sampled to accomplish the three-dimensional reconstruction of neuronal networks.

STED (along with other methods) has been utilized in an attempt to elucidate the role of precursor spheres in the early formation of photoreceptor ribbon synapses in mouse retina. The study reveals a sphere size of $\sim$ 130 nm and a composition of multiple units. The spheres act as transport units for CAZ proteins during synaptogenesis.

Altogether these results evidence the development of a flexible STED setup providing unprecedented resolution in two color channels. The systems could serve as a foundation for a series of further developments in multicolor STED: Desirable is a simplification of the laser system while simultaneously maintaining large parts of the wavelength flexibility. A setup based on a supercontinuum laser could meet these demands. [116] An all-optical approach to achieve 3D-superresolution with dual-color STED has been pursued by Schmidt *et al.* and bears the advantage of complete noninvasiveness. [57] The temporal evolution of dually stained biological species may be analyzed if the image acquisition time can be reduced.

Recent advances in this field should enable such efforts rather soon. [52]

The usage of a dye combination where one dye is characterized by a large Stokes-shift could finally enable a dual color excitation and one-color inhibition pattern. Such a system would necessitate only one STED laser and could therefore appreciably economize dual-color STED nanoscopy.

3 STED microscopy with fluorinated Rhodamine dyes

3.1 Motivation

In STED microscopy the choice of a suitable dye is crucial for achieving high resolution because high light intensities need to be applied to truly saturate the stimulated emission process. Even though a large variety of commercial dyes can be used for STED microscopy the chemical synthesis of novel dye classes offers an important starting point for optimization. The requirements for a good STED dye are manifold: Besides high photostability to tolerate the light intensities other properties such as high fluorescence quantum yield, large absorption cross section and low triplet formation are essential. Just as well, the dye has to provide for coupling to secondary antibodies against biological substances through introduction of appropriate functional groups. In this context high water solubility of the dye is desirable to mimic the native environment of biomolecules.

The synthetic chemistry group around Dr. V. Belov at the Max Planck Institute for Biophysical Chemistry in Göttingen [1] have developed a new class of fluorinated Rhodamine dyes for application in labeling and imaging techniques which fluoresce at wavelengths of ~ 520 nm. [117] Figure 3.1 displays the chemical structures of some synthesized derivatives and an exemplary absorption/fluorescence spectrum. Rhodamines are fluorescent dyes whose basic structure is that of Xanthene (also known as 10*H*-9-oxaanthracene or Dibenzo[*a*,*e*]pyran), a yellow organic heterocyclic compound. Compared to other fluorescent dyes such as Coumarine or Pyrene zwitterionic Rhodamine dyes have the advantage of being intrinsically hydrophilic. Their spectra are easily tunable by changing substituents at the Xanthene fragment and/or in the *o*-substituted benzoic acid residue. Sulfonation of the R^1-sites in figure 3.1 further increases water solubility, reduces aggregation and quenching of fluorescence in water/aq. buffers due to the generation of non-fluorescent dimers. [118] In this manner

---

[1] The group is integrated in the Department of NanoBiophotonics led by Prof. Dr. Stefan W. Hell.

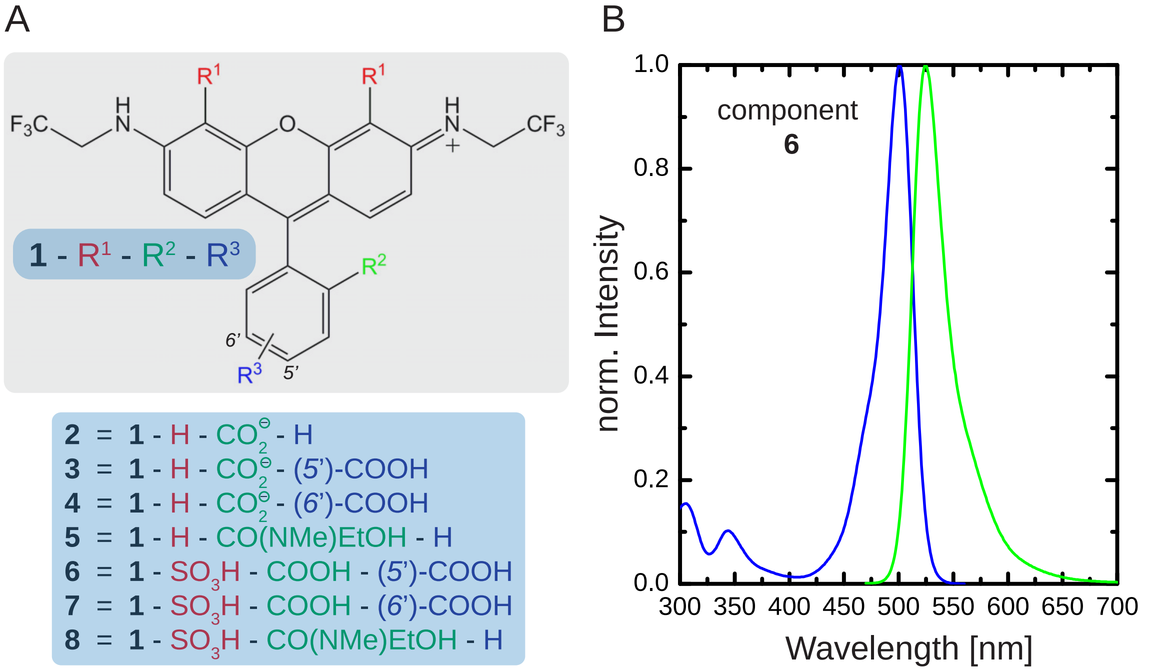

Figure 3.1: The chemical structures of some new fluorinated Rhodamines characterized for use in STED microscopy are depicted in (A) along with the UV-VIS and fluorescence spectra of component **6** (B). With an absorption maximum at 500 nm and fluorescence emission around 520 nm the spectra are exemplary for the new substance class.

the quantum yield of a free dye in solution and after coupling to a biological macromolecule is often increased, too. One hypothesis for this favourable behaviour is that sulfonation increases the distance to the conjugate and thus inhibits *fluorescence resonance energy transfer* (FRET). [119]

Due to a strong -*I*-effect fluorination of the xanthene fragment is likely to increase photostability. The inductive effect causes radical centers, which are known to be generated during bleaching reactions, to be destabilized thus reducing the photobleaching probability. [21,120]

3.2 Fluorescence depletion and STED imaging

In order to test the suitability of the new dyes for use in STED microscopy different measurements were performed with the green color channel of the optical setup described in section 2.2. Figure 3.2 displays the remaining fluorescence signal in case of a switched on STED

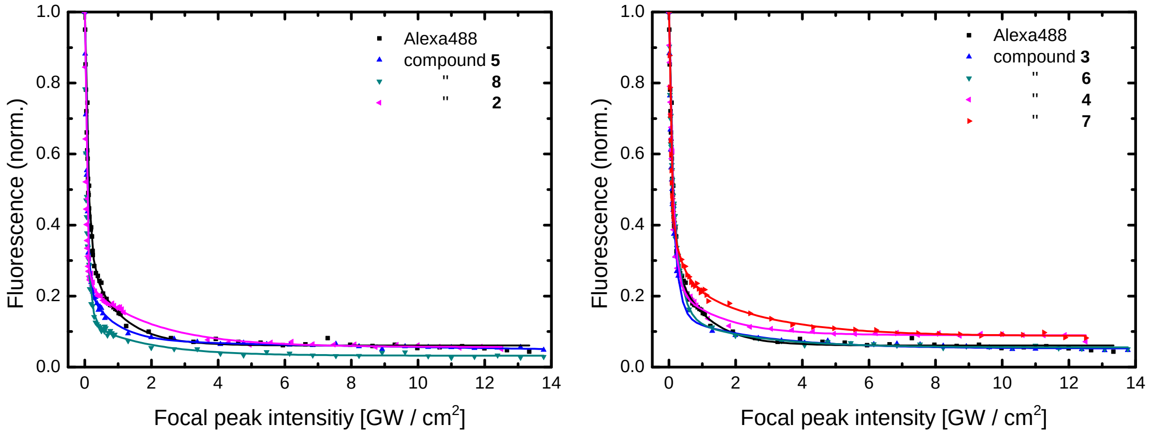

Figure 3.2: STED fluorescence depletion curves of several new fluorinated Rhodamines. The designation of the compounds follows the notation introduced in figure 3.1. For comparison the curves of commercially available compound Alexa 488 is given.

beam (λ = 593 nm) with increasing intensity. [2] A comparison between the depletion curves of the new dyes and that of commercial substance Alexa 488 (Molecular Probes, Eugene, USA) shows no significant difference which points out the custom-built dyes' high quality. Fluorescence depletion down to $\sim$ 4% of remaining signal is possible matching or improving results obtained from Alexa 488. Note the maximum light intensity of $\sim$ 13 GW/cm^2. Such enormous peak irradiations are possible through regeneratively amplifying ultrashort pulses (the pulse repetition rate is 76 MHz; compare section 2.2) and drive the transition between the dyes' electronic singlet states S_1 and S_0 far into saturation - a process required for STED to work. According to equation (2.4) image resolutions far below the diffraction limit of light can be expected with these dyes when considering the fact that $I_{\mathrm{STED}} >> I_{\mathrm{sat}}$ in the present examples.

In a next step compound **6** was converted to its NHS ester and coupled to the microtubule-associated protein Doublecortin (immunostained with anti-Doublecortin rabbit IgG) to prove the applicability of the new fluorinated Rhodamine dyes for superresolution STED imaging. The large frames in Figure 3.3 display the STED and confocal images of an axon within the structural environment shown in the smaller frame (bottom right). While already a look at the large STED image discloses a significant sharpening of the image compared to its confocal counterpart the small outtakes (bottom center) fasten this impression on numbers. The FWHM of the considered strand is reduced from approximately 155 nm in confocal mode to

---

[2] The samples were prepared from $\sim$ 10 μM dye solutions containing 1% PVA. 30-50 μL of the solution were then spin-coated ona a cover slip at 3000-4000 rpm.

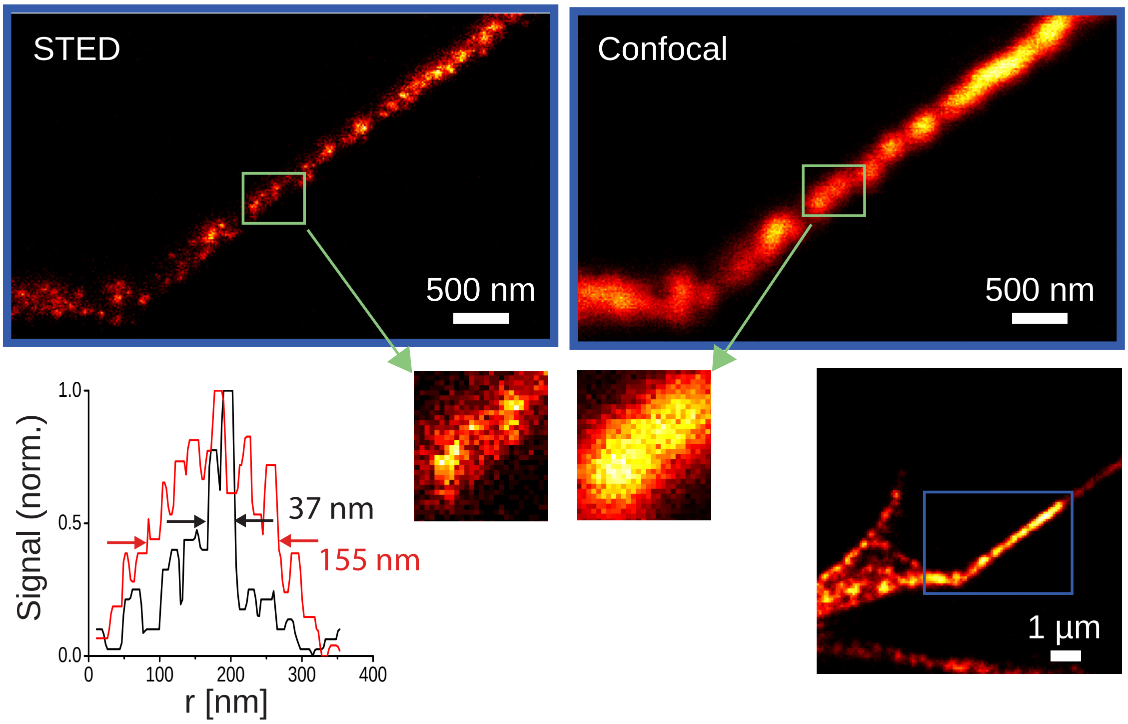

Figure 3.3: STED and confocal images of Doublecortin in neurons immunostained with anti-Doublecortin rabbit IgG bearing the compound **6**. Bottom right: Confocal overview image. The outtakes display the structure's Full-width-half-maximum (FWHM) within a fraction of the axon. In STED mode the FWHM is only approximately 37 nm whereas in confocal mode it is broadened to approximately 155 nm.

approximately 37 nm in STED mode. [3] Even though the signal ratio between confocal and STED image is on the order of 10:1 which means that many fluorophores are bleached during passage of the intense STED light the resulting signal-to-noise ratio in the STED image is still large enough to give clear contrast.

Another concrete example of the dye's pertinence to STED bioimaging is given in figure 3.4 where again pictures of the neuronal protein Doublecortin are shown. [4] In (A) the beginning of an axon strand is imaged with small bunches of proteins being nicely resolvable only in STED mode. Figure 3.4 (B) displays a combined STED and confocal picture of a different structural element. While the confocal part bears only a washy blur individual small dots are unraveled in the STED inset. Note the good signal-to-noise ratio also in the STED picture - a fact attributed to the quality of the new fluorinated Rhodamine dye.

---

[3] Excitation intensity (λ = 488 nm): 1.9 MW/cm^2; STED intensity (λ = 593 nm): 1.6 GW/cm^2.

[4] Excitation intensity (λ = 488 nm): 1.9 MW/cm^2; STED intensity (λ = 593 nm): 1.6 GW/cm^2.

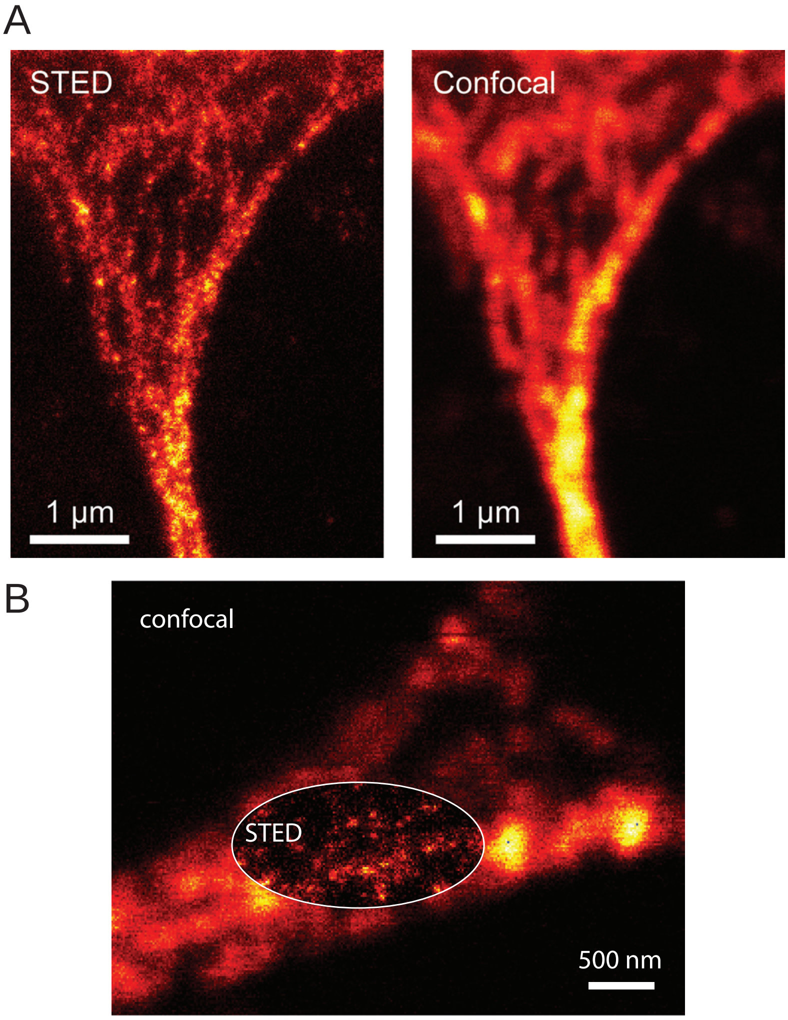

Figure 3.4: (A) and (B) display STED and confocal images of Doublecortin in neurons labeled with compound **6** (secondary antibody: anti-rabbit IgG). The resolution of the STED image clearly outmatches the confocal resolution with the dye tolerating high STED intensities as can be seen by eye from the good signal-to-noise ratio.

3.3 Summary

STED microscopy is a powerful method for optical imaging beyond the diffraction limit. Yet, its full performance can only be unleashed if high quality fluorescent dyes with properties such as high photostability, high fluorescence quantum yield and/or low triplet formation are utilized. A new class of fluorinated rhodamine dyes has been invented by Belov *et al.* that bands together many of these favourable properties. The dyes are found to be stable under exposition to intense STED light and perform well in fluorescence depletion experiments using the STED setup described in section 2.2. Conjugation of one dye derivative to the neuronal protein Doublecortin enables the recording of high quality STED images with resolution below 40 nm.

4 Nanolithography using Stimulated Emission Depletion

In this chapter it will be set out how the STED concept can be adapted to optical writing on the nanoscale. A brief review of the research field of lithography is followed by the presentation of a viable concept for nanolithography employing STED induced photobleaching suppression. Next, experimental evidence of this phenomenon is given and an appropriate photophysical model is derived to further corroborate the results. It will then be shown that subdiffraction optical patterning of easily fabricable samples is possible if a spatially altered STED beam is utilized.

4.1 Optical writing on the nanoscale - why and how?

The preceding chapter of this thesis and numerous examples from the recent literature prove that STED microscopy has established itself as a valuable technique to accomplish optical imaging with subdiffraction resolution in biological and material science. [121–123] With the expertise gained from these experiments it would be an exciting and challenging task to eventually 'go the other way around' and to use STED not only for structural readout but for the process of optical nanopatterning, too. The prospects of such a technique are tremendous: Ongoing industrial need for miniaturization and integration of sub-micron structured material surfaces have truly boosted the field of lithography in recent years and also call for alternative approaches.

A case distinction can be made between conventional and unconventional lithography. [124] The former encompasses highly developed and widely used techniques such as projection lithography and scanning beam (or maskless) lithography whereas the latter comprises new types of fabrication that circumvent limitations of conventional methods. Soft lithography [125–127] and scanning probe lithography [128–131] are just two examples of unconventional lithographic techniques.

Photolithography [132] can be ranked among projection lithography and is thus classified as a conventional method. The advent of new UV-lasers with wavelengths down to 157 nm and suitable optics have enabled photolithography to produce feature sizes as small as 50 nm. [133] With scanning beam lithography using electron beams or focused ion beams it is even possible to deposit or remove material with sub-10 nm resolution. [134] However, each of these techniques has distinct limitations which constrain extensive applicability and further development. Problems encountered in electron beam lithography, for instance, include the generation of high-power secondary electrons and strong scattering within the sample. Moreover, the patterning process is comparatively slow. Photolithography, on the other hand, overcomes the problem of slow pattering through parallelization but is fundamentally limited by diffraction and requires complicated sample preparation. The utilization of shorter wavelengths (X-rays, e. g.) further decreases pattern size but comes at the expense of severely increased technical - and hence also financial - costs. [135] These drawbacks in conjunction with significant industrial demand for inexpensive ways to produce nanopatterned surfaces indicate the need for novel, innovative approaches to (photo)lithography in the nanometer resolution range.

Furthermore, it can be distinguished between lithographic techniques working in the far-field and those operating in the near-field. Near-field methods have been presented that break the diffraction limit, for instance, by illuminating a sample with wavelength λ_0 through a very small pinhole with radius r_0 where $r_0/\lambda_0 << 1$. [136] Yet, operating with evanescent spatial frequencies in the optical near-field requires very high precision of sample positioning because the waves decay exponentially with distance from the interface at which they are formed. [137] Such handicaps are usually not present for far-field techniques where the distance between objective and sample is comparatively large. Here, matters can further be simplified by the utilization of adequate laser sources providing cost-efficient and stable illumination. As mentioned above, the main obstacle in applying far-field techniques for lithography has so far been the diffraction barrier. [6] Now that various methods exist that are capable of breaking the diffraction limit in microscopy it is a straightforward idea to tackle this limit in optical writing, too.

Recently, three approaches have been published that have accomplished optical writing with subdiffraction resolution down to λ/20 with visible light. [62–64] They are circumstantially discussed in section 1.3. These approaches have in common that they avail themselves of standard photolithographic features. While two of these methods work with partially inhibited polymerizations to write patterns, the third method uses photochromic molecules to render a film on top of a photoresist opaque or transparent. Each of the concepts utilizes a depletion scheme inspired by STED. While doubtlessly those results are impressive and mark a significant simplification of the required optics as compared to conventional lithography, they might have the disadvantage of a somewhat elaborate sample preparation. In addition to that, the processes involved in depletion are rather complex and appear to be not yet fully understood from a photophysical/-chemical point of view. Preferably would therefore be optical lithography with simplified sample preparation and well-understood/-controllable photophysics. In the following sections such an 'unconventional' photolithography approach will be presented and thoroughly discussed.

4.2 Results

4.2.1 A concept for Nanolithography using STED

The novel approach to nanopatterning is based on photobleaching thin lines into layers of fixed fluorophores. The photobleached areas are subjected to the diffraction limit of $\Delta r = \lambda/2\mathrm{NA}$, where λ is the wavelength and NA denotes the numerical aperture of the optical system. Yet, it appears to be reasonable to argue that smaller features will be realized if the laser spot's potential to photobleach is somehow inhibited in the outer regions of the focus. In order to further illustrate this idea, figure 4.1 (A) schematically depicts the electronic energy levels of a conventional organic dye. In this scheme three singlet states S_0, S_1 and S_n are considered. Fluorescence emission from S_1 to S_0 usually follows $\mathrm{S}_0 \rightarrow \mathrm{S}_1$ excitation. However, due to its higher energy level additional reaction pathways are passable from S_1 which may possibly lead to photodestruction of the fluorophore. An important pathway of that type is the transition from S_1 to S_n which is launched at high laser intensities. [138] If now a STED laser is switched on whose wavelength is adjusted such that it efficiently drives the $\mathrm{S}_1 \rightarrow \mathrm{S}_0$ transition two effects are prominent: On the one hand, the fluorescent state S_1 is depleted (as exploited in STED imaging) but additionally molecules are prevented from running the photodestructive $\mathrm{S}_1 \rightarrow \mathrm{S}_n$ pathway. The general bleaching suppression capability of STED in this scheme is displayed in figure 4.1 (B). Here, lines are bleached by a 76 MHz - pulsed 488 nm laser in a layer of the organic dye KK114 [139] ($\lambda_{\mathrm{abs}} \approx$ 640 nm, $\lambda_{\mathrm{em}} \approx$ 660 nm) on a custom-built STED microscope. The layer has been prepared by spin-coating an aqueous solution of the dye onto a microscope cover glass which is then directly mounted without an additional medium. Such layers seem to exhibit sufficient fixation due

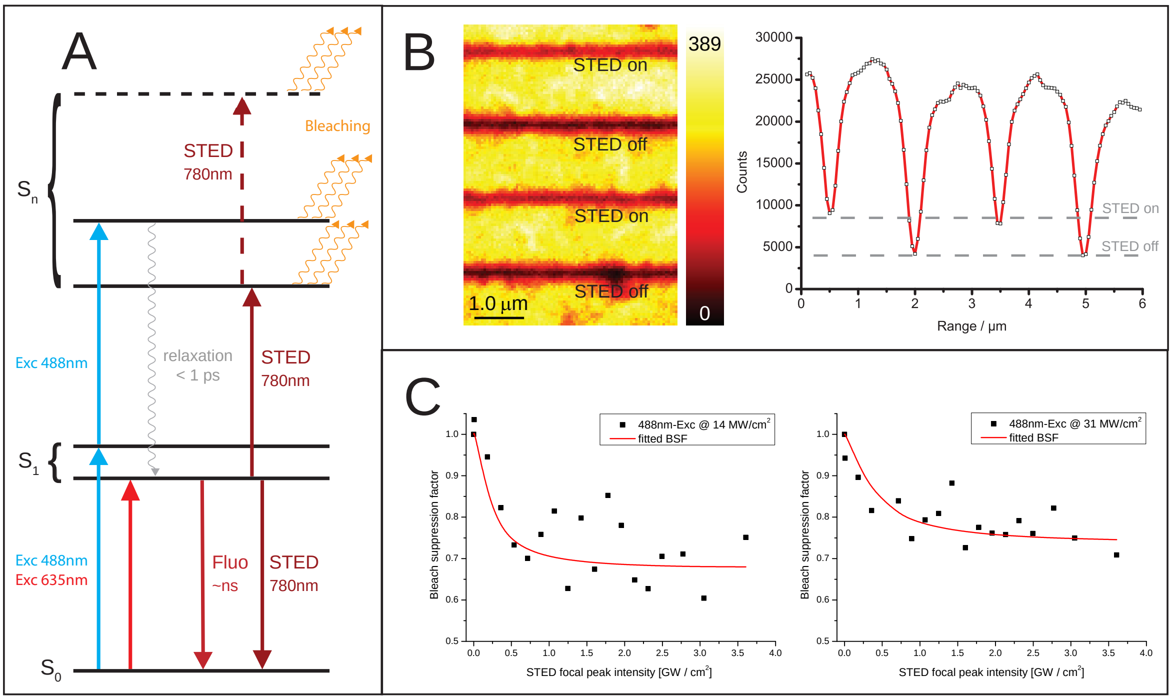

Figure 4.1: A: Three-level singlet system of a conventional dye and possible reaction pathways. B: Bleached lines in a dye film with the STED beam alternately switched off and on along the y-direction. The graph displays a y-line profile through the image with counts summed up along the x-axis. Clearly, less molecules are photobleached if the STED beam is switched on. C: BSF as a function of STED intensity for two different 488 nm bleaching intensities. The points represent measured data, the red lines correspond to fitting results.

to adsorption since no washing-out of the bleached lines was observed. The dye KK114 was chosen because it features some beneficial properties for our purposes. Its rather low triplet state population avoids very efficient photobleaching within the triplet system. [79] Furthermore, excitation at 488 nm, i. e., a wavelength significantly blue-shifted with respect to the absorption maximum, induces very pronounced photobleaching via S_n. [21, 140] Read-out of the written structures was performed with a red laser (λ = 635 nm) at very low intensities on the order of 500 nW to keep this process quasi-nonbleaching. In figure 4.1 (B) the first and third lines were written with a 488 nm laser superimposed by an ordinary STED beam (λ = 780 nm) at a pixel dwell time of 10 ms. In lines two and four, on the other hand, the STED laser is kept off. When comparing the number of counts in these lines, it is noticeable that significantly higher signals are recorded in case of a switched on STED beam as can be seen in the graph besides the image. As the level of remaining fluorescence is a measure of the extent of photobleaching, we may directly infer that the STED beam acts as a suppressor of molecular photobleaching.

For a more quantitative description of the suppression effect we implemented a measurement

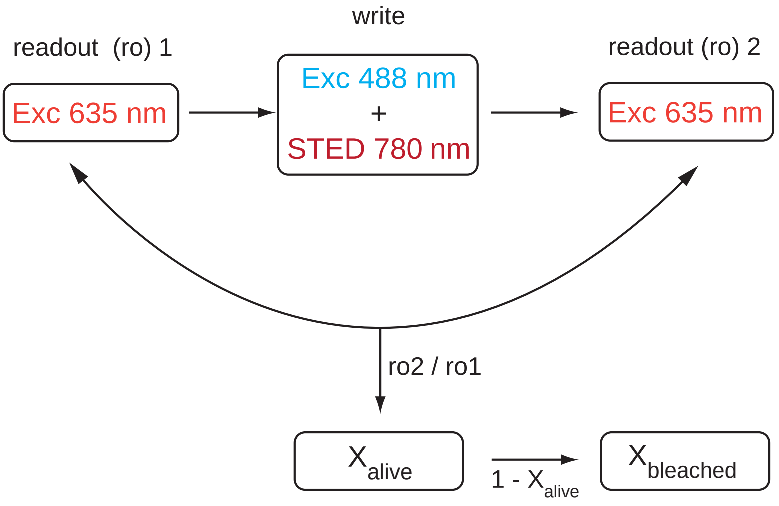

Figure 4.2: Illustration of the data analysis workflow for a quantitative description of the bleaching suppression effect.

scheme that should give a maximum of reliability and independence of other effects. The workflow of this analysis is shown in figure 4.2. At first, the quasi-nonbleaching low power 635 nm read-out laser scans a 10×10 μm sample area with a short pixel dwell time (0.5 ms) and large step size (1 μm) to obtain the initial fluorescence signal. In a second scan the same positions are intensely illuminated by the 488 nm bleaching laser for 5 ms to produce single isolated photobleached spots, whose remaining signal level is recorded by a third scan with the 635 nm read-out light. The STED beam is switched on every other line. Afterwards, the quotient of the two read-out measurements is calculated to yield the fraction $\mathrm{X}_{\mathrm{alive}}$ of unbleached fluorophores. Consequently, the fraction of bleached molecules is $\mathrm{X}_{\mathrm{bleached}}$ = 1 - $\mathrm{X}_{\mathrm{alive}}$. The photobleaching suppression effect can now be quantified by comparing the fractions $\mathrm{X}_{\mathrm{bleached}}$ and $\mathrm{X}_{\mathrm{bleached}}$(STED) without and with the STED light and calculating the bleach suppression factor (BSF).

$$\mathrm{BSF} = \frac{\mathrm{X}_{\mathrm{bleached}}\,(\mathrm{STED})}{\mathrm{X}_{\mathrm{bleached}}} = \frac{1 - \mathrm{X}_{\mathrm{alive}}\,(\mathrm{STED})}{1 - \mathrm{X}_{\mathrm{alive}}} \tag{4.1}$$

Values of the BSF smaller than 1 indicate suppression of photobleaching and larger levels of remaining fluorescence signal. To account for local inhomogeneities of the dye film the measurement was repeated several times on different positions within the sample. The resulting value of the BSF factor should therefore give a robust average as plotted in figure 4.1 (C) for two different laser intensities of the 488 nm bleaching light and increasing STED light intensity. We observe increasing suppression of photobleaching if the STED intensity is augmented. At approximately 70% a saturation level is reached which means that under current experimental conditions photobleaching can be suppressed by up to 30%.

In order to rule out that effects other than stimulated emission depletion may be responsible for the bleaching suppression the following experiment was carried out: For seven different bleaching and STED intensities [1] lines were written in a layer of dye. Thereby the STED beam was alternately switched on and off. Next, the 488 nm - bleaching power (measured in the back aperture of the objective lens) necessary to bleach approximately 50% of the molecules was evaluated and subsequently plotted versus the applied STED power (figure 4.3). While graph (A) was obtained with an optimized temporal delay between pulses of excitation- and STED-beam, this timing was detuned in the graph of figure 4.3 (B). Obviously more excitation power is needed in case of an optimized STED pulse timing which in turn means that indeed stimulated emission depletion is responsible for the reduction of photobleaching induced by the excitation beam. Figure 4.3 (C) shows a relative depiction of the aboves. Here, the quotient of the cases 'STED on' (optimized delay) and 'STED off' (detuned delay) is calculated. The graph nicely reveals that the effect of bleaching suppression is only present in the case of an optimized STED delay. This may serve as another argument that indeed stimulated emission is responsible for the observed bleaching suppression. Another interesting observation from figure 4.3 is that bleaching suppression passes through a maximum if the STED power is increased. An explanation of this behaviour could be that beyond a crucial STED power STED-induced bleaching becomes dominant and outweighs the suppression effect. This effect is much less pronounced in the measurements underlying figure 4.1 (C) which probably is a matter of writing step size. While the step size is large (1 μm) in figure 4.1 (C) to avoid overlap of PSFs on written patterns along the axis, the step size is made small in figure 4.3 to achieve linewriting. Hence the total illumination of a written spot is significantly larger in the latter case resulting in amplified STED bleaching.

4.2.2 Theoretical description

To further corroborate the experimental findings shown in figures 4.1 (B) and (C) we theoretically modeled the bleaching suppression. To this end, the BSF is defined as a function of three parameters: The bleaching intensity $\mathrm{I}_{\mathrm{exc}}$ at λ = 488 nm, the STED intensity $\mathrm{I}_{\mathrm{STED}}$ at

---

[1] Irradiancies: 488 nm bleaching laser 1.0 - 35.2 MW/cm^2, 780 nm STED laser 0 - 1.3 GW/cm^2

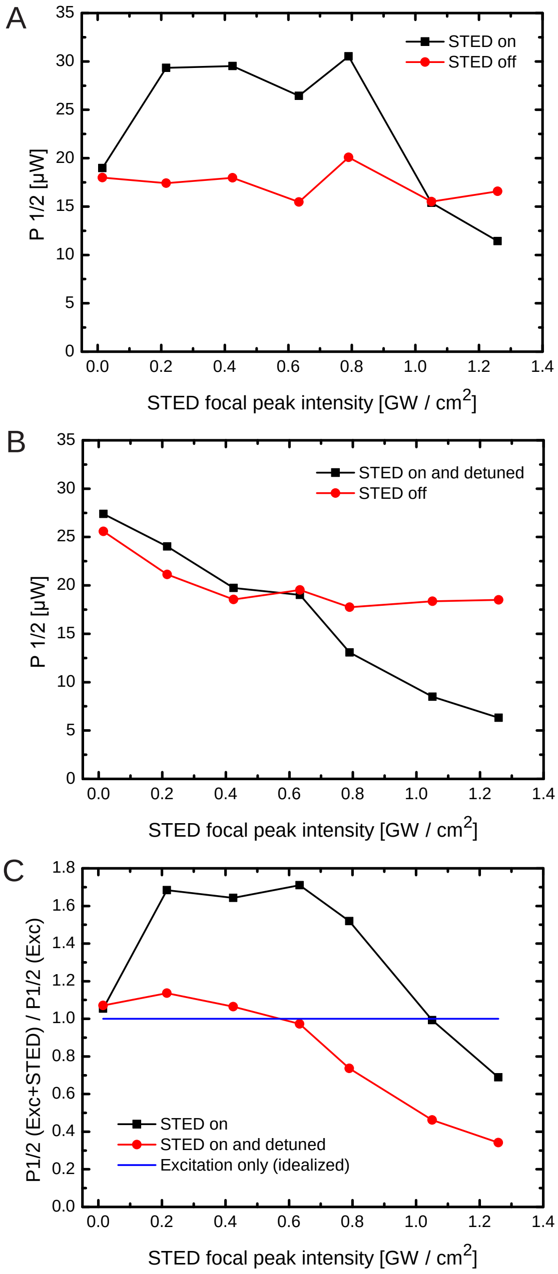

Figure 4.3: The excitation power needed to bleach approx. 50% of the molecules as a function of STED power. (A): STED-delay optimized for maximal fluorescence suppression; (B): STED and excitation temporally detuned; (C): Relative representation [P1/2(Exc+STED) / P1/2(Exc)] of the above graphs. The blue line corresponds to the situation of using the excitation beam only (idealized). In this depiction it is cognoscible that bleaching suppression is only effective if the excitation and STED beams are temporally overlapped.

λ = 780 nm and the pixel dwell time $\mathrm{t_{dw}}$.

$$f : \mathrm{I_{exc}}, \mathrm{I_{STED}}, \mathrm{t_{dw}} \longmapsto \mathrm{BSF} \tag{4.2}$$

Our calculations are based on the electronic level system of figure 4.1 (A) with electronic singlet states $\mathrm{S_0}$ and $\mathrm{S_1}$ and their interconversion rates $\mathrm{k_{01}}$ ($\mathrm{S_0} \rightarrow \mathrm{S_1}$) and $\mathrm{k_{10}}$ ($\mathrm{S_1} \rightarrow \mathrm{S_0}$) and an effective photobleaching rate $\mathrm{k_{bl}}$ from $\mathrm{S_1}$. The fraction of bleached molecules $\mathrm{X_{bleached}} = 1 - \mathrm{X_{alive}}$ can be calculated by solving the following rate equation system at any time of the pulse train of excitation and STED light [21]:

$$\frac{\mathrm{d}\,[S_0]}{\mathrm{d}t} = -k_{01} \cdot [S_0] + k_{10} \cdot [S_1] \tag{4.3a}$$

$$\frac{\mathrm{d}\,[S_1]}{\mathrm{d}t} = -k_{1,\mathrm{bl}} \cdot [S_1] - k_{10} \cdot [S_1] + k_{01} \cdot [S_0] \tag{4.3b}$$

$$\frac{\mathrm{d}\,[\mathrm{X_{bleached}}]}{\mathrm{d}t} = k_{1,\mathrm{bl}} \cdot [S_1] \tag{4.3c}$$

In these equations $\mathrm{k_{01}}$ is the rate constant of excitation from $\mathrm{S_0}$ to $\mathrm{S_1}$ (assumedly no excitation through the STED beam occurs) and $\mathrm{k_{10}}$ is the rate constant of the corresponding de-excitation (which is solely performed by the STED beam or by fluorescence). $\mathrm{S_0}$ and $\mathrm{S_1}$ are the relative populations of the electronic singlet states. The rate constants

$$k_{01}\,(t) = \sigma_{\mathrm{exc}} \cdot \gamma_{\mathrm{exc}} \cdot I_{\mathrm{exc}}\,(t) \tag{4.4}$$

and

$$k_{10}\,(t) = 1/\tau_{\mathrm{fl}} + \sigma_{\mathrm{STED}} \cdot \gamma_{\mathrm{STED}} \cdot I_{\mathrm{STED}}\,(t) \tag{4.5}$$

are given by the effective cross sections of absorbing excitation light $\sigma_{\mathrm{exc}} \cdot \gamma_{\mathrm{exc}}$ and of stimulated emission by the STED light $\sigma_{\mathrm{STED}} \cdot \gamma_{\mathrm{STED}}$. Here, σ_{xx} denotes the photon cross section for the considered process and $\gamma_{\mathrm{xx}} = \lambda_{\mathrm{xx}}/hc$ stands for the reciprocal photon energy at a certain wavelength λ_{xx}. Here, h and c are Planck's constant and the velocity of light, respectively. The pulsed laser intensities $\mathrm{I_{exc}}$ and $\mathrm{I_{STED}}$ are dependent on time t and τ_{fl} is the fluorescence lifetime of the dye. Population of the triplet state may be neglected because for dye KK114 a maximum population of less than 3% is generated through excitation by

488 nm light. [2] Photobleaching is accounted for via the following rate constant:

$$\begin{aligned} k_{\mathrm{bl}} = {} & \sigma_{\mathrm{1n,bl}} \cdot \gamma_{\mathrm{exc}} \cdot I_{\mathrm{exc}}\left(t\right) \\ & + \sigma^*_{\mathrm{1n,bl}} \cdot \gamma_{\mathrm{STED}} \cdot I_{\mathrm{STED}}\left(t\right) \\ & + \delta^*_{\mathrm{1n,bl}} \cdot \gamma^2_{\mathrm{STED}} \cdot I_{\mathrm{STED}}\left(t\right)^2 \end{aligned} \tag{4.6}$$

Here, photobleaching occurs from higher excited electronic states S_n via additional absorption of photons in the S_1 state. Three different bleaching pathways are incorporated: One-photon absorption of excitation light with bleaching cross section $\sigma_{\mathrm{1n,bl}}$, one-photon absorption of STED light with bleaching cross section $\sigma^*_{\mathrm{1n,bl}}$ and two-photon absorption of STED light with bleaching cross section $\delta^*_{\mathrm{1n,bl}}$. Most notably, equation (4.6) features the possibility of photobleaching by the STED beam as a competitive process to stimulated emission. [65] Assuming gaussian pulses with a repetition rate of 76 MHz and setting all relevant characteristics of the employed experimental setup [3], an algorithm has been developed that solves equations (4.3) numerically and thereby performs a least-squares fit to approximate the unknown bleaching cross sections $\sigma_{\mathrm{1n,bl}}$, $\sigma^*_{\mathrm{1n,bl}}$ and $\delta^*_{\mathrm{1n,bl}}$ using experimental data from figure 4.1 (C). Further, $\sigma_{\mathrm{exc}}\left(488\mathrm{nm}\right) = 1.57 \cdot 10^{-18}\mathrm{cm}^2$, $\sigma_{\mathrm{STED}} = 6.75 \cdot 10^{-16}\mathrm{cm}^2$ and τ_{fl} = 2.9 ns were assessed from control experiments of the absorption and emission spectrum and from fluorescence lifetime measurements by time-correlated single-photon counting. As can be seen by the red lines in the graph of figure 4.1 (C) the model describes experimental data rather well and provides good estimates for the bleaching cross sections:

$$\sigma_{\mathrm{1n,bl}} \approx 4.0 \cdot 10^{-19}\mathrm{cm}^2 \tag{4.7a}$$

$$\sigma^*_{\mathrm{1n,bl}} \approx 1.9 \cdot 10^{-20}\mathrm{cm}^2 \tag{4.7b}$$

$$\delta^*_{\mathrm{1n,bl}} \approx 4.0 \cdot 10^{-50}\mathrm{cm}^4\mathrm{s} \tag{4.7c}$$

The theoretical model together with the determined effective photobleaching cross sections enables mapping the desired behavior of the BSF as a function of $\mathrm{I}_{\mathrm{exc}}$ and $\mathrm{I}_{\mathrm{STED}}$ as depicted in figure 4.4. For comparison, the dwell time t_{dw} is adjusted such that each data point corresponds to a situation where 50% of the molecules are bleached for $\mathrm{I}_{\mathrm{STED}}$ = 0. The BSF appears to reach its lowest values at comparatively high excitation and STED intensities. Thus, the suppression effect is maximized if strong bleaching by the excitation beam is counteracted by strong stimulated emission depletion over a comparatively short time. The

---

[2] The according calculation is described in section 4.3.

[3] These parameters are subsumed in table 4.1 of the experimental section.

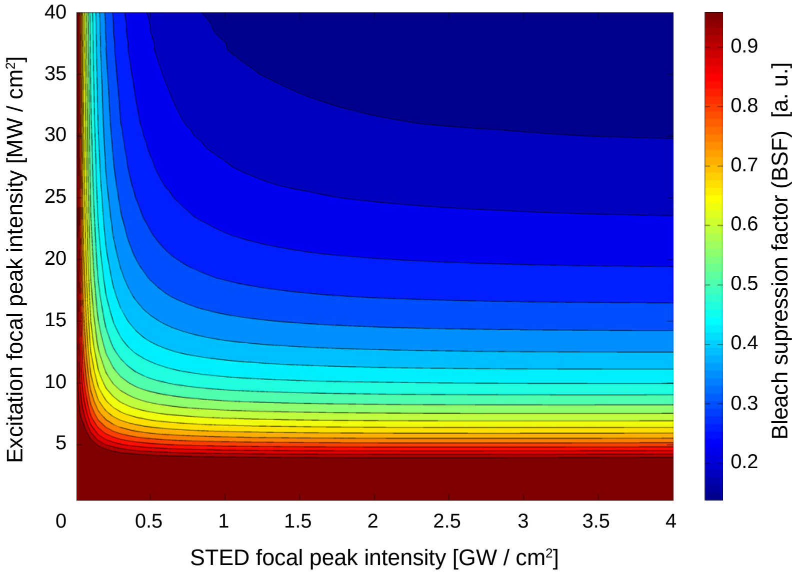

Figure 4.4: Mapping of the BSF as a function of excitation- and STED-power using the estimated bleaching cross sections in equations (4.7). The dwell time is made variable to bleach exactly 50% of the molecules for $I_{\mathrm{STED}} = 0$.

pixel dwell time for large values of I_{exc} and I_{STED} is on the order of $\approx$ 0.5 ms. Note that the contour lines do not decay monotonically which is a consequence of the introduction of multi-step bleaching cross section $\delta^{*}_{1n,\mathrm{bl}}$ which will eventually dominate at very large STED powers. At fixed excitation power and varying STED intensity the BSF will therefore run through a distinct minimum which marks the STED power for optimized photobleaching suppression.

4.2.3 STED nanolithography

Theory

So far the discussion has concentrated on proving and explaining the effect of photobleaching suppression using STED. It could be shown that in a simple dye layer strong photobleaching is induced by exciting the red-emitting fluorophore KK114 with a pulsed high-intensity laser at a wavelength of 488 nm (focal peak intensities on the order of several MW/cm^2). By superimposing a pulsed STED laser at a wavelength of 780 nm (focal peak intensities on the order of a few GW/cm^2) this photobleaching can effectively be suppressed. In a next step it shall be worked out how this phenomenon can be exploited for subdiffraction optical writing. Therefore, the spatial appearance of the STED PSF needs to be altered such that a tiny zero-

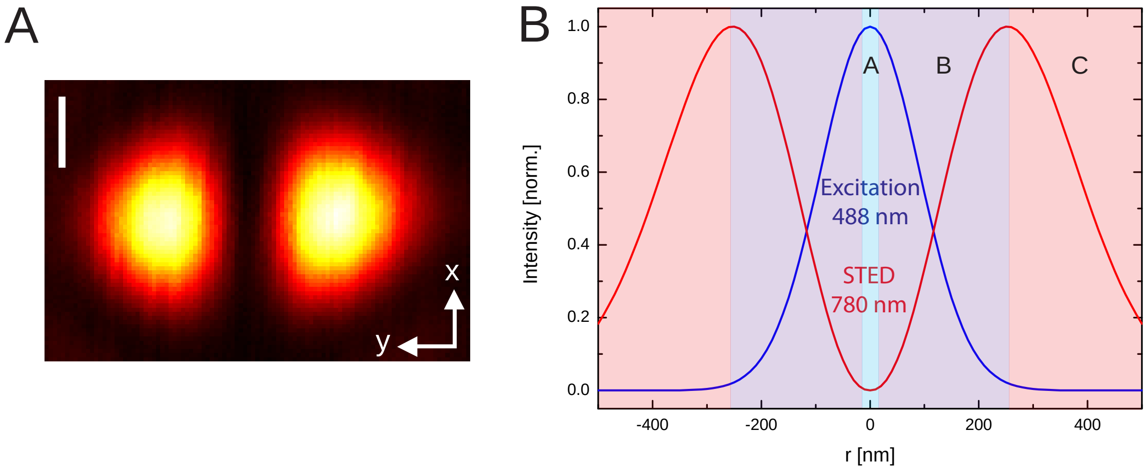

Figure 4.5: (A) PSF of the 780 nm STED beam after π-shift of the wavefront (scale bar 200 nm). The according y-line profile featuring a zero intensity position is given in (B) along with the gaussian line profile of the blue excitation/bleaching laser. In zone A bleaching occurs only through the exciting beam, whereas in zone B the interplay between excitation, bleaching and bleaching suppression by STED determines the degree of bleaching. In zone C only the STED beam contributes to (weak) bleaching.

intensity zone is generated. Figure 4.5 depicts such a configuration realized by inserting a phase mask into the STED beam π-shifting a semicircular area of the wavefront. Within this central zone only the blue bleaching laser is effective (zone A in figure 4.5 (B)) whereas in all other parts of the beam bleaching suppression by stimulated emission depletion prevails. As a consequence, a pattern will be imprinted whose size nonlinearly depends on the STED intensity (zone B in figure 4.5 (B)). In fact, if the STED intensity is further increased, even subdiffraction-sized patterns should be realizable.

Solving the system of rate equations (4.3) on a spatial grid $(\mathrm{I}_{\mathrm{exc}}(r,t), \mathrm{I}_{\mathrm{STED}}(r,t))$ for the setup consisting of superimposed excitation beam and phase-shaped STED beam attests that indeed the FWHM of a bleached spot can significantly be reduced. Figures 4.6 (A) and (B) display the results of the retrieved model calculated for experimental conditions that have been used to record data for figure 4.1 (C). For these conditions ($\mathrm{I}_{\mathrm{exc}}$ = 14 and 31 MW/cm^2, $\mathrm{I}_{\mathrm{STED}}$ = 1.9 GW/cm^2) [4] merely a moderate decrease of pattern size is achieved with the FWHM shrinking from 235 nm to 178 nm and from 327 nm to 278 nm, respectively. In both cases the pixel dwell time has been set to 5 ms and the bleaching effect of the excitation laser has led to almost complete bleaching at and around the center. If we now consider

---

[4] Employing a halfmoon phase plate (see figure 4.5 (A)) a focal peak intensity of $\mathrm{I}_{\mathrm{STED}}$ = 1.9 GW/cm^2 corresponds to $\mathrm{I}_{\mathrm{STED}}$ = 3.8 GW/cm^2 for a gaussian beam - the maximum value applied in the measurements of figure 4.1 (C).

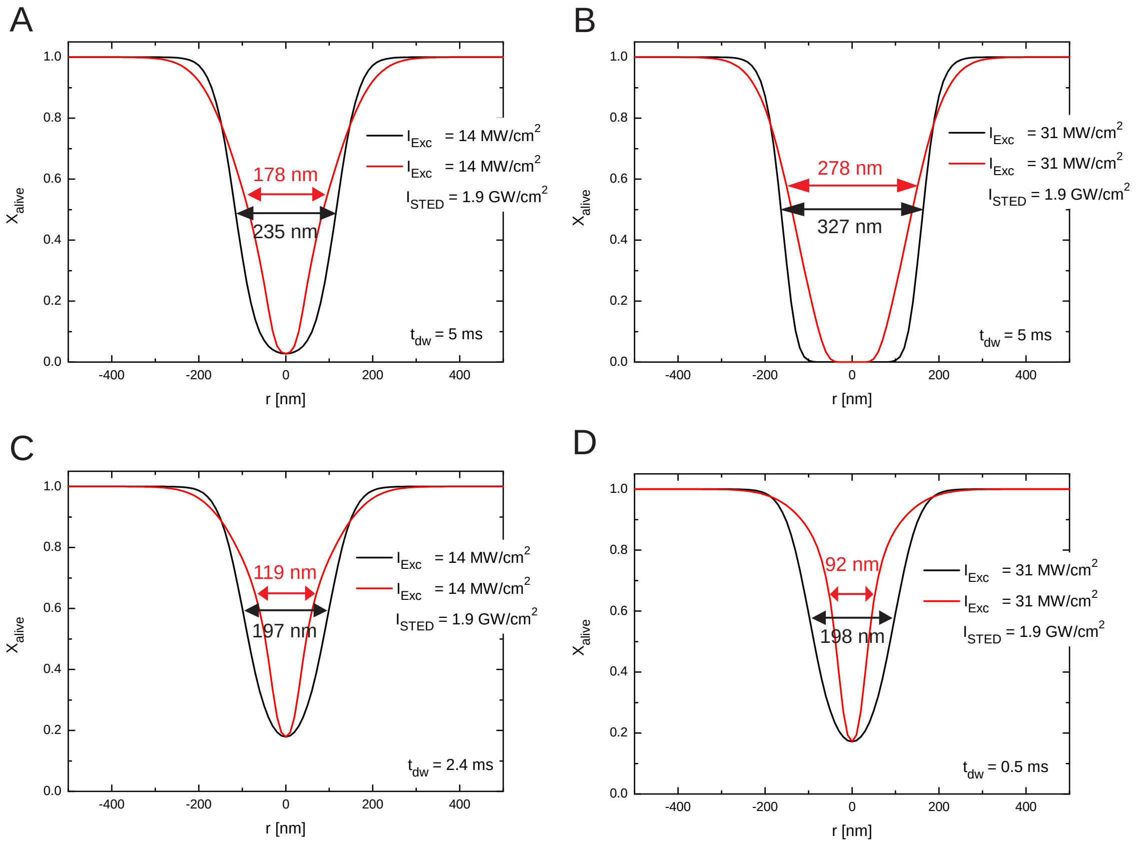

Figure 4.6: FWHM of spots bleached by superimposed 488 nm excitation and spatially altered STED beam. (A) and (B) correspond to experimental conditions applied in the measurements of figure 4.1 whereas (C) and (D) exemplify the ideal conditions with optimized dwell time for $X_{alive} = 20\%$.

the pixel dwell time dependency of the bleaching suppression effect a different situation is encountered. By adapting the dwell time such that $X_{alive} = 20\%$, which is a value that still gives a large writing contrast, the full width half maxima can be narrowed much stronger. For a bleaching focal peak intensity of $I_{exc} = 14 \text{ MW/cm}^2$ and a pixel dwell time of 2.4 ms a FWHM of only 119 nm is registered - a value significantly below the resolution limit of $\sim$ 200 nm for a 488 nm writing beam. Even better results are obtained if a higher writing irradiancy of $I_{exc} = 31 \text{ MW/cm}^2$ is applied with a pixel dwell time of 0.5 ms. In this case the FWHM is narrowed down to 92 nm in the simulations providing a proof of principle for subdiffraction nanolithography using stimulated emission depletion.

It has been mentioned previously in the text that the effect of photobleaching suppression using STED is strongly dependent on the pixel dwell time τ_{dw}. This dependency is certainly worth some further examination. Therefore, the fraction of unbleached molecules X_{alive} in

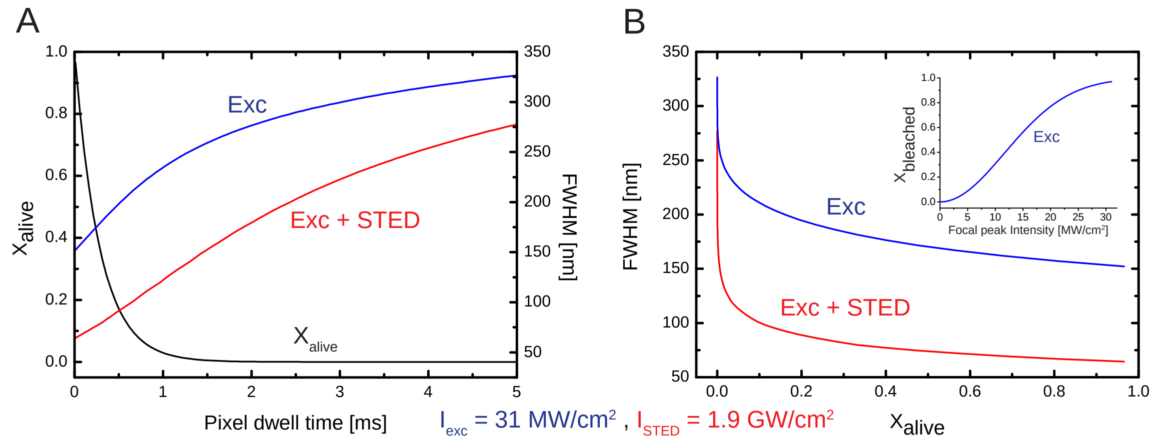

Figure 4.7: (A) Plotting the fraction of unbleached molecules X_{alive} in the center of the writing beam against the pixel dwell time for a writing intensity of $I_{\text{exc}} = 31$ MW/cm^2 shows that sufficient signal contrast ($X_{\text{alive}} \leq 0.2$) is obtained for a pixel dwell time for ~ 0.5 ms. Superimposing the 488 nm writing beam with a STED beam ($I_{\text{STED}} = 1.9$ GW/cm^2) featuring a central zero leads to significantly shorter line widths. At a suitable dwell time of 0.5 ms the FWHM is reduced from 198 nm to 92 nm using STED (compare figure 4.6 (D)). (B) The course of the FWHM is plotted as a function of X_{alive} for fixed I_{exc} and I_{STED} and varying pixel dwell time. Increasing X_{alive} leads to narrower line widths but also to a loss of image contrast. The inset displays the fraction of bleached molecules X_{bleached} for increasing values of I_{exc} up to 31 MW/cm^2 ($\tau_{\text{dw}} = 1$ ms). Note the sigmoidal curvature of the graph.

the center of the writing beam is determined as a function of pixel dwell time under fixed irradiation with excitation/bleaching and STED light (figure 4.7 (A)). The calculation has been performed one-dimensionally with a STED beam featuring a central zero according to figure 4.5 (B). Assuming a perfect zero intensity zone in the center of the STED beam the course of the graph will be the same for the two cases of writing solely with the excitation beam and writing with overlaid excitation and STED beam. Obviously, above a pixel dwell time of approximately 1 ms nearly all molecules are bleached. Good signal contrast between written spot and surrounding ($X_{\text{alive}} \approx 0.2$) is achieved up to $\tau_{\text{dw}} \approx 0.5$ ms. It can be directly read off the graph that for either of the two writing procedures the resulting FWHM increases as τ_{dw} is temporally extended (red and blue lines). Nevertheless, the FWHM is well below the diffraction limit up to $\tau_{\text{dw}} \approx 2$ ms if a STED beam is switched on (red line) with the effect of bleaching suppression through STED being most pronounced at comparatively short illumination times below 1 ms. A good tradeoff between sufficient image contrast and enhanced writing resolution is found at $\tau_{\text{dw}} = 0.5$ ms. Here the fraction of unbleached molecules is 20% and the resulting line width of the written pattern is 92 nm as compared to 198 nm if no STED beam is applied (compare also figure 4.6 (D)). At larger pixel dwell times $X_{\text{alive}} \rightarrow 0$ in the center of the beam and the FWHM are broadened which is a consequence of enhanced photobleaching in the beams' outer parts. Since the FWHM and $\mathrm{X}_{\mathrm{alive}}\,(\tau_{\mathrm{dw}})$ are monotonous functions we can directly plot the FWHM to corresponding values of $\mathrm{X}_{\mathrm{alive}}$ (figure 4.7 (B)). Here, $\mathrm{I}_{\mathrm{exc}}$ and $\mathrm{I}_{\mathrm{STED}}$ are constant whereas τ_{dw} is varied. The initial strong decay of the graphs right away catches the eye and is readily explained by saturated bleaching in large areas around the focal zone as $\mathrm{X}_{\mathrm{alive}} \rightarrow 0$. Again, note the considerably smaller line width in case of bleaching suppression by STED. With increasing $\mathrm{X}_{\mathrm{alive}}$ the FWHM further shrinks in a close to linear manner. Yet, there is a another very intriguing feature of figure 4.7 (B) concerning the pattern width of spots written solely by the 488 nm writing beam at large fractions of unbleached molecules ($\mathrm{X}_{\mathrm{alive}}$ = 0.6 - 1). In this region the full width half maxima take on values down to 150 nm which is below Abbe's diffraction limit of $\sim$ 200 nm. This result might at first glance appear to be unphysical but becomes clearer when the inset graph in figure 4.7 (B) is examined. In that depiction the dependency of the fraction of bleached molecules $\mathrm{X}_{\mathrm{bleached}}$ on the writing intensity is shown for the 488 nm beam at τ_{dw} = 1 ms. The curvature of the graph clearly is sigmoidal which means that bleaching is comparatively weak at low writing intensity and is then strongly enhanced as $\mathrm{I}_{\mathrm{exc}}$ is augmented before it becomes weaker again due to saturation effects. This behaviour also has implications on the FWHM in STED nanolithography: Thinking in doses low writing intensities are equivalent to higher intensities at lower dwell times and thus equivalent to regions of $\mathrm{X}_{\mathrm{alive}} \approx 1$ in the main graph of figure 4.7 (B). The probability p_{bl} of a molecule to bleach in our model is a product of the probability $\mathrm{p}_{\mathrm{S}_0\rightarrow\mathrm{S}_1}$ to be excited from S_0 to S_1 and the probability $\mathrm{p}_{\mathrm{S}_1\rightarrow\mathrm{S}_\mathrm{n}}$ to be further excited to the bleaching-prone state S_n:

$$p_{\mathrm{bl}} = p_{\mathrm{S}_0\rightarrow\mathrm{S}_1} \cdot p_{\mathrm{S}_1\rightarrow\mathrm{S}_\mathrm{n}} \tag{4.8}$$

At very low doses of light both $\mathrm{p}_{\mathrm{S}_0\rightarrow\mathrm{S}_1}$ and $\mathrm{p}_{\mathrm{S}_1\rightarrow\mathrm{S}_\mathrm{n}}$ are small which results in an even smaller probability p_{bl} to bleach. Hence $\mathrm{X}_{\mathrm{alive}}$ in the beam's outer part remains high during illumination and the resulting FWHM may take on values that are smaller than $\Delta r = \lambda\,/\,2\mathrm{NA}$ = 175 nm (for a 488 nm beam). Subdiffraction writing in this scheme is therefore a consequence of bleaching being a multi-step process.

Probably one of the greatest benefits of STED imaging is the fact that resolution is merely restricted by technical impediments (e. g., limited power or optical imperfections) with the STED intensity $\mathrm{I}_{\mathrm{STED}}$ dependent FWHM Δr obeying a modification of Abbe's equation:

$$\Delta r \geq \lambda / \left(2n \cdot \sin\alpha\sqrt{1 + I_{\mathrm{STED}}/I_{\mathrm{sat}}}\right) \tag{4.9}$$

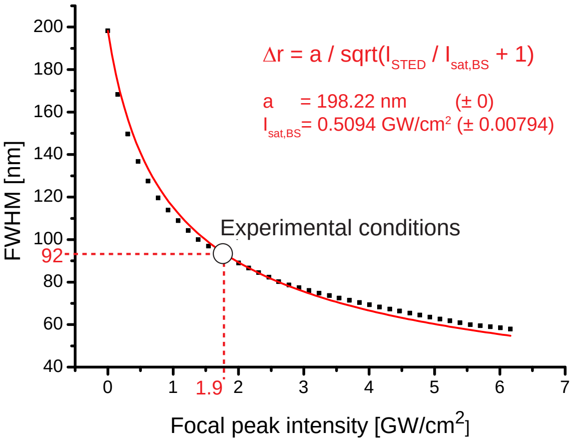

Figure 4.8: Plot of the bleached FWHM as a function of STED power using the estimated bleaching cross sections in equation (4.7) at an excitation/bleaching intensity of 31 MW/cm^2 and a dwell time of τ_{dw} = 0.5 ms. The dashed red lines mark the attainable FWHM at the experimentally applied STED power. The red line is the result of a fit to equation (4.10).

where $\mathrm{I_{sat}}$ is the saturation intensity. The question arises whether a similar regularity can be found for STED nanolithography. To this end the calculated FWHM Δr of a written pattern as a function of STED intensity $\mathrm{I_{STED}}$ is investigated for $\mathrm{I_{exc}}$(488 nm) = 31 MW/cm^2 and τ_{dwell} = 0.5 ms (black dots in figure 4.8). In close analogy to equation (4.9) a fitting function

$$\Delta r = a/\sqrt{I_{\mathrm{STED}}/I_{\mathrm{sat,BS}} + 1} \tag{4.10}$$

is defined where a is a constant factor and $\mathrm{I_{sat,BS}}$ is the saturation intensity of bleaching suppression using STED. Data in figure 4.8 is well described with $a \approx$ 198.22 nm and $\mathrm{I_{sat,BS}} \approx$ 0.5094 GW/cm^2 which means that just like in STED imaging the resulting FWHM as a function of STED intensity follows a square-root law. However, at STED intensities beyond $\sim$3 GW/cm^2 the fit slightly underestimates the full width half maxima of the written structure. This is a consequence of multi-photon bleaching by the STED beam which is incorporated in the simulations through bleaching cross section $\delta^*_{1n,\mathrm{bl}}$ (compare equation (4.7)) but not accounted for in the fitting function. At larger STED intensities this process becomes more pronounced and thus leads to even broader line widths. Even higher STED intensities will enhance the effect until finally multi-step STED induced bleaching will undesirably prevail over bleaching suppression by STED.

The white spot in figure 4.8 marks the maximum STED intensity $\mathrm{I_{STED}}$ = 1.9 GW/cm^2 applied in the experimental approach. At this STED intensity a pattern width of 92 nm can be expected (compare figure 4.6). Yet, the graph nicely reveals that even smaller patterns would

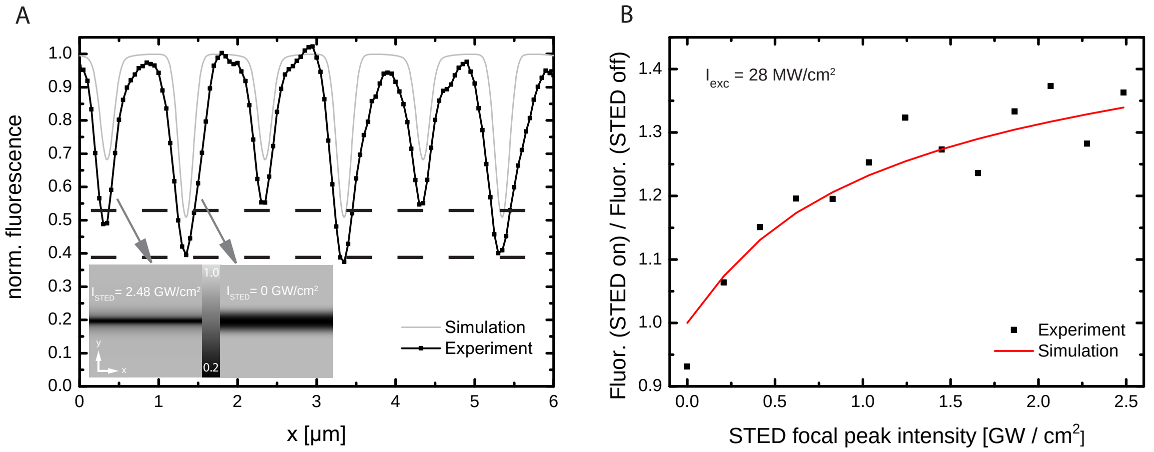

Figure 4.9: (A) Line profile obtained from bleaching small lines in a layer of dye KK114 with a 488 nm laser and the STED beam switched off every other line. 635 nm readout in combination with simulations confirm that the higher signal level obtained with STED is consistent with a considerably smaller line width (see inset). (B) Plotting the quotient [fluorescence (STED on) / fluorescence (STED off)] versus STED intensity for a 488 nm bleaching intensity of 28 $\mathrm{MW/cm^2}$ shows the increase expected from simulations that predict subdiffraction resolution of the written spots.

be written if the STED intensity could be further augmented. Tripling the STED power is predicted to yield line widths of less than 60 nm which again demonstrates that the presented approach to STED nanolithography does not have a fundamental limit of pattern size.

Experiment

In order to experimentally proof the resolution enhancement in optical writing with STED we have written lines into the KK114 dye layer along one axis with the 488 nm laser and added the phase-shaped STED beam in every other line (figure 4.9). The experiment is very similar to that of figure 4.1(C) except that this time a shaped PSF featuring a pronounced central zero in one dimension is utilized for the STED beam (see figure 4.5(B)) and the step size is enlarged to 200 nm along the writing axis. In this manner lines are produced without overlap of the PSFs during the writing process. Figure 4.9(A) shows profiles of the fluorescence signal collected when scanning the bleached lines with a diffraction-limited 635 nm laser spot of low power (< 1 μW, black line) and adding up the signal along the writing axis. The grey lines correspond to the result expected from theory. Also included are simulated images of the lines written with and without STED beam exemplifying the subdiffraction line width of ~90 nm in the former case. To visualize subdiffraction STED nanolithography it is drawn on the following rationale: The usage of a phase mask for the STED beam with a central intensity close to zero ($< 0.1\%$ in experimental action) should entail no difference in remaining fluorescence in the central position of the bleached spot. Yet, the bleaching spot's FWHM is expected to be narrower if the STED beam is switched on as shown by the simulated lines in the inset of figure 4.9(A). The signal during confocal readout is collected also from the minimum's surrounding which results in a smaller dip in the signal for lines of smaller width and equal contrast. Exactly this behaviour is observed experimentally in the graphs of figure 4.9(A). Simulations of the entire process (grey lines) show good agreement with experimental results and only differ slightly in absolute values giving further evidence for subdiffraction nanolithography using STED. The small difference in offset may, for example, be accounted to experimental imperfections such as sample drift or residual intensity in the focal center of the STED light.

Since the described measurements have been carried out for various STED powers the relative signal in the minima of the recorded profile between STED and confocal writing mode can be plotted against the STED power. The result is depicted in figure 4.9(B). Expectedly, the fraction gets larger as the STED power is risen which is in accordance with having written narrower line widths. Good agreement with simulated data (red line) further corroborates the declaration of having achieved subdiffraction STED nanolithography.

Optimizations

Similar results are achieved with another organic dye Atto 647 N (data not shown), which as well is characterized by a very low population of the triplet state. However, the approach fails on dyes absorbing in the visible range such as Fluorescein and Rhodamine 110 possibly due their higher triplet buildup. The relatively large triplet population exposes a too efficient pathway for photobleaching by the STED light. [65] Since photobleaching cross sections are a measure of a molecule's probability to photobleach they provide further insight into the underlying kinetics. For the STED lithography approach presented here, the influence of the individual photobleaching pathways (via excitation at λ = 488 nm and/or via STED at λ = 780 nm) is relevant in terms of attainable line width. Therefore, figure 4.10(A) displays a written line's FWHM for varying values of bleaching cross sections $\sigma_{\mathrm{1n,bl}}$ and $\sigma^*_{\mathrm{1n,bl}}$. The intensities I_{exc} = 31 MW/cm^2 and I_{STED} = 1.9 GW/cm^2 are kept constant and the pixel dwell time is adjusted for a fraction of 80% photobleached molecules in the written line's center - a value that provides sufficient contrast. The largest resolution enhancement is reached at combinations of strong excitation bleaching $\sigma_{\mathrm{1n,bl}}$ and low STED bleaching $\sigma^*_{\mathrm{1n,bl}}$. A striking feature of figure 4.10(A) is the dependency of the FWHM solely on the ratio of the bleach-

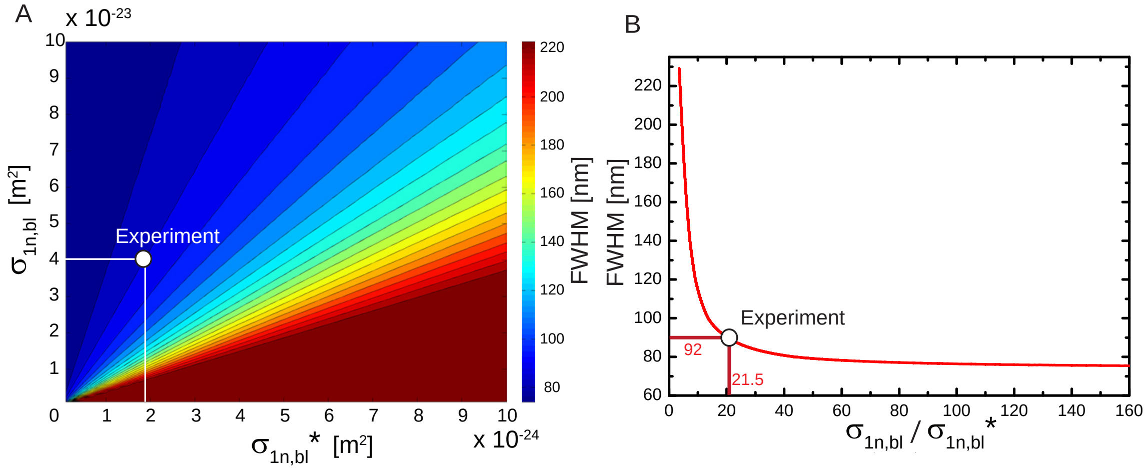

Figure 4.10: (A) 2D-plot of the attainable FWHM as a function of excitation bleaching cross section $\sigma_{1n,bl}$ and STED bleaching cross section $\sigma^*_{1n,bl}$ where the pixel integration time is adjusted such that 80% of the molecules are bleached (I_{exc} = 31 MW/cm^2). The spot within the map marks the best possible FWHM for the cross sections obtained from fitting experimental data of dye KK114. (B) Plotting the achievable FWHM versus the ratio $\sigma_{1n,bl}$ / $\sigma^*_{1n,bl}$ yields an exponential decay. Large ratios - i. e., strong excitation bleaching and low STED bleaching of the dye - result in sub-80 nm patterning under the given conditions. With a ratio of 21.5 for the used dye a FWHM of approximately 92 nm is already realizable in our experiment.

ing cross sections $\sigma_{1n,bl}$ / $\sigma^*_{1n,bl}$. As depicted in figure 4.10(B) the FWHM of the bleached lines decreases exponential-like with this ratio (and even takes on values larger than the diffraction-limited line width of ≈ 200 nm for $\sigma_{1n,bl}$ / $\sigma^*_{1n,bl} < 5$ where the STED light dominates the photobleaching and results in a bleaching enhancement instead of suppression). In the current simulations based on the properties of dye KK114 and the light intensities given above, the lowest achievable FWHM is ~75 nm. Note that unlimitedly lower values can be reached when increasing I_{STED} (compare figure 4.8).

Consequently, optimized experimental conditions correspond to large values of $\sigma_{1n,bl}$ and low values of $\sigma^*_{1n,bl}$. This is achieved by selecting a suitable dye (exhibiting low STED bleaching) and a writing wavelength that maximizes $\sigma_{1n,bl}$. In the experiments presented here these criteria are fulfilled by choosing an excitation wavelength blue-shifted with respect to the dye's absorption maximum and by selecting photostable fluorophores that have previously served well in STED nanoscopy. [139, 141] According to figure 4.10 the addition of an adequate anti-bleaching agent that selectively inhibits bleaching by the STED beam is expected to improve resolution since the ratio of the bleaching cross sections $\sigma_{1n,bl}/\sigma^*_{1n,bl}$ would by this means be enlarged. The addition of anti-bleaching agent Trolox which is known to work well for several dyes [142, 143] altogether did not improve the results as it undesirably prevented bleaching by the excitation beam, as well.

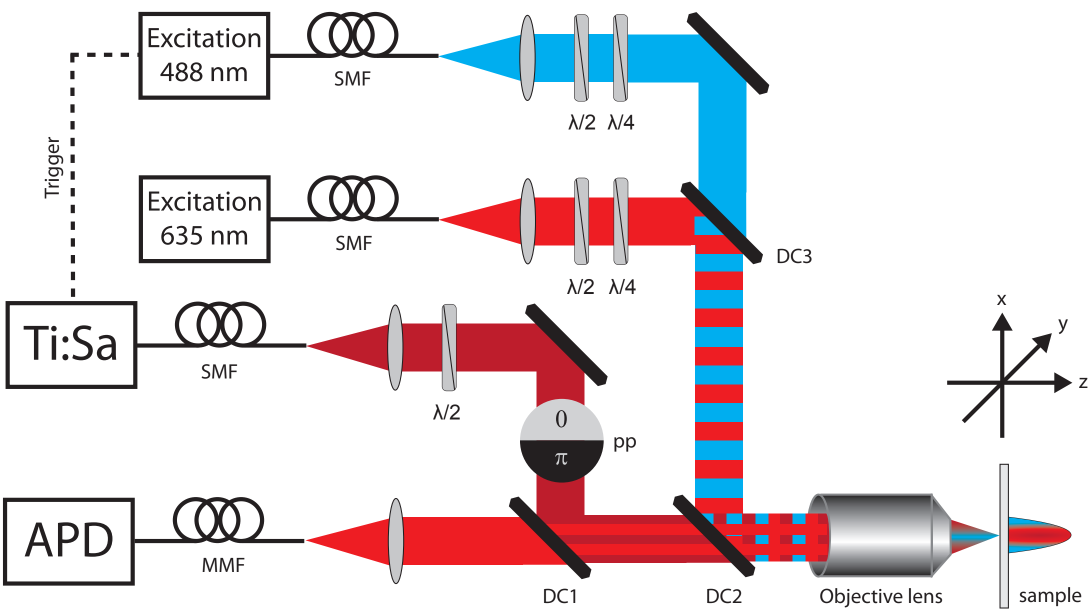

Figure 4.11: The optical setup employed for STED nanolithography. A stage-scanned sample is patterned by 488 nm excitation/bleaching light provided by a pulsed diode laser. STED light is taken from a 780 nm Ti:Sa-laser and structural readout is performed by a 635 nm pulsed laser diode at low power. Beams are superimposed by dichroic mirrors and fluorescence light is detected by an avalanche photodiode (APD). For pulse-stretching and beam shape cleanup single mode fibers (SMF) are employed.

4.3 Experimental section

After having presented the concept and the results of STED nanolithography using photobleaching suppression the character of this section is more technical and intends to comprehensively inform about experimental details. Especially, the utilized optical setup will be spotlighted but also all relevant parameters for measurement and computation will be pointed out.

4.3.1 STED microscope

The measurements have been performed on a custom-built STED-setup depicted in figure 4.11. STED light is provided by a femtosecond Ti:Sa-laser (mod. Mira900, Coherent, USA) operating at a wavelength of λ = 780 nm. Pumped by a 532 nm diode laser (Verdi V18, Coherent, USA) at a power of 14 W the Ti:Sa-oscillator produces 200 fs pulses with a repetition rate of 76 MHz. The output power is approximately 2.3 W. After temporally prestretching the pulses with glass rods the light is coupled into a 100 m single mode fiber

(Schäfter+Kirchhoff, Germany) for further pulse stretching to $\sim$ 300 ps and beam shape cleanup. Via dichroic filters (DC1 and DC2 in figure 4.11) the light enters a microscope objective (Leica HCX PL APO 100× NA 1.4, Leica, Germany) and is used for stimulated emission depletion.

Triggered by the Ti:Sa-oscillator a laser diode (PicoTA, Picoquant, Germany) generates pulsed light ($\tau \approx$ 150 ps, f = 76 MHz) with a wavelength of 488 nm and an output power of $\sim$ 3 mW. After passage of a single-mode fiber (Schäfter+Kirchhoff, Germany) and dichroic filters DC3 and DC2 (figure 4.11) the beam is spatially and temporally overlapped with the STED beam (by a custom-built electronic delay box). The 488 nm light is then used for optical writing in STED nanolithography.

For readout of written patterns a 76 MHz pulsed 635 nm diode laser (Picoquant, Germany) is used for red-emitting dyes. External triggering of the laser is not necessary since temporal overlap with either of the two other beams is not needed. The optical path of the beam is analogous to that of the blue beam.

Focal peak intensities are determined as described in section A.3.

Half-wave and quarter-wave plates (termed λ/2 and λ/4 in figure 4.11) are placed into each of the beam paths to produce circularly polarized light in the back aperture of the objective. Only mandatory for the use of 2D donut phase masks (compare figure 2.3) this also ensures the response of a maximum number of randomly distributed molecules in the sample. If spatial shaping of the STED light is desired to produce a PSF of the type shown in figure 4.5(A) a phase plate (pp) is inserted in the optical path imprinting a 0 - π phase jump on the wavefront in a semicircular area. As the phase plate requires linear polarization of the STED light the quarter-wave plate is removed during these measurements.

During data recording the sample is line-scanned by a piezo-stage (Melles Griot) through fixed beams. Fluorescence is then collected in Epi-direction and focused into a multi-mode fiber (MMF) (Thorlabs, Germany) for confocal detection. The number of photons is counted by an avalanche photodiode (APD) (Perkin Elmer, Canada).

4.3.2 Sample preparation

Samples were prepared by spin-coating $\sim$ 30 - 50 μL of aqueous dye solution (c $\approx$ 10 μM) on a cover slip at 4000-5000 rpm. The slip was then fixed to a microscope slide without the use of mounting media to avoid possible dark state generation in the dye molecules.

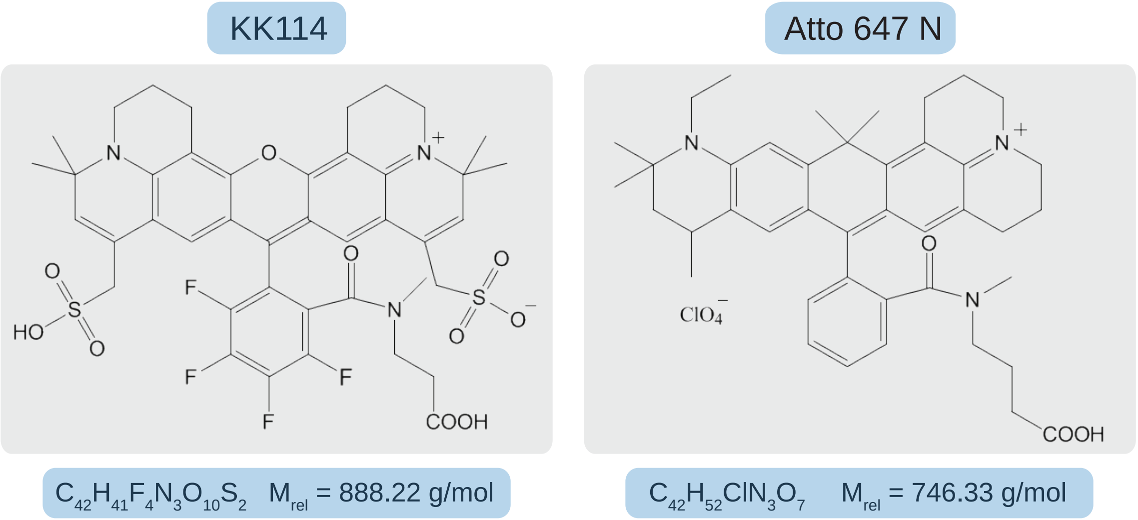

Figure 4.12: The chemical structures of the dyes KK114 and Atto 647 N which are used for STED nanolithography.

4.3.3 Dye characterization

Adequate dyes for optical writing with STED are the red-emitting fluorophores Atto 647 N (AttoTec, Germany) and KK114 (custom-made by Kolmakov *et al.*). [141] The chemical structures of the dyes' carboxylic acids are depicted in figure 4.12. KK114 belongs to the class of Rhodamine dyes and is characterized by a low intersystem crossing rate ($k_{ISC} = 1.8{\cdot}10^6\ s^{-1}$) and a high fluorescence quantum yield of 0.8. The dye's molar extinction coefficient (in water) at an absorption wavelength of 637 nm is ϵ_{637} = 92000 $Lmol^{-1}cm^{-1}$. Fluorescence emission occurs at a wavelength of λ_{em} = 660 nm.
Atto 647 N, on the other hand, is classified as a Carbopyronine dye and also features a low intersystem crossing rate of $k_{ISC} = 0.3 \cdot 10^6 s^{-1}$. The dye's quantum yield is 0.65 and the molar extinction coefficient at 644 nm (in PBS buffer) is ϵ_{644} = 150000 $Lmol^{-1}cm^{-1}$. Compared to KK114 the fluorescence of Atto 647 N is slightly red-shifted with a maximum at a wavelength of λ_{em} = 669 nm. Both dyes exhibit a triplet state lifetime of $\sim$ 3.3 μs which was determined by FCS measurements. [144] The assumption that the triplet state may be neglected in our model (compare figure 4.1 (A)) has been tested by incorporating it with intersystem crossing rate k_{ISC} and triplet relaxation rate k_T according to figure 4.13. Calculations suggest that dye KK114 excited with a typical 488 nm irradiation of 31 MW/cm^2 at an integration time of 5 ms [5] has a maximum triplet buildup of only $\sim$ 2.5%. If a gaussian-shaped STED

---

[5] At the given excitation irradiance a dwell time of 5 ms is sufficient to bleach (nearly) all molecules.

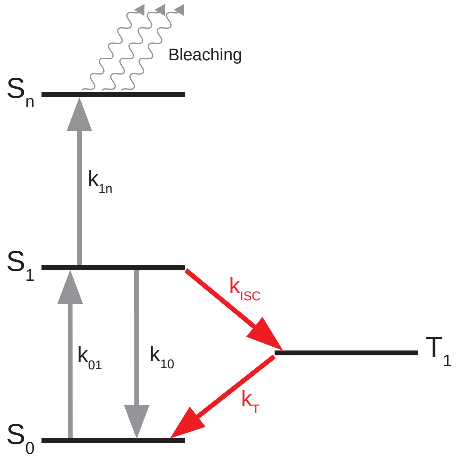

Figure 4.13: The electronic state model of the dyes used hitherto (figure 4.1 (A)) is expanded by the triplet state and its interconversion rates k_{ISC} and k_T to calculate the triplet buildup.

beam with an intensity of 3.7 GW/cm^2 is also switched on the maximum triplet buildup drops even further down to $\sim$ 0.001%. This can be explained by having a very low population of the S_1-state at all times since the molecules are either further excited to higher singlet states S_n or are depleted to the ground state S_0 by the STED beam. Thus the fraction of molecules available for intersystem crossing is very low. All in all these findings substantiate the approach to omit the triplet state during simulations of STED nanolithography with dyes KK114 and Atto 647 N.

4.3.4 Measurements

The software Imspector (custom-built by Dr. A. Schönle) was used for data acquisition while data analysis and simulations were carried out using the software MatLab (Mathwork, USA). The fit of the bleach suppression factor in figure 4.1 (C) leading to the bleaching cross sections in equations (4.7) is the basis for all subsequent simulations. Table 4.1 therefore summarizes all pertinent parameters used in the simulations and states in note form how they were acquired. Fluorescence lifetime imaging (FLIM) measurements using samples prepared as described yielded a fluorescent lifetime of τ_{fl} = 2.9 ns for dye KK114.
The absorption cross section $\sigma_{\mathrm{exc}}\,(488\mathrm{nm}) = 1.57 \cdot 10^{-18}\mathrm{cm}^2$ has been obtained in the following way (see figure 4.14 for an illustration): First, the absorption cross section $\sigma_{\mathrm{exc}}\,(633\mathrm{nm}) = 1.73 \cdot 10^{-16}\ \mathrm{cm}^2$ at an excitation wavelength of 633 nm is determined from the fluorescence excitation spectrum. Since the dye is excited at 488 nm in this project the according

Parameter	Value	Origin of data
Pulse shape	Gaussian	measured
Pulse delay (Exc ↔ STED)	70 ps	measured
$\sigma_{\text{exc}}\,(488\text{nm})$	$1.57{\cdot}10^{-22}$ m^2	measured
τ_{exc}	150 ps	measured
σ_{STED}	$6.75{\cdot}10^{-21}$ m^2	fluorescence emission spectrum
τ_{STED}	300 ps	measured
τ_{fl}	2.9 ns	lifetime measurements
repetition rate	76 MHz	used in experiment

Table 4.1: List of used parameters for the fit in figure 4.1 (C) and subsequent simulations.

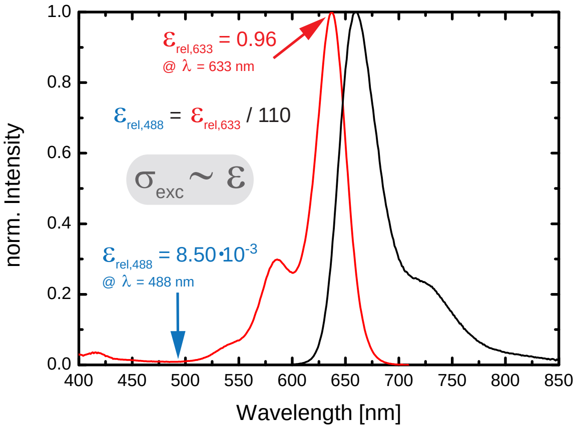

Figure 4.14: The relative absorption of dye KK114 (in water) at a wavelength of 633 nm is 0.96. Absorption at 488 nm is lower by a factor of ~ 110. If the direct proportionality between extinction coefficient and absorption cross section is taken into account the absorption cross section at 488 nm can be estimated from the measured absorption cross section at 633 nm.

cross section $\sigma_{\text{exc}}\,(488\text{nm})$ has been extrapolated by comparing the molar extinction coefficients at the two wavelengths. This is justified because of a direct proportionality between molar extinction coefficient and absorption cross section. [145] Since for KK114 the absorption at 488 nm is smaller by a factor of 110 compared to absorption at 633 nm the absorption cross section used for the simulations is $\sigma_{\text{exc}}\,(488\text{nm}) = \sigma_{\text{exc}}\,(633\text{nm})/110 = 1.57 \cdot 10^{-22}\text{cm}^2$ which is exactly the value given in table 4.1.

The spectral dependence of the cross section for stimulated emission is given by

$$\sigma_{\text{STED}}\,(\lambda) = \frac{\lambda^4 E\,(\lambda)}{8\pi c n \tau} \tag{4.11}$$

with c the speed of light in vacuum, n the refractive index and τ the lifetime of the S_1

state. [146, 147] The line shape function $\mathrm{E}(\lambda)$ was determined from the dye's fluorescence emission spectrum via $Q = \int E(\lambda)\ \mathrm{d}\lambda$ where Q is the quantum efficiency.

Figure 4.1 (B) was obtained by writing bleached lines in a layer of dye with the STED beam alternately switched on and off. In x- and y-direction the step size of the piezo stage was 15 and 1500 nm, respectively, and the pixel dwell time was 10 ms.

In Figure 4.1 (C) the piezo step size in x-direction was increased to 1 μm in order to eliminate prebleaching due to overlap of the PSFs along the axis (in y-direction the step size was 1 μm, too). The illuminated area was 100 $\mu\mathrm{m}^2$ (10 $\times$ 10 pixels) in total. For excitation irradiancies of 14 and 31 MW/cm^2 the STED irradiancies were varied between 0 and 3.6 GW/cm^2 in 19 and 18 steps, respectively. Each measurement series was repeated 4 ($\mathrm{I}_{\mathrm{exc}}$ = 14 MW/cm^2) and 6 ($\mathrm{I}_{\mathrm{exc}}$ = 31 MW/cm^2) times, respectively, at different sample positions to account for possible inhomogeneities in dye concentration. In the former case 5 additional measurement series were performed at some individual STED powers to increase reliability of the data. The pixel dwell time during writing was 5 ms for these measurements.

In the fitting procedure the system of equations (4.3) was solved numerically with a robust differential equations solver in MatLab (built-in function *ode45*) for a pulsed time dependence of $\mathrm{I}_{\mathrm{exc}}$ and $\mathrm{I}_{\mathrm{STED}}$. Not every pulse needed to be computed separately. After a few pulses an equilibrium of bleaching amount per pulse and total nonbleached population was reached, greatly increasing calculation speed. The fitting of the bleaching cross section was done in two steps. At first, $\sigma_{\mathrm{1n,bl}}$ is determined by a numerical least-squares fit of $\mathrm{X}_{\mathrm{alive}}$ using equations (4.3) for the case $\mathrm{I}_{\mathrm{STED}}$ = 0. As each individual measurement included data for this case the number of data is large and the resulting value of $\sigma_{\mathrm{1n,bl}}$ is supposed to be well reliable. Next, $\mathrm{X}_{\mathrm{alive}}$ as a function of STED power is fitted numerically for $\sigma^*_{\mathrm{1n,bl}}$ and $\delta^*_{\mathrm{1n,bl}}$ keeping the previously determined value of $\sigma_{\mathrm{1n,bl}}$ fixed. The bleach suppression factor can then be calculated via $\mathrm{BSF} = (1 - \mathrm{X}_{\mathrm{alive}}\,(\mathrm{STED}))\,/\,(1 - \mathrm{X}_{\mathrm{alive}})$.

Mapping of the bleach suppression factor as a function of excitation and STED intensity (figure 4.4) has been performed using the fitted bleaching cross sections. To account for the BSF's dependency on the pixel dwell time we chose to calculate it at a fraction of 50% bleached molecules with the dwell time adapted accordingly.

The PSF of figure 4.5 (A) was obtained by detecting 780 nm STED light scattered off gold beads (diameter d = 80 nm) with a photomultiplier tube incorporated in the experimental setup (see also section 2.2.3). Less than 0.1% of residual light intensity and thus a close to perfect zero was measured in the center of the PSF.

Experimental data in figure 4.9 was acquired analogously to data from figure 4.1 (C) except for a decreased step size of 200 nm along the written line. Additionally, a phase plate was inserted in the STED beam path that π-shifts half of the wavefront in order to produce a STED PSF exhibiting a central zero. [148] The excitation intensity of the 488 nm laser was chosen to be 28 MW/cm^2 and the pixel dwell time was 0.5 ms which, according to figure 4.6 (C), should be optimal at the given excitation intensity.

Simulations in figures 4.6 (C-F), 4.9 and 4.10 were carried out as before but instead of computing with a gaussian STED PSF a phase-shaped STED PSF with a central zero intensity zone is employed (compare figure 4.5 (A)).

4.4 Summary

Inspired by continuing industrial demand for further miniaturization in lithographic patterning and (optical) data storage a subdiffraction far-field writing technique has been introduced that circumvents the rather complex setups required for classical lithography.

The very basis of the approach is the experimental finding that stimulated emission depletion (STED) - so far only applied in optical imaging - can partially prevent dye molecules from bleaching by another laser by keeping them in the nonbleaching S_0 ground state. An appropriate photophysical model has been devised that ascribes this effect to enhanced $\mathrm{S}_1 \rightarrow \mathrm{S}_0$ de-excitation which outbalances potential excitation of the molecules to bleaching prone singlet states S_n through the other laser (dark state populations need to be negligible at any time as is the case for dyes KK114 and Atto 647 N). Unlike in optical imaging the excitation laser in STED nanolithography is intendedly strongly bleaching to serve as a writing beam. This is accomplished by exciting the dye far blue-shifted to its absorption maximum in order to reach highly excited singlet states. When superimposed with a phase-shaped STED beam that features a tiny zero-intensity zone in the center, subdiffraction patterns can be written. This is possible because bleaching takes place only in the beam's center whereas it is inhibited through stimulated emission depletion in its outer parts.

Following investigations to rule out that effects other than stimulated emission are responsible for bleaching suppression, a theoretical description of the effect is given based on underlying rate equations. Numerically fitting of bleaching cross sections to experimental data provides quantitative access to the phenomenon of bleaching suppression through STED.

Calculations using the fitted bleaching cross sections and a phase-shaped STED PSF confirm that subdiffraction patterns down to a size of $\sim$ 92 nm can be written with the present setup. In this context the pixel dwell time is shown to have notable influence on the written FWHM for it co-determines the fraction $\mathrm{X}_{\mathrm{alive}}$ of unbleached molecules. At this the regularity holds that larger values of $\mathrm{X}_{\mathrm{alive}}$ corresponding to smaller writing contrast enable smaller values of the FWHM. Hence, a tradeoff between contrast and FWHM is required.

To describe the exponential decay of a bleached spot's FWHM with increasing STED power the modified Abbe equation known from STED imaging may be applied with just minor changes. This works well for moderate STED powers but slightly underestimates the FWHM at higher STED powers due to neglect of multi-photon bleaching by the STED beam.

An (indirect) proof of the method's successful operation is given by comparing the fluorescence signal during confocal readout for the cases 'STED on' and 'STED off'. As expected from simulations the readout signal is higher in the former case because more fluorescent molecules are present in the focus if the FWHM of the bleached pattern is narrowed.

Interestingly, it was found that the FWHM depends exponentially on the ratio of excitation and STED bleaching cross sections with larger ratios resulting in smaller FWHM. Estimation of the bleaching cross sections combined with knowledge of intrinsic dye properties thus renders it possible to predict the achievable FWHM in STED nanolithography at a given STED power. In general it may be inferred that results are improved - i. e., FWHM are narrowed - if large excitation bleaching cross sections are combined with low STED bleaching cross sections in an experiment using short pixel dwell times and high STED intensities.

The present study may serve as the starting point for further investigations to exploit the potential of STED nanolithography. While an indirect proof of resolution increase has been given here, a direct observation thereof would certainly be desirable. Retrieving an additive that selectively inhibits STED bleaching would improve results even further. Moreover, the method's prospective in CW mode is worth being looked at carefully since CW lasers would not only facilitate the experimental setup but also induce a different - perhaps more favourable - bleaching behaviour. The invention of novel dyes with even less dark state buildup are expected to further improve results. Finally, sample preparation could be optimized through the addition of substances that produce homogeneous films without altering the dye's bleaching behaviour. [6]

---

[6] PMMA has been tested but worsened bleaching suppression through STED. PVA is known to yield additional dark states and to reduce the mobility of triplet-quenching oxygen and is therefore unsuited for STED nanolithography as well. [149, 150]

5 Conclusion and Outlook

This thesis describes both the development of multicolor STED imaging with macromolecular lateral resolution and the extension of the STED concept to subdiffraction optical writing. The former efforts result in dual-color images of neuronal proteins with unprecedented resolution and - combined with a novel sample sectioning technique - in a 3D reconstruction of dual-color STED images. The new concept of STED nanolithography is introduced and shown to be capable of writing patterns with $\sim$ 90 nm FWHM in the present configuration.

Dual-color STED nanoscopy demands high standards of both the employed fluorescent dyes and the optical setup as four beams - two excitation beams and two fluorescence depletion beams - need to be spatially superimposed. The choice of appropriate dyes in conjunction with adequate laser systems is therefore of major significance for this technique. Macromolecular resolution in two color channels (a 'green channel' operating with green-absorbing dyes and a 'red channel' working with red-absorbing dyes) is achieved by diligently adapting the employed laser systems to the photophysics of the dyes. Complete revision of the optical setup used for the first implementation of dual-color STED microscopy [48] thus leads to a further doubling of the red channel's resolution down to 33 nm whilst maintaining the green channel's resolution of 31 nm. This hitherto unmatched resolution enhancement in multicolor STED is proved by imaging 1:1-mixtures of red- and green-fluorescent dyes.

Going beyond mere demonstration of resolution capability the developed method succeeds in resolving features of biologically relevant neuronal proteins as small as approximately 35 nm. Colocalization studies of such systems potentially providing new biological insight thus become feasible.

As many, for instance, neuronal proteins build up highly three-dimensional structures it is of vital importance to extend superresolution to three dimensions. To this end the lateral resolution capacity of the developed dual-color STED microscope is combined with a novel sample sectioning technique. [68] Such ultrathin samples (d = 75-100 nm) provide extraordinary sharp images because they do not suffer from disturbing axial out-of-focus fluorescence. Most importantly, though, whole cells can be sectioned, imaged and afterwards be stacked to yield a three-dimensional view of the cell. In this way the first three-dimensional reconstruction of dual-color STED images with an effective resolution of $35\times35\times80$ nm^3 has been accomplished.

The red channel of the dual-color setup has also helped in elucidating the role of so-called precursor spheres during early steps in the assembly of photoreceptor ribbon synapses in the mouse retina. [67] By labeling the protein Bassoon STED microscopy reveals that the precursor spheres are actually composed of multiple units with an average diameter of approximately 130 nm which agrees well with electron microscopical data.

As the performance of STED nanoscopy is strongly correlated with the quality of the employed fluorescent dyes the invention and STED-related characterization of new fluorescent dyes is of utmost importance. Chapter 3 is therefore devoted to the characterization of a newly synthesized class of rhodamine dyes for STED nanoscopy. The fluorescence of the green-emitting dyes is shown to be well depletable using STED yielding saturation intensities comparable to that of established commercial dyes. A series of sub-40 nm resolving STED images taken with the green channel of the dual-color STED setup proves the bioconjugated dye's brightness and photostability under high intensity STED conditions.

An implementation of subdiffraction STED nanolithography is realized by exploiting the newly established effect of photobleaching suppression through STED in conventional dye layers. Thereby a strong bleaching laser is superimposed by a high-intensity STED laser which exhibits comparatively low photobleaching. Consequently, fluorophores are de-excited to the nonbleaching electronic ground state by the STED beam thus preventing higher excitation to bleaching-prone states. The effect is established both experimentally and theoretically by devising a compatible photophysical model. Experimental data is well described by numerical fittings based on underlying rate equations. Numerical simulations show that the utilization of a donut-shaped STED beam inhibits photobleaching in the beam's outer area whereas bleaching remains unperturbed in its center. Hence, bleached lines with subdiffraction FWHM can be written in a dye layer which is also (indirectly) proved by subsequent experiments.

The future of multicolor STED nanoscopy will see a simplified optical setup in combination with an extension of the resolution capacity to three dimensions in an all-optical approach. The advent of user-friendly supercontinuum laser sources may prove to be helpful in that respect. [116] The usage of a conventional and a large Stokes-shift dye could furthermore enable simultaneous operation of both color channels with only one STED laser.

In STED nanolithography the main task will be a direct observation of resolution enhancement which yet has not succeeded due to an imperfect readout procedure. Moreover, the invention of new fluorescent substances with tailor-made properties could boost the bleaching suppression effect. Due to its technical simplicity and easy sample preparation the technique could become an alternative to classical photolithography with optical data storage as possible field of application.

Bibliography

[1] S. Bradbury. *The evolution of the microsope*. Pergamon Press, London, 1965.

[2] H. Salih, M. Al-Amri, and M. El Gomati. The miracle of light. *A World of Science (UNESCO)*, 3:2–7, 2005.

[3] Timothy C. Kriss and Vesna M. Kriss. History of the operating microscope: From magnifying glass to microneurosurgery. *Neurosurgery*, 42:899–907, 1998.

[4] Albert E. Kalderon. The evolution of microscope design from its invention to the present days. *Am. J. Surg. Pathol.*, 7:95–102, 1983.

[5] Kutluay Uluç, Gregory C. Kujoth, and Mustafa K. Başkaya. Operating microscopes: past, present, and future. *Neurosurg. Focus*, 27:E4, 2009.

[6] Ernst C. Abbe. Beiträge zur Theorie des Mikroskops und der mikroskopischen Wahrnehmung. *Arch. Mikr. Anat.*, 9:413–468, 1873.

[7] Stefan W. Hell and Jan Wichmann. Breaking the diffraction resolution limit by stimulated emission: stimulated emission depletion microscopy. *Opt. Lett.*, 19(11):780–782, 1994.

[8] Alfred Kwok-Kit Wong. *Resolution enhancement techniques in optical lithography*. SPIE Press, 2001.

[9] Shuyang Su. *China - Eine Einführung in Geschichte, Kultur und Zivilisation*. Chronik Verlag, 2006.

[10] David N. Carvalho. *Forty centruries of ink*. Lenox Hill Pub. and Dist. Co., New York, 1904.

[11] Edda Bhattacharjee. Bi Sheng und Gutenberg und die beweglichen Lettern. *Information - Wissenschaft & Praxis*, 52(1):37–40, 2001.

[12] Alois Senefelder. *The invention of lithography*. New York: The Fuchs & Lang Manufacturing Company, 1911.

[13] Gerd Wedler. *Lehrbuch der physikalischen Chemie*. Wiley-VCH, 4th edition, 1997.

[14] Peter Atkins and Julio de Paula. *Physical Chemistry*. Oxford University Press, 7th edition, 2002.

[15] G. G. Stokes. On the change of refrangibility of light. *Phil. Trans. R. Soc. Lond.*, 142:463–562, 1852.

[16] A. H. Coons and M. H. Kaplan. Localization of antigen in tissue cells. II. Improvements in a method for the detection of antigen by means of fluorescent antibody. *J. Exp. Med.*, 91:1–13, 1950.

[17] O. Shimomura. The discovery of aequorin and green fluorescent protein. *J. Microsc.*, 217:3–15, 2005.

[18] M. Chalfie, Y. Tu, G. Euskirchen, W. Ward, and D. C. Prasher. Green fluorescent protein as a marker for gene expression. *Science*, 263:802–805, 1994.

[19] A. Paul Alivisatos, Weiwei Gu, and Carolyn Larabell. Quantum dots as cellular probes. *Annu. Rev. Biomed. Eng.*, 7:55–76, 2005.

[20] G. Palumbo and R. Pratesi. *Lasers and current optical techniques in biology*. The Royal Society of Chemistry, 2004.

[21] C. Eggeling, A. Volkmer, and C. A. M. Seidel. Molecular photobleaching kinetics of rhodamine 6g by one- and two-photon induced confocal fluorescence microscopy. *ChemPhysChem*, 6:791–804, 2005.

[22] K. I. Willig, B. Harke, R. Medda, and S. W. Hell. Sted microscopy with continuous wave beams. *Nature Methods*, 4(11):915–918, 2007.

[23] Lars Kastrup. *Fluorescence depletion by stimulated emission in single-molecule spectroscopy*. PhD thesis, University of Heidelberg, 2004.

[24] J. Keller, A. Schönle, and S. W. Hell. Efficient fluorescence inhibition patterns for resolft microscopy. *Opt. Express*, 15(6):3361–3371, 2007.

[25] Volker Westphal and Stefan W. Hell. Nanoscale resolution in the focal plane of an optical microscope. *Phys. Rev. Lett.*, 94:143903, 2005.

[26] Stefan W. Hell. Far-field optical nanoscopy. *Science*, 316:1153–1158, 2007.

[27] Peter W. Hawkes and John C. H. Spence. *Science of microscopy*, volume 1. Springer, 2007.

[28] John C. H. Spence. The future of atomic resolution electron microscopy for materials science. *Mat. Sci. Eng.*, R26:1–49, 1999.

[29] James K. Koehler. *Advanced techniques in biological electron microscopy III*. Springer-Verlag, 1986.

[30] W. Baumeister. Electron tomography: towards visualizing the molecular organization of the cytoplasm. *Curr. Opin. Struct. Biol.*, 12:679–684, 2002.

[31] Robert C. Dunn. Near-field scanning optical microscopy. *Chem. Rev.*, 99:2891–2927, 1999.

[32] Franz J. Giessibl. Advances in atomic force microscopy. *Rev. Mod. Phys.*, 75(3):949–983, 2003.

[33] P. Rai-Choudhury, editor. *SPIE handbook of microlithography, micromachining, and microfabrication*, volume 1. SPIE-The International Society for Optical Engineering, 1997.

[34] S. A. Rishton, H. Schmid, D. P. Kern, H. E. Luhn, T. H. P. Chang, G. A. Sai-Halasz, M. R. Wordeman, E. Ganin, and M. Polcari. Lithography for ultrashort channel silicon field effect transistor circuits. *J. Vac. Sci. Technol.*, B6(1):140–145, 1988.

[35] Marvin Minsky. Memoir on inventing the confocal scanning microscope. *Scanning*, 10:128–138, 1988.

[36] K. W. Dunn and P. A. Young. Principles of multiphoton microscopy. *Nephron Exp. Nephrol.*, 103:e33–e40, 2006.

[37] W. Denk, J. H. Strickler, and W. W. Webb. Two-photon laser scanning fluorescence microscopy. *Science*, 248:73–76, 1990.

[38] Jeff A. Squier, Michiel Müller, G. J. Brakenhoff, and Kent R. Wilson. Third harmonic generation microscopy. *Opt. Express*, 3:315–324, 1998.

[39] Bo Huang, Mark Bates, and Xiaowei Zhuang. Super-resolution fluorescence microscopy. *Annu. Rev. Biochem.*, 78:993–1016, 2009.

[40] Stefan W. Hell. Toward fluorescence nanoscopy. *Nat. Biotechnol.*, 21(11):1347–1355, 2003.

[41] Stefan Bretschneider, Christian Eggeling, and Stefan W. Hell. Breaking the diffraction barrier in fluorescence microscopy by optical shelving. *Phys. Rev. Lett.*, 98:218103, 2007.

[42] Michael Hofmann, Christian Eggeling, Stefan Jakobs, and Stefan W. Hell. Breaking the diffraction barrier in fluorescence microscopy at low light intensities by using reversibly photoswitchable proteins. *Proc. Natl. Acad. Sci. USA*, 102(49):17565–17569, 2005.

[43] E. Betzig, G. H. Patterson, R. Sougrat, O. W. Lindwasser, S. Olenych, J. S. Bonifacino, M. W. Davidson, J. Lippincott-Schwartz, and H. F. Hess. Imaging intracellular fluorescent proteins at nanometer resolution. *Science*, 313:1642–1645, 2006.

[44] Michael J. Rust, Mark Bates, and Xiaowei Zhuang. Sub-diffraction-limit imaging by stochastic optical reconstruction microscopy (STORM). *Nat. Methods*, 3:793–796, 2006.

[45] Samuel T. Hess, Thanu P. K. Girirajan, and Michael D. Mason. Ultra-high resolution imaging by fluorescence photoactivation localization microscopy. *Biophys. J.*, 91(11):4258–4272, 2006.

[46] Benjamin Harke, Chaitanya Ullal, Jan Keller, and Stefan W. Hell. Three-dimensional nanoscopy of colloidal crystals. *Nano Lett.*, 8(5):1309–1313, 2008.

[47] Bo Huang, Wenqin Wang, Mark Bates, and Xiaowei Zhuang. Three-dimensional super-resolution imaging by stochastic optical reconstruction microscopy. *Science*, 319:810–813, 2008.

[48] G. Donnert, J. Keller, C. A. Wurm, S. O. Rizzoli, V. Westphal, A. Schönle, R. Jahn, S. Jakobs, C. Eggeling, and S. W. Hell. Two-color far-field fluorescence nanoscopy. *Biophys. J.*, 92(8):L67–69L, 2007.

[49] Hannes Bock, Claudia Geisler, Christian A. Wurm, Stefan Jakobs, Andreas Schönle, Alexander Egner, Stefan W. Hell, and Christian Eggeling. Two-color far-field fluorescence nanoscopy based on photoswitching emitters. *Appl. Phys. B*, 88:161–165, 2007.

[50] Mark Bates, Bo Huang, Graham T. Dempsey, and Xiaowei Zhuang. Multicolor super-resolution imaging with photo-switchable fluorescent probes. *Science*, 317:1749–1753, 2007.

[51] H. Shroff, C. G. Galbraith, J. A. Galbraith, H. White, J. Gillette, S. Olenych, M. W. Davidson, and E. Betzig. Dual-color superresolution imaging of genetically expressed probes within individual adhesion complexes. *Proc. Natl. Acad. Sci. USA*, 104(51):20308–20313, 2007.

[52] Volker Westphal, Silvio O. Rizzoli, Marcel A. Lauterbach, Dirk Kamin, Reinhard Jahn, and Stefan W. Hell. Video-rate far-field optical nanoscopy dissects synaptic vesicle movement. *Science*, 320:246–249, 2008.

[53] Birka Hein, Katrin I. Willig, and Stefan W. Hell. Stimulated emission depletion (sted) nanoscopy of a fluorescent protein-labeled organelle inside a living cell. *Proc. Natl. Acad. Sci. USA*, 105(38):14271–14276, 2008.

[54] J. S. Biteen, Thompson M. A., N. K. Tselentis, G. R. Bowman, L. Shapiro, and W. E. Moerner. Super-resolution imaging in live *Caulobacter crescentus* cells using photoswitchable EYFP. *Nat. Methods*, 5:947–949, 2008.

[55] Stefan Hell and Ernst H. K. Stelzer. Properties of a 4pi-confocal fluorescence microscope. *J. Opt. Soc. Am. A*, 9:2159–2166, 1992.

[56] M. G. L. Gustafsson, D. A. Agard, and J. W. Sedat. I^5M: 3D widefield light microscopy with better than 100 nm axial resolution. *J. Microsc.*, 195:10–16, 1999.

[57] Roman Schmidt, Christian A. Wurm, Stefan Jakobs, Johann Engelhardt, Alexander Egner, and Stefan W. Hell. Spherical nanosized focal spot unravels the interior of cells. *Nat. Meth.*, 5(6):539–544, 2008.

[58] B. Bailey, D. L. Farkas, D. L. Taylor, and F. Lanni. Enhancement of axial resolution in fluorescence microscopy by standing-wave excitation. *Nature*, 366:44–48, 1993.

[59] Mats G. L. Gustafsson. Surpassing the lateral resolution limit by a factor of two using structured illumination microscopy. *J. Microsc.*, 198(2):82–87, 2000.

[60] Mats G. L. Gustafsson. Nonlinear structured-illumination microscopy: Wide-field fluorescence imaging with theoretically unlimited resolution. *Proc. Nat. Acad. Sci. U.S.A*, 102(37):13081–13086, 2005.

[61] S.W. Hell, S. Jakobs, and L. Kastrup. Imaging and writing at the nanoscale with focused visible light through saturable optical transitions. *Appl. Phys. A*, 77:859–860, 2003.

[62] Trisha L. Andrew, Hsin-Yu Tsai, and Rajesh Menon. Confining light to deep subwavelength dimensions to enable optical nanopatterning. *Science*, 324:917–921, 2009.

[63] Linjie Li, Rafael R. Gattass, Erez Gershgoren, Hana Hwang, and John T. Fourkas. Achieving $\lambda/20$ resolution by one-color initiation and deactivation of polymerization. *Science*, 324:910–913, 2009.

[64] Timothy F. Scott, Benjamin A. Kowalski, Amy C. Sullivan, Christopher N. Bowman, and Robert R. McLeod. Two-color single-photon photoinitiation and photoinhibition for subdiffraction photolithography. *Science*, 324:913–917, 2009.

[65] G. Donnert, J. Keller, R. Medda, M. A. Andrei, S. O. Rizzoli, R. Lührmann, R. Jahn, C. Eggeling, and S. W. Hell. Macromolecular-scale resolution in biological fluorescence microscopy. *Proc. Natl. Acad. Sci. USA*, 103(31):11440–11445, 2006.

[66] Lars Meyer, Dominik Wildanger, Rebecca Medda, Annedore Punge, Silvio O. Rizzoli, Gerald Donnert, and Stefan W. Hell. Dual-Color STED Microscopy at 30-nm Focal-Plane Resolution. *Small*, 4:1095–1100, 2008.

[67] Hanna Regus-Leidig, Susanne tom Dieck, Dana Specht, Lars Meyer, and Johann Helmut Brandstätter. Early steps in the assembly of photoreceptor ribbon synapses in the mouse retina: The involvement of precursor spheres. *J. Comp. Neurol.*, 512:814–824, 2009.

[68] Annedore Punge, Silvio O. Rizzoli, Andreas Schönle, Lars Kastrup, Lars Meyer, Jan D. Wildanger, Reinhard Jahn, and Stefan W. Hell. 3D reconstruction of high-resolution STED microscope images. *Microsc. Res. Tech.*, 71:644–650, 2008.

[69] Jeff W. Lichtman and Jose-Angel Conchello. Fluorescence microscopy. *Nat. Methods*, 2:910–919, 2005.

[70] T. Clark Brelje, Martin W. Wessendorf, and Robert L. Sorenson. Multicolor laser scanning confocal immunofluorescence microscopy: Practical application and limitations. *Methods Cell Biol.*, 70:165–244, 2002.

[71] B. Alberts, A. Johnson, J. Lewis, M. Raff, K. Roberts, and P. Walter. *Molecular Biology of the Cell.* Garland Science, New York, 4 edition, 2002.

[72] R. Y. Tsien, L. Ernst, and A. Waggoner. Fluorophores for confocal microscopy: Photophysics and photochemistry. In J. B. Pawley, editor, *Handbook of biological confocal microscopy*, pages 338–352. Springer, New York, 3 edition, 2006.

[73] Gerald Donnert. *Dual-colour STED microscopy on the nanoscale.* PhD thesis, University of Heidelberg, 2007.

[74] K. I. Willig, R. R. Kellner, R. Medda, B. Hein, S. Jakobs, and S. W. Hell. Nanoscale resolution in GFP-based microscopy. *Nature Methods*, 3(9):721–723, 2006.

[75] Katrin I. Willig. *STED microscopy in the visible range.* PhD thesis, University of Heidelberg, 2006.

[76] `https://www.atto-tec.com/`.

[77] `http://www.activemotif.com/`.

[78] Benjamin Harke. *3D STED microscopy with pulsed and continuous wave lasers.* PhD thesis, University of Göttingen, 2008.

[79] G. Donnert, C. Eggeling, and S. W. Hell. Major signal increase in flurorescence microscopy through dark-state relaxation. *Nat. Methods*, 4(1):81–86, 2007.

[80] Jan Keller. *Optimal de-excitation patterns for RESOLFT-Microscopy.* PhD thesis, University of Heidelberg, 2006.

[81] James B. Pawley (ed.). *Handbook of biological confocal microscopy.* Plenum Press, 1995.

[82] Eugene Hecht. *Optics.* Addison Wesley, 2002.

[83] M. Schrader, M. Kozubek, S. W. Hell, and T. Wilson. Optical transfer functions of 4pi confocal microscopes: theory and experiment. *Opt. Lett.*, 22(7):436–438, 1997.

[84] P. Török, P. D. Higdon, R. Juskaitis, and T. Wilson. Optimising the image contrast of conventional and confocal optical microscopes imaging finite sized spherical gold scatterers. *Opt. Commun.*, 155:335–341, 1998.

[85] Benjamin Harke, Jan Keller, Chaitanya K. Ullal, Volker Westphal, Andreas Schönle, and Stefan W. Hell. Resolution scaling in sted microscopy. *Optics Express*, 16(6):4154–4162, 2008.

[86] Thomas A. Klar. *Progress in Stimulated Emission Depletion Microscopy*. PhD thesis, Rupertus Carola University of Heidelberg, 2001.

[87] Lars Kastrup and Stefan W. Hell. Absolute optische Wirkungsquerschnitte fluoreszierender Einzelmoleküle. *Angew. Chem.*, 116(48):6814–6818, 2004.

[88] Lars Kastrup and Stefan W. Hell. Absolute optical cross section of individual fluorescent molecules. *Angew. Chem. Int. Ed.*, 43:6646–6649, 2004.

[89] K. Willig, J. Keller, M. Bossi, and S.W. Hell. STED microscopy resolves nanoparticle assemblies. *New J. Phys.*, 8:106, 2006.

[90] J. Fölling, V. Belov, R. Kunetsky, R. Medda, A. Schönle, A. Egner, C. Eggeling, M. Bossi, and S. W. Hell. Photochromic rhodamines provide nanoscopy with optical sectioning. *Angew. Chem. Int. Ed.*, 46:6266–6270, 2007.

[91] Ji-Xin Cheng and Sunney X. Xie. Coherent anti-stokes raman scattering microscopy: Instrumentation, theory, and applications. *J. Phys. Chem. B*, 108:827–840, 2004.

[92] Bruce Alberts, Alexander Johnson, Julian Lewis, Martin Raff, Keith Roberts, and Peter Walter. *Molekularbiologie der Zelle*. Wiley-VCH, 2004.

[93] `http://wwwalt.uniklinik-saarland.de/med_fak/physiol1/images/forsch2.jpg`.

[94] T. C. Sudhof. The synaptic vesicle cycle. *Annual Review of Neuroscience*, 27:509–547, 2004.

[95] David Bodian. An electron microscopic characterization of classes of synaptic vesicles by means of controlled aldehyde fixation. *J. Cell Biol.*, 44(1):115–124, 1970.

[96] Richard McIntosh, Daniela Nicastro, and David Mastronarde. New views of cells in 3D: an introduction to electron tomography. *Trends Cell Biol.*, 15(1):43–51, 2005.

[97] Mark K. Bennett, Jose E. Garcia-Arraras, Lisa A. Elferink, Karen Peterson, Anne M. Fleming, Christopher D. Hazuka, and Richard H. Scheller. The syntaxin family of vesicular transport receptors. *Cell*, 74:863–873, 1993.

[98] Roxanne C. Lariviere and Jean-Pierre Julien. Functions of intermediate filaments in neuronal development and disease. *J. Neurobiol.*, 58(1):131–148, 2004.

[99] Jean-Pierre Julien. Neurofilament functions in health and disease. *Curr. Opin. Neurobiol.*, 9(5):554–560, 1999.

[100] M. Dyba and S.W. Hell. Focal spots of size $\lambda/23$ open up far-field fluorescence microscopy at 33 nm axial resolution. *Phys. Rev. Lett.*, 88:163901, 2002.

[101] Lewis Melville, Sandy Dickson, Melissa L. Farquhar, S. E. Smith, and R. Larry Peterson. Visualization of mycorrhizal fungal structures in resin embedded tissues with xanthene dyes using laser scanning confocal microscopy. *Can. J. Bot.*, 76:174–178, 1998.

[102] Katrin I. Willig, Silvio O. Rizzoli, Volker Westphal, Reinhard Jahn, and Stefan W. Hell. Sted-microscopy reveals that synaptotagmin remains clustered after synaptic vesicle exocytosis. *Nature*, 440(7086):935 – 939, 2006.

[103] Marie E. Burns and George J. Augustine. Synaptic structure and function: Dynamic organization yields architectural precision. *Cell*, 83:187–194, 1995.

[104] Susanne tom Dieck, Lydia Sanmarti-Vila, Kristina Langnaese, Karin Richter, Stefan Kindler, Antje Soyke, Heike Wex, Karl-Heinz Smalla, Udo Kampf, Jürgen-Theodor Fränzer, Markus Stumm, Craig C. Garner, and Eckart D. Gundelfinger. Bassoon, a novel zinc-finger cag/glutamine-repeat protein selectively localized at the active zone of presynaptic nerve terminals. *J. Cell Biol.*, 142:499–509, 1998.

[105] Craig C. Garner, Stefan Kindler, and Eckart D. Gundelfinger. Molecular determinants of presynaptic active zones. *Curr. Opin. Neurobiol.*, 10:321–327, 2000.

[106] Schoch and Eckart D. Gundelfinger. Molecular organization of the presynaptic active zone. *Cell Tissue Res.*, 326:379–391, 2006.

[107] Susanne E. Ahmari, JoAnn Buchanan, and Stephen J. Smith. Assembly of presynaptic active zones from cytoplasmic transport packets. *Nat. Neurosci*, 3:445–451, 2000.

[108] Vardinon Friedman, Tal Bresler, Craig C. Garner, and Noam E. Ziv. Assembly of new individual excitatory synapses: time course and temporal order of synaptic molecule recruitment. *Neuron*, 27:57–69, 2000.

[109] Rong G. Zhai, Hagit Vardinon-Friedman, Claudia Cases-Langhoff, Birgit Becker, Eckart D. Gundelfinger, Noam E. Ziv, and Craig C. Garner. Assembling the presynaptic active zone: A characterization of an active one precursor vesicle. *Neuron*, 29:131–143, 2001.

[110] Mika Shapira, Rong G. Zhai, Thomas Dresbach, Tal Bresler, Viviana I. Torres, Eckart D. Gundelfinger, Noam E. Ziv, and Craig C. Garner. Unitary assembly of presynaptic active zones from piccolo-bassoon transport vesicles. *Neuron*, 38:237–252, 2003.

[111] Peter Sterling and Gary Matthews. Structure and function of ribbon synapses. *Trends Neurosci*, 28:20–29, 2005.

[112] Frank Schmitz, Andreas Königstorfer, and Thomas C. Südhof. Ribeye, a component of synaptic ribbons. *Neuron*, 28:857–872, 2000.

[113] Susanne tom Dieck and Johann H. Brandstätter. Ribbon synapses of the retina. *Cell Tissue Res.*, 326:339–346, 2006.

[114] Janet C. Blanks, Anthony M. Adinolfi, and Richard N. Lolley. Photoreceptor degeneration and synaptogenesis in retinal-degenerative (rd) mice. *J. Comp. Neurol.*, 156:95–106, 1974.

[115] Isabella Spiwoks-Becker, Martin Glas, Irina Lasarzik, and Lutz Vollrath. Mouse photoreceptor synaptic ribbons lose and regain material in response to illumination changes. *Eur. J. Neurosci.*, 19:1559–1571, 2004.

[116] Dominik Wildanger, Eva Rittweger, Lars Kastrup, and Stefan W. Hell. Sted microscopy with a supercontinuum laser source. *Opt. Express*, 16(13):9614–9621, 2008.

[117] Stefan W. Hell, Vladimir Belov, Gyuzel Mitronova, Mariano Bossi, Gael Moneron, Christian Wurm, Stefan Jakobs, Christian Eggeling, Jakob Bierwagen, and Lars Meyer. New fluorinated rhodamines as photostable fluorescent dyes for labelling and imaging techniques. Patent, 2009. PCT/EP2009/004650.

[118] Fritz P. Schäfer, editor. *Topics in applied physics: Dye lasers*, volume 1. Springer-Verlag, 1990.

[119] Vladimir Belov. personal communication.

[120] V. E. Korobov and A. K. Chibisov. Primary processes in the photochemistry of rhodamine dyes. *J. Photochem.*, 9:411–424, 1978.

[121] Stefan W. Hell, Roman Schmidt, and Alexander Egner. Diffraction-unlimited three-dimensional optical nanoscopy with opposing lenses. *Nature Photon.*, 3:381–387, 2009.

[122] Eva Rittweger, Kyu Young Han, Scott E. Irvine, Christian Eggeling, and Stefan W. Hell. Sted microscopy reveals crystal colour centres with nanometric resolution. *Nature Photonics*, 3:144–147, 2009.

[123] Chaitanya K. Ullal, Roman Schmidt, Stefan W. Hell, and Alexander Egner. Block copolymer nanostructures mapped by far-field optics. *Nano Lett.*, 9:2497–2500, 2009.

[124] Byron D. Gates, Qiaobing Xu, J. Christopher Love, Daniel B. Wolfe, and George M. Whitesides. Unconventional nanofabrication. *Annu. Rev. Mater. Res.*, 34:339–372, 2004.

[125] Younan Xia and George M. Whitesides. Soft lithography. *Annu. Rev. Mater. Sci.*, 28:153–184, 1998.

[126] Younan Xia and George M. Whitesides. Soft lithography. *Angew. Chem. Int. Ed. Engl.*, 37:550–575, 1998.

[127] Younan Xia, John A. Rogers, Kateri E. Paul, and George M. Whitesides. Unconventional methods for fabricating and patterning nanostructures. *Chem. Rev.*, 99(7):1823–1848, 1999.

[128] Ralph Nyffenegger and Reg Penner. Nanometer-scale surface modification using the scanning probe microscope: Progress since 1991. *Chem. Rev.*, 97:1195–1230, 1997.

[129] Stephan Krämer, Ryan R. Fuierer, and Christopher B. Gorman. Scanning probe lithography using self-assembled monolayers. *Chem. Rev.*, 103:4367–4418, 2003.

[130] Calvin F. Quate. Scanning probes as a lithography tool for nanostructures. *Surf. Sci.*, 386:259–264, 1997.

[131] David S. Ginger, Hua Zhang, and Chad A. Mirkin. The evolution of dip-pen nanolithography. *Angew. Chem. Int. Ed.*, 43:30–45, 2004.

[132] Harry J. Levinson. *Principles of lithography, 2nd edition*. SPIE - The International Society for Optical Engineering, 2005.

[133] T. Itani, W. Wakamiya, J. Cashmore, and M. Gower. 157-nm lithography with high numerical aperture lens for sub-70 nm node. *Microelectron. Eng.*, 67-68:39–46, 2003.

[134] Sajal Biring, Kun-Tong Tsai, Ujjal Kumar Sur, and Yuh-Lin Wang. High speed fabrication of aluminum nanostructures with 10 nm spatial resolution by electrochemical replication. *Nanotechnology*, 19:355302–355306, 2008.

[135] M. Burkhardt, S. Silverman, Henry I. Smith, D. A. Antoniadis, K. W. Rhee, and M. C. Peckerar. Gap control in the fabrication of quantum-effect devices using x-ray nanolithography. *Microelectron. Eng.*, 27:307–310, 1995.

[136] E. A. Ash and G. Nichols. Super-resolution aperture scanning microscope. *Nature*, 237:510–512, 1972.

[137] E. Betzig, J.K. Trautmann, T.D. Harris, J.S. Weiner, and R.L. Kostelak. Breaking the diffraction barrier: Optical microscopy on a nanometric scale. *Science*, 251:1468–1470, 1991.

[138] C. Eggeling, J. Widengren, R. Rigler, and C. A. M. Seidel. Photobleaching of fluorescent dyes under conditions used for single-molecule detection: Evidence of two-step photolysis. *Anal. Chem.*, 70:2651–2659, 1998.

[139] Roman Schmidt, Christian A. Wurm, Annedore Punge, Alexander Egner, Stefan Jakobs, and Stefan W. Hell. Mitochondrial cristae revealed with focused light. *Nano Lett.*, 9:2508–2510, 2009.

[140] C. Eggeling, J. Widengren, L. Brand, J. Schaffer, S. Felekyan, and C. A. M. Seidel. Analysis of photobleaching in single-molecule multicolor excitation and förster resonance energy transfer measurements. *J. Phys. Chem. A*, 110(9):2979–2995, 2006.

[141] Kirill Kolmakov, Vladimir N. Belov, Jakob Bierwagen, Christian Ringemann, Veronica Müller, Christian Eggeling, and Stefan W. Hell. Novel red-emitting rhodamine dyes for fluorescence microscopy and nanoscopy. *Chem. Eur. J.*, 2009. *accepted*, DOI:10.1002/chem200902309.

[142] Jan Vogelsang, Robert Kasper, Christian Steinhauer, Britta Person, Mike Heilemann, Markus Sauer, and Philip Tinnefeld. A reducing and oxidizing system minimizes photobleaching and blinking of fluorescent dyes. *Angew. Chem. Int. Ed.*, 47:5465–5469, 2008.

[143] Thorben Cordes, Jan Vogelsang, and Philip Tinnefeld. On the mechanism of trolox as antiblinking and antibleaching reagent. *J. Am. Chem. Soc*, 131:5018–5019, 2009.

[144] Christian Eggeling and Christian Ringemann. personal communication, 2009.

[145] Leo Levi. *Applied Optics*. John Wiley And Sons, 1968.

[146] O. G. Peterson, J. P. Webb, W. C. McColgin, and J. H. Eberly. Organic dye laser threshold. *J. Appl. Phys.*, 42(5):1917–1928, 1971.

[147] E. Rittweger, B. R. Rankin, V. Westphal, and S. W. Hell. Fluorescence depletion mechanisms in super-resolving sted microscopy. *Chem. Phys. Lett.*, 442:483 – 487, 2007.

[148] T. A. Klar, E. Engel, and S. W. Hell. Breaking Abbe's diffraction resolution limit in fluorescence microscopy with stimulated emission depletion beams of various shapes. *Phys. Rev. E*, 64:066613, 1–9, 2001.

[149] Rob Zondervan, Florian Kulzer, Sergei B. Orlinskii, and Michel Orrit. Photoblinking of rhodamine 6G in poly(vinyl alcohol): Radical dark state formed through the triplet. *J. Phys. Chem. A*, 107(35):6770–6776, 2003.

[150] Jonas Fölling, Mariano Bossi, Hannes Bock, Rebecca Medda, Christian A. Wurm, Birka Hein, Stefan Jakobs, Christian Eggeling, and Stefan W. Hell. Fluorescence nanoscopy by ground-state depletion and single-molecule return. *Nat. Methods*, 5:943–945, 2008.

[151] M. Bertero and P. Boccacci. *Introduction to inverse problems in imaging*. Institute of Physics Publishing, 1998.

[152] T.J. Holmes and Y.-H. Liu. Richardson-lucy/maximum likelihood image restoration algorithm for fluorescence microscopy: further testing. *Appl. Optics*, 28:4930–4938, 1989.

[153] A.N. Tikhonov and V.Y. Arsenin. *Solutions of Ill-posed problems*. Wiley, New York, 1977.

[154] J. R. Kremer, D. N. Mastronarde, and J. R. McIntosh. Computer visualization of three-dimensional image data using imod. *J. Struct. Biol.*, 116(1):71–76, 1996.

[155] B. Richards and E. Wolf. Electromagnetic diffraction in optical systems ii. structure of the image field in an aplanatic system. *Proc. R. Soc. Lond. A*, 253:358–379, 1959.

[156] Mario Encinas, Montse Iglesias, Yuhui Liu, Hongyin Wang, Ashraf Muhaisen, Valentin Cena, Carme Gallego, and Joan X. Comella. Sequential treatment of sh-sy5y cells with retinoic acid and brain-derived neurotrophic factor gives rise to fully differentiated, neurotrophic factor-dependent, human neuron-like cells. *Journal of Neurochemistry*, 75(3):991–1003, 2000.

[157] C. J. Barnstable, R. Hofstein, and K. Akagawa. A marker of early amacrine cell development in rat retina. *Brain Res.*, 352:286–290, 1985.

[158] R. Jahn, W. Schiebler, C. Ouimet, and P. Greengard. A 38,000-dalton membrane protein (p38) present in synaptic vesicles. *Proc. Natl. Acad. Sci. USA*, 82:4137–4141, 1985.

A Appendix

In the following those relevant experimental details of this thesis are listed that have yet not directly been stated in the text.

A.1 Alignment of dual-color images

For the reasons given in section 2.2 the dual-color STED images have to be taken consecutively with the red channel first followed by the green channel. Possible offsets in the two images are accounted for through addition of double-stained fluorescent beads which serve as landmarks for the overlap. The Overlay is then performed by calculating a translation vector from the difference of the bead centroids in both channels.

The consecutive recording of the dual-color images moreover causes slight sample drift. To quantify the degree of image distortion after overlay - which is equivalent to determining the overlay's accuracy - eight pictures with randomly distributed two-color beads were evaluated yielding an accuracy of approximately 12±9 nm x- and 14±8 nm in the y-direction within a distance of 1 μm from the reference beads.

A.2 Deconvolution

Where indicated, smoothing and contrast enhancement of the image was conducted with an iterative, non-negativity constrained deconvolution procedure, known as the Richardson-Lucy (RL) or Expectation-Maximization algorithm. [151, 152]

In figure 2.17 a single-step linear deconvolution (LD), i. e. a Wiener filter, was carried out. [153]

In both cases the image is deconvolved with an estimated effective PSF FWHM of $\sim$ 30 nm which is justified according to the explanations in section 2.3.1.

Figure	dye(s)	$\mathrm{E_{STED}}$ [nJ]	$\mathrm{t_{dw}}$ [ms]
2.6	yellow-green beads / crimson beads	2.8 / 1.9	6 / 0.5
2.10	Atto 532 / Atto 633	0.6 / 1.2	6 / 0.3
2.11	Chromeo 488 / Atto 633	1.1 / 1.4	6 / 0.5
2.12	Chromeo 488 / Atto 633	1.7 / 1.4	6 / 0.5
2.16	Atto 532 / Atto 633	0.6 / 1.2	6 / 0.3

Table A.1: Table of experimental parameters used in the measurements of chapter 2. The respective first value corresponds to the green channel and the second value to the red channel of the dual-color STED microscope.

A.3 Materials and methods

Dual-color STED: Measurement parameters

Table A.1 provides an overview of the experimental parameters for the dual-color STED measurements discussed in chapter 2. This includes a listing of dyes, pulse energies $\mathrm{E_{STED}}$ and pixel dwell times $\mathrm{t_{dw}}$.

3D reconstruction of dual-color STED images: Image processing

In section 2.3.3 STED images of sectioned samples are shown. For the stereoview image of figure 2.16 several STED images had to be laterally overlapped first as described in section A.1 to give the dual-color representation. Subsequently the dual-color images were stacked vertically. The alignment of consecutive slices was performed by translating and rotating the images until a satisfactory match of the coembedded silica beads was achieved. To build the 3D representations, the manual alignment tool midas was used, which is part of the academic IMOD software suite. [154] Static 3D visualizations of the data stacks were produced with the commercial visualization software package amira (Visage Imaging, Carlsbad, CA). [1]

Calculation of focal peak intensities

Given a certain power of a gaussian shaped beam with wavelength λ, pulse length τ_{pulse} and pulse repetition rate f_{rep} in the back focal plane the focal peak intensity is obtained by first calculating the focal intensity distribution through numerical integration of the Richard-Wolf

---

[1] Image alignment of figure 2.16 was performed by Annedore Punge.

diffraction integral. [155] After yielding the total power by numerical integration in the focal plane the peak power can be pinpointed at the focal point of the PSF.

Cell culture and Immunocytochemistry

Neurofilaments / alpha-Internexin

The SH-SY5Y neuroblastoma cell line was grown as described previously. [156] Cells were seeded on standard glass coverslips to a confluency of about 80%. 10 μM *all-trans*-Retinoic Acid (RA) (EMD Biosciences Inc., San Diego, United States) was added the day after plating. After 5 days in the presence of RA cells were washed three times and incubated with 50 ng/ml human Brain Derived Neurotrophic Factor (hBDNF) (Alomone Laboratories, Jerusalem, Israel) in serum-free medium for up to several weeks.

Immunostaining of neurofilaments as a neuronal marker protein was performed with anti-200 kD Neurofilament heavy subunit phospho mouse IgG (Abcam, Cambridge, UK) and anti-70 kD Neurofilament light subunit rabbit IgG as primary antibodies and with Atto 633 sheep anti-mouse IgG (Atto-Tec, Siegen, Germany) and Chromeo 488 goat anti-rabbit IgG (Active Motif Chromeon GmbH, Tegernheim, Germany) as secondary antibodies, respectively.

Immunostaining of neurofilaments and alpha-internexin was performed with anti-70kD Neurofilament light subunit rabbit IgG (Abcam, Cambridge, UK) and anti-alpha internexin mouse IgG (Acris) as primary antibodies and with Chromeo 488 goat anti-rabbit IgG (Active Motif) and Atto 633 sheep anti-mouse IgG (NHS-dye: Atto-Tec, Siegen, Germany and unconjugated antibody: Dianova) as secondary antibodies, respectively. The cells were mounted in Mowiol containing Dabco.

Syntaxin 1 / Synaptophysin / SNAP-25 and Sample Sectioning

Primary cultures of neonatal rat hippocamal neurons were prepared as described [102] and were used between 15 and 25 days in vitro. For labeling, the neurons were fixed with 4% paraformaldehyde (ice-cold), quenched with 50 mM ammonium chloride, permeabilized by use of 0.1% Triton X-100 and immunostained as described [102] using antibodies against syntaxin 1 (HPC-1 mouse monoclonal), synaptophysin (G96 rabbit polyclonal) and SNAP-25 (71.1, Synaptic Systems, Göttingen, Germany). [68, 157, 158] Secondary antibodies (Dianova GmbH, Hamburg, Germany) were conjugated with the fluorescent dyes Atto 532 and Atto 633, respectively (Atto-Tec). The preparations were then post-fixed with paraformaldehyde and embedded in Nanoplast resin (Polysciences, Inc., Warrington, PA, USA) as described elsewhere. [68] The polymerised blocks were detached from the coverslips by dipping them into liquid nitrogen and cut with an ultramicrotome (EM UC6, Leica Microsystems GmbH, Wetzlar, Germany) using an ultrasonic diamond knife (Diatome AG, Biel, Switzerland). The slices were afterwards transferred onto glass coverslips.

Bassoon

Samples used for the measurements described in section 2.3.4 were prepared from vertical cryostat sections of P2 mouse retina stained with a polyclonal rabbit anti-Bassoon antiserum, followed by the incubation with an antirabbit secondary antibody labeled with the organic fluorophore Atto 633. The Bassoon-stained transport units were imaged in confocal and STED modes (see Figure 2.17). [67]

Sample preparation of Nanobeads

Gold Beads

For the preparation of gold beads (used for probing the microscope's PSF) $\sim$ 4.5 g PVA were dissolved in 30 mL water. Stirring and heating to $\sim$ 50 °C speeded up dissolution significantly. The gold colloid (80 nm, British Biocell) was sonicated for 10 minutes. 20 μL of the gold colloid were pipetted into an Eppendorf cut and diluted with 200 μL of the PVA solution. Then 100 μL of the dispersion were transferred to a coverslip and spincoated at 4000 rpm for 30 seconds to yield a uniform polymer film. The sample was dried overnight in a dessicator. Finally, the coverslip was mounted onto a microscope slide with immersion oil and glued with nail polish.

Fluorescent Beads

Samples of fluorescent nanobeads were prepared as follows: First, the stock solution of the beads was diluted according to the desired final bead density ($\sim$ 1:1000 - 1:10000). The resulting dispersion was sonicated for $\sim$ 30 minutes. Meanwhile, 100 μL of Poly-L-Lysine (0.1% w/v in water, Sigma-Aldrich, Germany) were poured on a clean coverslip. After 10 minutes the solution was sucked off using a vacuum pump. Then $\sim$ 50 μL of the bead dispersion were pipetted on the coverslip. 10-15 minutes later the dispersion was sucked off and the cover slip was rinsed carefully with small amounts of distilled water. Drying of the coverslip was followed by mounting the the coverslip onto a microscope slide using Mowiol.

Acknowledgements

For giving me the unique opportunity to scientifically contribute to the exciting field of STED nanoscopy I would first of all like to thank Prof. Dr. Stefan W. Hell. Besides providing a dynamic and stimulating working atmosphere at the Max Planck Institute for Biophysical Chemistry in Göttingen he never hesitated to share his expertise in fruitful discussions.

Prof. Dr. Joachim Spatz is gratefully acknowledged for serving as the first referee of my thesis and for warranting an efficient and uncomplicated accomplishment of an external dissertation.

The challenging task of researching in a truly interdisciplinary field affords the opportunity to work closely with people of various scientific backgrounds. In the first instance I would therefore like to thank Dr. Jan Keller who never got tired of teaching me the secrets of scientific programming, Dr. Christian Eggeling who often came up with good advice, Dominik Wildanger who collaborated in the dual-color STED project as a Diploma student and Dr. Vladimir Belov and his synthetic chemistry group who provided novel and improved fluorescent dyes.

Further collaborators (in alphabetic order) include Dr. Gerald Donnert (dual-color STED project), Jaydev Jethwa (laser alignment), Rebecca Medda (preparation of biological samples), Dr. Gael Moneron (laser alignment), Annedore Punge (preparation of sectioned samples for 3D reconstruction of dual-color STED images), Dr. Hanna Regus-Leidig (biologist investigating mouse retina photoreceptor ribbon synapses), Dr. Silvio O. Rizzoli (preparation of biological samples for the dual-color STED project) and Dr. Andreas Schönle (development of the measurement software 'Imspector').

The nature of research in optical science requires the management of manifold technical questions. The staff of the mechanical workshop at the MPI for Biophysical Chemistry has always been eager to find prompt solutions to optomechanical issues. Likewise, the optics and electronics workshops have contributed to the successful accomplishment of this work by providing adequate devices.

For critically reading the manuscript of this thesis (or parts thereof) I would furthermore like

to thank Dr. Christian Eggeling, Dr. Lars Kastrup, Dr. Jan Keller, Rebecca Medda, Dr. Claas von Middendorff and Dr. Hanna Regus-Leidig.
At all stages not only of this thesis but of my whole life I have experienced invaluable support by my family, i. e., my parents and my two brothers. Together with my long-term partner Katharina they remind me of the truly important things in life.
Last but certainly not least I would like to acknowledge the swimming team of the University of Göttingen for keeping me in shape physically. Training sessions were both demanding and diverting while simultaneously social aspects were rarely neglected.

Göttingen, October 2009

Erklärung gemäß § 8(3) b) und c) der Promotionsordnung:

a) Ich erkläre hiermit, dass ich die vorgelegte Dissertation selbst verfasst und mich keiner anderen als der von mir ausdrücklich bezeichneten Quellen und Hilfen bedient habe.

b) Ich erkläre hiermit, dass ich an keiner anderen Stelle ein Prüfungsverfahren beantragt bzw. die Dissertation in dieser oder anderer Form bereits anderweitig als Prüfungsarbeit verwendet oder einer anderen Fakultät als Dissertation vorgelegt habe.

____

(Lars Meyer)